Strong Suppression of Υ Excited States in Pb+Pb Collisions at $\sqrt{s_{\mathrm{NN}}} = 5.02$ TeV with the CMS Detector

By

Chad Steven Flores
B.S. (University of California, Davis) 2011
M.S. (University of California, Davis) 2012

Dissertation

Submitted in partial satisfaction of the requirements for the degree of

Doctor of Philosophy

in

Physics

in the

Office of Graduate Studies

of the

University of California

Davis

Approved:

Manuel Calderón de la Barca Sánchez, Chair

Daniel Cebra

Ramona Vogt

Committee in Charge

2017

To my late grandfather, Eulalio "Papa" Flores,
who taught me to work hard and be proud of who I am.
I "gave them hell" and they gave me a Ph.D.

Contents

List of Figures

List of Tables

Abstract

Strong Suppression of Υ Excited States in Pb+Pb Collisions at $\sqrt{s_{\mathrm{NN}}} = 5.02$ TeV with the CMS Detector

The relative yields of Υ mesons produced in $p+p$ and Pb+Pb collisions at $\sqrt{s_{\mathrm{NN}}} = 5.02\,\mathrm{TeV}$ and reconstructed via the dimuon decay channel are measured using data collected by the CMS experiment. Double ratios are formed by comparing the yields of the excited states, Υ(2S) and Υ(3S), to the ground state, Υ(1S), in both Pb+Pb and $p+p$ collisions at the same energy. The double ratios, $[\Upsilon(n\mathrm{S})/\Upsilon(1\mathrm{S})]_{\mathrm{PbPb}}/[\Upsilon(n\mathrm{S})/\Upsilon(1\mathrm{S})]_{pp}$, are measured to be 0.308 ± 0.055 (stat) $\pm\, 0.019$ (syst) for the Υ(2S) and less than 0.26 at 95% confidence level for the Υ(3S). The double ratios are studied as a function of collision centrality, as well as dimuon transverse momentum, and rapidity. As a function of collision centrality the Υ(2S) double ratio is consistent with unity in the most peripheral (70–100%) bin and is consistent with zero in the most central (0–5%) bin. The Υ(2S) double ratio is consistent with a constant dependence on the kinematic variables, with a large suppression seen throughout the studied kinematic range. No significant Υ(3S) signal is found in the Pb+Pb data. The Υ(3S) double ratio is consistently below unity for all bins, including the most peripheral (50–100%) bin, indicating a strong suppression of the Υ(3S) relative to the Υ(1S).

Acknowledgments

My academic journey would not have been possible without the encouragement and support from my wife, family, friends, mentors, and peers. I will not be able to thank everyone for making this work possible but I would like to take a moment to acknowledge a select few. To those that I failed to mention, thank you for all you have done for me.

To my adviser, Manuel: thank you for being a great teacher, mentor, and friend. From my first years at UC Davis, as an undergraduate, you were always willing to listen to my personal and academic obstacles. You always provided me with well balanced advice and encouragement to keep pushing forward for the best life and for the best possible physics. I will miss all the times I was able to learn from you and the fun we had working side-by-side at CERN.

To Daniel, thank you for always pushing me to think critically and to be a better example for the younger generation of researchers in the group. I will miss our many softball discussions as well as having you as a teammate.

To Rylan and Michael, thank you for helping me learn to become an efficient researcher on CMS. Rylan, thank you for listening to my research woes even after you left the Davis group. Chris, thank you for always taking the time to discuss interesting problems in the office. I thank the three of you for being some of the best senior graduate students I could have looked up to and call my friends.

To my younger CMS counterparts: Ota and Santona, thank you for making it seem like I knew what I was doing and for pushing me to explain everything better.

To my CMS heavy-ion crew: this thesis would not be possible without the help and support from Camelia, Nicolas, Émilien, Raphaël, Jason, Yongsun, Songkyo, Dongho, Jaebeom, Geonhee, Mihee, and André. I can not thank you all enough for all that you have taught me and for being great friends.

To Kai Liu, thank you for inviting me to join your lab as an undergrad at Davis. The time I spent in the lab was priceless. Thank you for encouraging me to go to graduate school.

To Dave, Rachael, Greg, Will, and Fred: thank you for making undergrad amazing. I could not have asked for a better group of study partners and friends. To Dusty, James and Dustin: we are doctors now. Graduate school at Davis would not have been the same without you guys there to cheer me on and listen to me vent. Cheers to more fun and adventures.

To my family: Dad, thank you for always believing in me and pushing me to be the best version of me. You always taught me to ask questions about life and nature and that is what motivated my desire to study physics. Mom, thank you for always encouraging me to do science and to pursue anything I wanted. I am thankful for your love and support all through my life. Shannon, Andrea, and Anthony: thank you for my role models and for always being there to support me as your little brother through food, money, time, and conversations. To all my family, I love you and am thankful for all you have done for me. To the younger generations and to the future generations to come, I hope my work inspires you to pursue whatever it is you want.

Last but certainly not least, to my wife: Dora, you have always been there for me from the beginning of my academic journey. I would not be here if you had not convinced me to go to community college. I love you and am thankful for all your support and sacrifice during my many years in college. Our future is bright and I look forward to spending it with you.

Chapter 1

Introduction

1.1 Standard Model

This chapter presents a very brief introduction to the some of the properties of the fundamental particles and their interactions to give some context to the topic of this thesis, which will focus on the strong interaction. The standard model of particle physics describes the collection of fundamental particles as well as the strong, electromagnetic, and weak interactions. It does not provide a description of gravity and how it connects to the other fundamental forces. The electromagnetic interaction describes the interaction between electrically-charged particles and is described by the theory known as quantum electrodynamics (QED). The propagator or mediator of the electromagnetic force is the photon. The photon is a massless, electrically neutral object. The weak interaction describes interactions of fundamental particles via the propagators, Z and W particles. In a basic sense, the weak interaction can explain and is responsible for radioactive decay. The strong interaction can describe the interactions of the nucleons within the nucleus (residual strong force) and also the interactions of the partons (quarks and gluons) inside of the nucleons. The focus of the research in this thesis is the strong interaction between partons, described by a theory known as Quantum Chromodynamics (QCD). Figure 1.1 shows the standard model particles. They are broken down into bosons, which are integer spin particles, and fermions, half-integer spin particles. Fermions make up the things around us and can be constituents of other particles. The quarks are the fundamental

fermions that interact via the strong interaction. They are also the building blocks of the nucleons, i.e. protons and neutrons, which in turn are the building blocks of nuclei. Quarks exist in 6 fundamental types, which we call 'flavors': up (u), down (d), charm (c), strange (s), top (t), and bottom/beauty (b) as well as their respective anti-particles. The leptons are fundamental fermions that do not interact via the strong interaction and consist of a set of massive charged particles and their respective massless (or very low mass) electrically neutral neutrino. They also include a respective anti-particle. These consist of the electron (e) and the electron neutrino (ν_e), the muon (μ) and muon neutrino (ν_μ), the tau (τ) and the tau neutrino (ν_τ). All of the fundamental fermions also interact via the weak and the electromagnetic interaction, except for neutrinos, which only interact via the weak interaction. The bosons are the force carriers as described earlier: the photon γ, the W, the Z, the gluon (g), and the Higgs (H). The H is the carrier of the Higgs force that is responsible for how the fundamental particles obtain their masses. The g is the force propogator of the strong force and is of great importance in this thesis. The following sections will go on to describe the importance that the strong force, quarks, and gluons they have in the field of heavy-ions. It will then lead to how the μ plays a role in measuring the Υ, a bound state of b and $\bar{b}$ quarks.

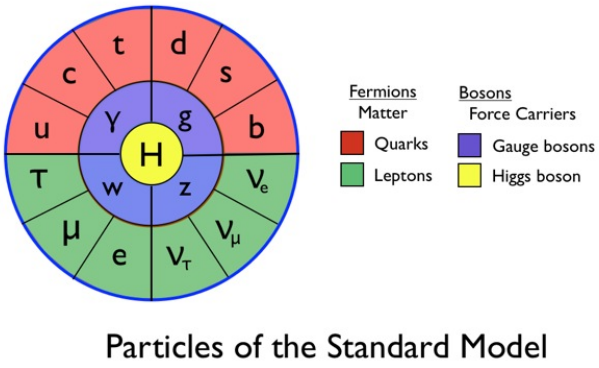

Figure 1.1: Particles of the Standard Model [1].

1.2 Heavy Ion Collisions

The field of heavy ion physics is concerned with understanding the interactions of QCD in a deconfined state. This deconfined state of quarks and gluons is known as the Quark Gluon Plasma (QGP), and is formed in the high-energy collisions that occur between heavy nuclei such as gold (Au) and lead (Pb). Once a collision occurs, a densely packed system of nucleons is created in which the quarks and gluons become quasi-free due to sufficient high energy density and overlap and are expected to cross over to a deconfined phase of nuclear matter. In this subsection I will briefly describe some basic aspects of QCD and its relation to the QGP, as well review some experimental observables of the QGP, including the one specific to the work in this document.

1.2.1 QCD

QCD is a non-Abelian gauge theory, which describes the interactions of partons that are the building blocks of hadrons such as the proton. These partons are a collective group of particles known as quarks and gluons, as described earlier. Quarks and gluons contain a specific charge referred to as the color charge analogously to the electric charge from QED. The charge portion of QCD can be described by the SU(3) symmetry or rather the special group of 3×3 unitary matrices. The color charges in QCD contain three distinct types and their respective anti-charge. The force carrier in QCD is the gluon, which itself can carry color and therefore interact with other gluons (in other words, gluons couple to each other). This behavior is in sharp contrast to that of the QED force carrier, the photon, which is electrically neutral [2, 3].

The Lagrangian density of QCD is given by [2]:

$$\mathcal{L} = \sum_q \bar{\psi}_{q,a}(i\gamma^\mu \partial_\mu \delta_{ab} - g_s \gamma^\mu t^C_{ab} \mathcal{A}^C_\mu - m_q \delta_{ab})\psi_{q,b} - \frac{1}{4} F^A_{\mu\nu} F^{A\mu\nu}, \tag{1.1}$$

where the repeated indices are summed and:

- γ^μ refers to the Dirac γ matrices.
- $\psi_{q,a}$ refers to the quark-field spinors with flavor q and a as a color index ($1 \leq a \leq N_c$) where N_c is the number of colors; $N_c = 3$.

- m_q refers to the mass of a quark with flavor q.
- $\mathcal{A}_\mu^C$ refers to the gluon fields where $(1 \leq C \leq 8)$ In other words, there are eight types of gluons.
- t_{ab}^C refers to the eight 3×3 matrices of SU(3) which are the generators of the group and contain the information that when a gluon interacts with a quark, the quark's color rotate in the SU(3) space.

and

$$F_{\mu\nu}^A = \partial_\mu \mathcal{A}_\nu^A - \partial_\nu \mathcal{A}_\mu^A - g_s f_{ABC} \mathcal{A}_\mu^B \mathcal{A}_\mu^C \tag{1.2}$$

where f_{ABC} are structure constants of SU(3) generators that follow this commutation relation:

$$\left[t^A, t^B\right] = i f_{ABC} t^C. \tag{1.3}$$

An interesting aspect of QCD is that there is no evidence for freely moving quarks and gluons in our everyday life, in contrast to the case of QED, where electrons and photons are a large part of our everyday experience with nature. When two electrically charged particles are pulled away from each other, the force between them decreases with increasing distance. With QCD, when two color charges are pulled apart, the force increases with increasing distance, thus confining the quarks and gluons inside of a hadron. When the distance between two quarks becomes increasingly larger the potential energy contained in the field can then be transformed into masses of new quarks. However, at short distances inside the hadron the partons can be thought of as free particles with small interaction coupling. The quarks can also behave freely at asymptotically large momenta when interacting with another high-momentum projectile. This is collectively known as asymptotic freedom [2, 3]. Since QCD confines quarks to hadrons I will introduce various types of hadrons. **Hadrons** are composite particles made up of quarks and gluons. There are 2 basic combinations that are found in nature: **baryons**, a composition of 3 quarks,

such as a proton or neutron and **mesons**, a quark anti-quark pair, such as a pion (π) or an Upsilon (Υ).

1.2.2 QGP

The QGP, as described previously, is a deconfined state of quarks and gluons at large energies and short distances. To understand the properties of the QGP, a mathematical formulation is needed for this strongly interacting matter. QCD is of course the mathematical theory of the strong interaction, but a key question is: How can properties and quantities related to the QGP be calculated. As described, QCD is asymptotically free at short length scales: smaller than the size of a hadron. In such cases, we could use perturbation theory to understand the interaction. However, at very high energy or momentum, perturbation theory requires some re-configuring using re-normalization. It is however possible to use a non-perturbation approach in which the QCD fields are discretized on a lattice, an approach known as lattice QCD. The purpose of lattice QCD is to map out space-time points with a finite spacing on a discrete lattice. This finite discretization regularizes the theory and thus removes the need for re-normalization in the perturbative approach [2, 3]. In a finite lattice, regular QCD is restored when the lattice spacing goes to zero.

A large portion of heavy-ion physics is devoted to understanding the Equation of State (EoS) of the QGP built on the basis of QCD. Thermodynamic quantities of the EoS such as pressure, energy, and entropy studies as a function of temperature can help provide evidence for the transition to a deconfined, state strongly-interacting state of matter known as the Quark Gluon Plasma. Figure 1.2 shows the energy density and the pressure for three different lattice scenarios for the temporal extent [4]. The overall behavior of both the energy density (symbols) and the pressure (lines) shows a quick rise around 185 MeV $< T <$ 195 MeV. This inflection when going from low to high temperature implies a rapid increase in the number of degrees of freedom of the system, i.e. a new phase. The lack of discontinuities signifies that it not a phase transition, but rather a rapid cross-over. In this new phase of matter, the color fields that were interacting on a scale smaller than a hadron can now interact over larger ranges, thus exhibiting deconfiment on a larger

scale. This feature is the key aspect to the existence of the QGP and the experimental goal of this field is to probe matter to reveal its thermodynamic properties, such as the temperature that this transition occurs. In this thesis the key observable can help probe the initial temperature of the system, which in some cases can be predicted to be about three times larger that the cross-over temperature [5].

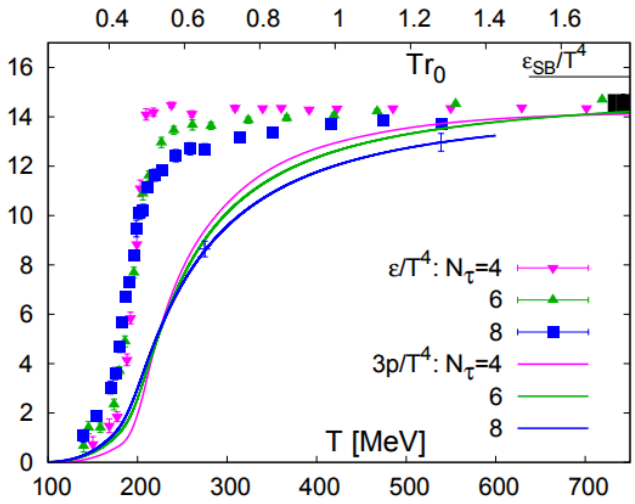

Figure 1.2: Energy density (symbols) and three times the pressure (lines) for various lattices with temporal extent, N_τ, of 4 (magenta), 6 (green), and 8 (blue) [4].

1.2.3 Experimental Observables

Once a QGP has formed in a high energy heavy-ion collision, it is now the purpose of the experimental field to find ways to understand this strongly-interacting matter through final-state measurements and (in the particular case for this thesis) using a particle collider.

When the QGP forms, particles created can undergo energy loss. In the most basic formation we have a QGP as described as a sea of partons that are freely moving. As other partons, created by the initial collision of nuclei, begin their propagation through this matter, they can interact via the strong force. This interaction is described as loss in energy as the colored objects surrounding this parton as it is traveling can either cause it to scatter or induce radiation and thus decrease the initial energy [3, 6]. Figure 1.3 shows the charged hadron two-particle azimuthal angle distribution. In the bottom panel (b) the

$p+p$ (black line) and Au+Au (blue stars) angular correlations are overlaid. At $\Delta\phi = 0$ the peaks match while at $\Delta\phi = \pi$ there is a large reduction in the Au+Au events. This modification at large $\Delta\phi = \pi$ is due to parton energy loss in the QGP medium. These events at $\Delta\phi = \pi$ are back-to-back jets (collection of partons). The idea of modification is an integral one in the field of heavy-ions and (as introduced here) there is always a baseline of $p+p$ events that are needed to compare to a heavy-ion collision event.

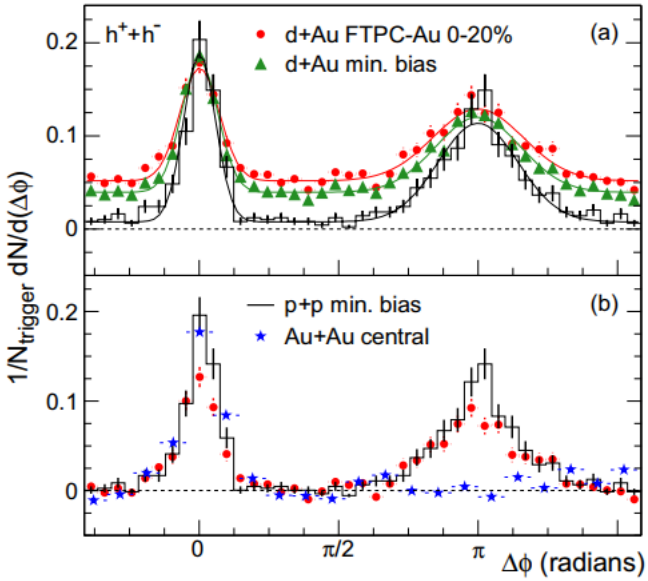

Figure 1.3: Two-particle azimuthal angular distrubtion of charged hadrons in d+Au central and minimum bias events (a) and (b) a comparison of $p+p$ (black) and Au+Au (blue stars) with d+Au event overlaid from (a). [6].

The modification we saw previously in the charged hadron distribution was seen by comparing events in $p+p$ and Pb+Pb. Analogously, we look at another way to observe modification in a heavy-ion collision known as R_{AA}. This nuclear modification is defined as the number of events producing a particular particle, as a function of p_T or y, in heavy-ion collisions divided by the number of events producing that particle in $p+p$ collisions scaled by the number of binary nucleon-nucleon collisions in the heavy-ion collisions. The reason that $p+p$ events are used is because there is not a high enough temperature and density in a single $p+p$ event to form a QGP. Although, one should be careful, there are some arguments for having QGP-like behavior in small systems, once you have very

high multiplicity events. Therefore $p+p$ collision events at the same energy as heavy-ion collision events are known as the reference or baseline. The nuclear modification, $R_{\rm AA}$, is given by

$$R_{\rm AA}(p_T, y) = \frac{d^2N^{\rm AA}/dp_T dy}{T_{\rm AA} d^2\sigma^{pp}/dp_T dy} \tag{1.4}$$

, where $d^2N^{\rm AA}/dp_T dy$ is the differential yield of a given quantity of interest in a heavy-ion collision, $d^2\sigma^{pp}/dp_T dy$ is determined from the differential cross-section of that type of quantity in a $p+p$ event, and $T_{\rm AA}$ is the geometrical overlap region of the colliding nuclei that describes the region of activity during the heavy-ion collision. If the measured $R_{\rm AA}$ value is larger than unity, the modification is an enhancement since we see more than would be expected by a simple superposition of nucleon-nucleon collisions. If the measured $R_{\rm AA}$ is less than unity it is known as suppression, which implies that there are physics effects that suppress the yield compared to what would be expected from a superposition of nucleon-nucleon collisions. Finally, if the measured $R_{\rm AA} = 1$ then there is no modification and the scaling with binary collisions holds.

Figure 1.4 shows results of $R_{\rm AA}$ from CMS at a center-of-mass energy per nucleon pair, $\sqrt{s_{\rm NN}} = 2.76$ TeV. Measurements of the Z (black triangle with red box), W (black square pink box), and high p_T direct photons (black downward triangle yellow box) have a nuclear modification value of one within their errors. This indicates that the Z, W, and isolated photons are not affected by the QGP medium. It is expected that these particles are unaffected because they do not have color charge, so they do not interact via the strong interaction, and therefore will not be affected as they pass through this strongly interacting QCD matter. All the other quantities in the figure are hadronic in origin, and therefore their suppression is indicative of energy-loss of their parent partons in the QCD medium.

The research topic of this thesis is that of the modification of Υ mesons in heavy-ion collisions. The measurement of all three Υ states in heavy-ion collisions was first measured at the Compact Muon Solenoid (CMS) experiment with data from 2011 at $\sqrt{s_{\rm NN}} = 2.76$ TeV. It was confirmed that the modification, in this particular case suppression, of the

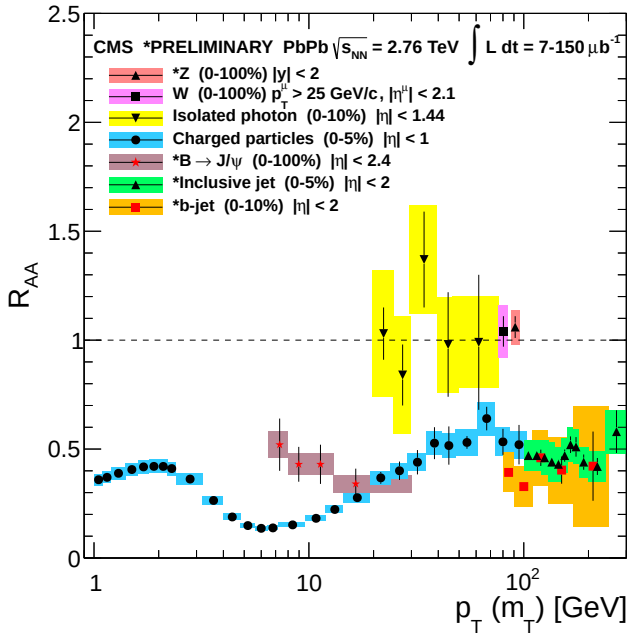

Figure 1.4: R_{AA} as a function of transverse momentum or transverse mass for various signals in Pb+Pb collisions at 2.76 TeV [7]

three states were modified sequentially. This meant that the Υ(1S)(ground state) had the smallest suppression, then the Υ(2S), and finally the Υ(3S) had the largest suppression. Figure 1.5 shows the R_{AA} as a function of N_{part} for the Υ(1S) and Υ(2S). The value of N_{part} number of participating nucleons, is a measure of the activity of the event in a heavy-ion collision. This value will be discussed further in Chapter 4. There is a clear suppression of the Υ(2S) (green) over all N_{part} values, indicating a difference in the Υ(1S) and Υ(2S)modification at lowest N_{part}.For the Υ(1S) (red) the only value not exhibiting suppression is the lowest N_{part} value where it is predicted that there will be no modification because the amount of activity and system size in that low N_{part} region is more like a $p+p$ event. However, since the Υ(2S) is suppressed at low N_{part}this would indicate a smaller temperature of the system, one that would not be large enough to modify the Υ(1S). The next section will cover an observable relate to the R_{AA} of the Υ meson.

1.2.3.1 Double Ratio

The work presented in this document consists of the measurement of the Υ double ratios from Pb+Pb collisions at $\sqrt{s_{\mathrm{NN}}}$=5.02 TeV with the CMS detector. The Pb+Pb and the

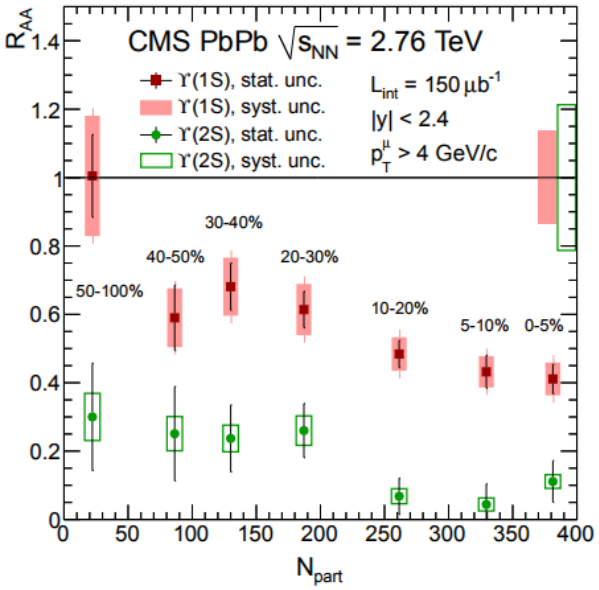

Figure 1.5: R_{AA} of the Υ(1S) (red) and Υ(2S) (green) as a function of N_{part} in Pb+Pb collisions at 2.76TeV [8]

$p+p$ collision data were obtained at the same center-of-mass energy during the heavy-ion running period of November-December 2015. Υ mesons are reconstructed via the dimuon (two muon vertex) decay channel. The double ratio is a measurement of the ratio of the excited to ground state yields in Pb+Pb collisions divided by the corresponding ratio measured in $p+p$ collisions.

The double ratios of the Υ(2S) and Υ(3S) mesons, $\mathcal{DR}_{21}$ and $\mathcal{DR}_{31}$ are defined respectively as:

$$\mathcal{DR}_{21} \equiv \frac{(\Upsilon(2\mathrm{S})/\Upsilon(1\mathrm{S}))_{\mathrm{PbPb}}}{(\Upsilon(2\mathrm{S})/\Upsilon(1\mathrm{S}))_{\mathrm{pp}}}, \mathcal{DR}_{31} \equiv \frac{(\Upsilon(3\mathrm{S})/\Upsilon(1\mathrm{S}))_{\mathrm{PbPb}}}{(\Upsilon(3\mathrm{S})/\Upsilon(1\mathrm{S}))_{\mathrm{pp}}} \tag{1.5}$$

where

- Υ(1S), Υ(2S), and Υ(3S) correspond to the extracted yields of the corresponding Υ states;
- The single ratios, $\mathcal{R}_{21} = \Upsilon(2\mathrm{S})/\Upsilon(1\mathrm{S})$ and $\mathcal{R}_{31} = \Upsilon(3\mathrm{S})/\Upsilon(1\mathrm{S})$ in the numerator of the double ratio are measured in Pb+Pb collisions while the same single ratios are made in the denominator of the double ratio for $p+p$ collisions.

The double-ratio measurements are equivalent to a ratio of nuclear modification factors of the relevant states, for example, in the case of the $\Upsilon(2S)$ we have:

$$\mathcal{DR}_{21} = \frac{R_{AA}(\Upsilon(2S))}{R_{AA}(\Upsilon(1S))}. \tag{1.6}$$

A double ratio of unity implies that the excited states are modified by the same factor as the ground state, and values less than unity signify that the excited states suffer additional suppression relative to the ground state. The advantage of double-ratio measurements is that experimental corrections, in particular those to account for efficiency and acceptance, cancel in the double ratio.

The goal of the research encompassed in this thesis was to extend our previous observations of the relative suppression of the Υ mesons to a higher energy than the previous measurement, shown in Fig. 1.6. This previous measurement [8] was of the $\mathcal{DR}_{21}$ as a function of N_{part}. The measurement showed a large relative suppression for all values of N_{part} at $\sqrt{s_{\text{NN}}} = 2.76$ TeV. We wanted to extend this measurement to data collection in Pb+Pb collisions at 5.02 TeV with much better statistical precision. With the increase in the amount of data at 5.02 TeV, we can analyze the relative suppression in narrower centrality bins, and explore $\mathcal{DR}_{21}$ as a function of dimuon p_T and y. In addition, we wanted to make a first measurement of $\mathcal{DR}_{31}$ as a function of N_{part} to provide a more complete story of the relative suppression. In particular, the $\Upsilon(3S)$ is the most loosely bound quarkonia state and begins to be modified first and at lower temperatures.

The structure of this document will start with some introduction to the theoretical models related to the observation of the double ratio in Chapter 2, it will then lead to a discussion on the CMS detector used to reconstruct the Υ decays in Chapter 3, then proceed to discuss some of the data selection criteria in Chapter 4. Chapter 5 is the most extensive of this thesis, and contains the main analysis portion. It starts with the method for fitting the dimuon invariant mass spectrum to extract the Υ yields and ratios. It then continues to discuss the efficiencies and acceptance to study their cancellation, and the size of any possible non-cancellation. Chapter 5 finishes with a discussion about the systematics that arise from the various fitting methods and the assumption that the efficiency fully cancels. Chapter 6 lays out the full results for the double ratio including

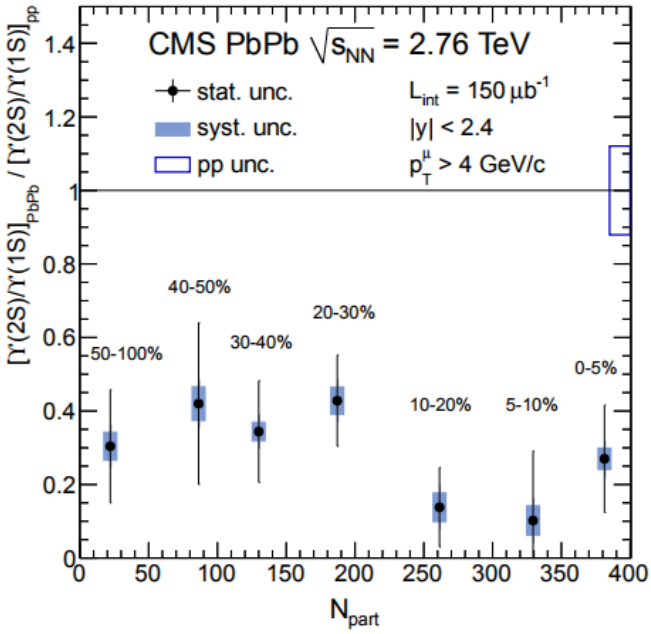

Figure 1.6: $\mathcal{DR}_{21}$ as a function of N_{part} in Pb+Pb collisions at 2.76TeV [8]

the Υ(2S) and Υ(3S) results, as well as comparisons with theory from Chapter 2 and a comparison to a previous experimental measurement [8] at a lower collision energy in Fig. 1.6. Chapter 7 concludes this work.

Chapter 2

Quarkonia in Medium

The term Quarkonia refers to the families of bound state flavorless heavy-quark charmed ($c\bar{c}$) and bottom ($b\bar{b}$) particles. Particularly interesting particles of this family are the J/ψ, a $c\bar{c}$ bound state of mass 3.096 GeV/c^2, and the Υ, a $b\bar{b}$ bound state of mass 9.460 GeV/c^2. These two meson states have dilepton decay channels, making them easily detectable in an experiment, particularly one with excellent muon-detection capabilities. Specifically they can decay to two oppositely charge electrons or muons. This family of particles is of particular interest due to original work dating to 1986 by Matsui and Satz on J/ψ suppression due to color Debye screening in a QGP [9]. The model they proposed describes the bound charm state in a quark gluon plasma with freely moving colored objects. If and when a charmed quark and anti-charmed quark pair is formed they can interact with the medium and become "screened" from each other. In other words the J/ψ bound state will not form at a given temperature due to the plasma being created, because the interaction between the charm quarks will be screened by the presence of other strongly-interacting colored partons in the plasma, preventing the charm and anti-charm quarks from binding. In the years since this idea was first proposed, many more models have helped refine our understanding of the mechanisms that lead to screening or melting of these heavy-quark bound states. It should be noted that although the original work from Matsui and Satz discussed the J/ψ, their model can be extended to treat the screening of the Υ meson.

Figure 2.1 shows the bottomonium family (which includes the Υ mesons) and their

respective quantum numbers. The Υ family contains the ground state Υ(1S), and excited states Υ(2S) and Υ(3S). The Υ(4S) is not studied as it resides above the $B\bar{B}$ threshold, therefore the Υ(4S) will decay strongly to a pair of B mesons. The less massive Υ states are energetically forbidden from such a decay. As seen in the figure, the Υ family is a complicated one as there are many feed-down decays from other particles, so understanding an inclusive measurement can become complicated. For that reason most measurements are inclusive and many theoretical predictions do take into account both direct production and feed-down contributions, as well as the suppression pattern for each state depending on its binding energy and spectral properties.

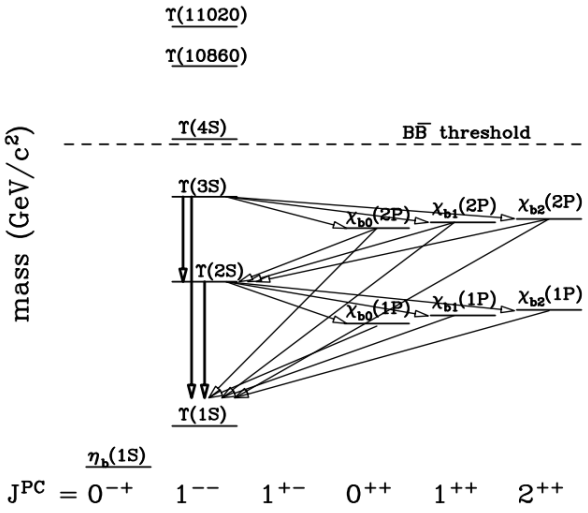

Figure 2.1: Bottomonium family with quantum numbers [3].

Since the mass ordering goes as the $m(\Upsilon(3S)) > m(\Upsilon(2S)) > m(\Upsilon(1S))$ it follows that the average radius of the Υ states, as calculated from its radial wave function, also follows the same ordering. Figure 2.2 shows the radial wave functions for the Υ family at a temperature $T = 0$ (no plasma formation) and $T = 200$ MeV (with a plasma). The figure shows that with increased temperature the radial wavefunction, and hence the average radius, of the Υ(1S) is mostly unaffected, indicating that at 200 MeV the screening effects for the Υ(1S) are very modest. The excited states, Υ(2S) and Υ(3S), clearly exhibit a broadening of the radius and thus are readily affected by the QGP medium even at the modest QGP temperature of 200 MeV. This model shown in Fig. 2.2 comes from a

description of a potential containing a string and Coulomb part and is referred to as the Cornell potential, given as

$$V_{Q\bar{Q}} = \sigma r - \alpha_{\text{eff}}/r, \tag{2.1}$$

where σ is the string tension and α_{eff} refers to the Coulomb-like coupling accounting for short range gluon exchange [10]. The $Q\bar{Q}$ is in reference to the heavy $Q\bar{Q}$ system where $Q = c$ or b. As temperature is increased, the heavy quark bound state can be screened, as described. The screened potential is given as

$$V(r,t) = \sigma r_D \left[1 - e^{-r/r_D}\right] - \left[\frac{\alpha_{\text{eff}}}{r_D} + \frac{\alpha_{\text{eff}}}{r} e^{-r/r_D}\right] \tag{2.2}$$

where r_D is the Debye radius. This is the radius which is dependent on the temperature of the medium. At a given critical deconfining temperature the heavy quark state will not survive. As in electromagnetic plasmas, if the Debye radius is sufficiently smaller than the binding radius r then the heavy quark state will be screened. If the radius is larger than the binding radius the state is allowed to form and stays bound.

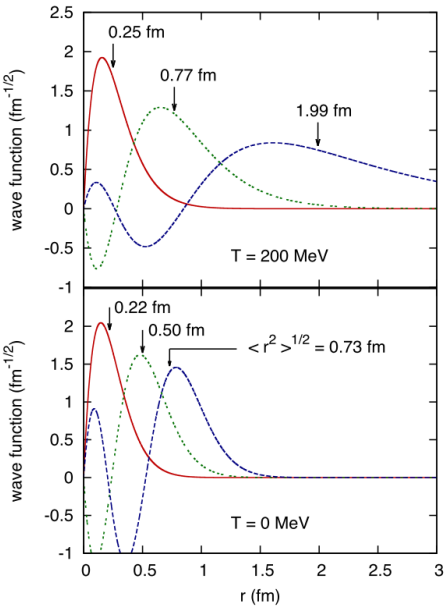

Figure 2.2: Radial wave functions for the Υ(1S) (solid red) Υ(2S) (dotted green) and Υ(3S) (dashed blue) at $T = 0$ (bottom panel) and $T = 200$ MeV (top panel) [10].

In recent studies, the calculations not only consider the screening from the real part of the potential but include an imaginary part of the potential. This imaginary part contains effects that contribute to the broadening of the width of the state and also contribute to the suppression of the yields [11, 12, 13]. Figure 2.3 shows the real part of the heavy quark potential (left) and the imaginary part of the potential (right). The figure contains calculations from lattice QCD with varying temperatures as a function of T with largest temperature ($T = 1.66T_c$ with $T_c = 172.5$ MeV) colored red and the lowest temperature as purple. As the temperature increases it is clear from the real part of the potential that the potential begins to flatten out and screening starts to occur and the heavy quark state is no longer bound.

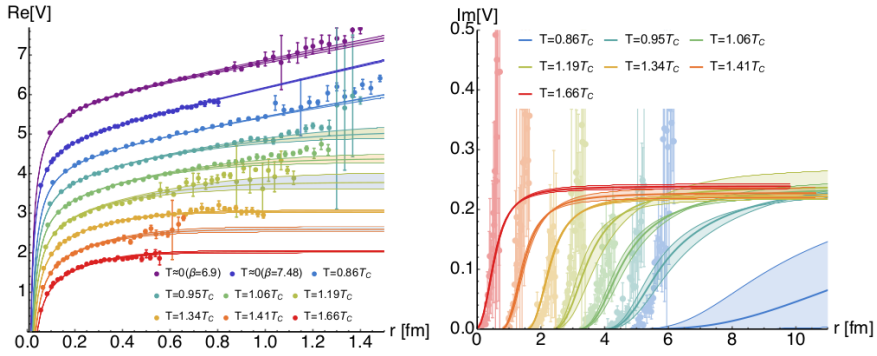

Figure 2.3: Prediction of the real-part (left) and imaginary part (right) of the in medium heavy quark potential for various temperatures [13].

Given that quarkonia survival probability is dependent on the temperature of the system we can determine the ordering of the survival in a QGP medium. The radius is inversely related to the temperature of the survival and thus one can expect the higher-mass states of a given quarkonium family, be it charmonium or bottomonium to melt at lower temperatures. In other words, there should be a sequential suppression pattern in order of increasing binding energy. Figure 2.4 show lines representing the survival of quarkonia at various values of the medium temperature, illustrating the idea that quarkonia can be used as a thermometer for the deconfined QGP phase. The quarkonia yields are suppressed sequentially in order of their binding energy.

At the highest temperature the Υ(1S) still is predicted to survive as it is the tightest

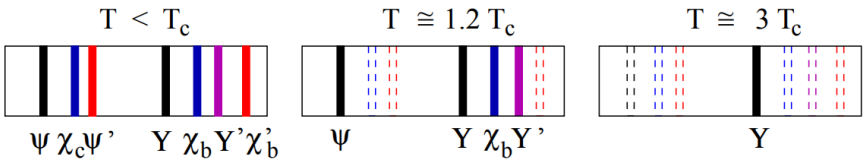

Figure 2.4: Quarkonia thermometer [14].

Table 2.1: Physical properties of the quarkonia states [14].

State	J/ψ	χ_c	ψ'	Υ	χ_b	Υ(2S)	χ_b'	Υ(3S)
Mass (GeV)	3.10	3.53	3.68	9.46	9.99	10.02	10.26	10.36
ΔE (GeV)	0.64	0.20	0.05	1.10	0.67	0.54	0.31	0.20
ΔM (GeV)	0.02	-0.03	0.03	0.06	-0.06	-0.06	-0.08	-0.07
radius (fm)	0.25	0.36	0.45	0.14	0.22	0.28	0.34	0.39

bound state with the smallest radius. Table 2.1 shows some physical properties of the quarkonia states such as mass, binding energy ΔE, and radius.

We therefore expect that quarkonia are excellent probes of the QGP phase, which are specifically sensitive to the medium temperature, as well as probes of deconfinement effects. In the rest of this work I will focus on the Υ family and the measurement of the relative suppression of the excited to ground state yields. I will compare the results obtained through this analysis with predictions from Ref. [5, 15] which incorporate some of the physics of quarkonia suppression discussed here into their models.

Chapter 3

Experimental Facilities

The data presented in this document were collected in November-December of 2015 at the CERN Large Hadron Collider (LHC) using the Compact Muon Solenoid (CMS) experiment. During this period of data taking I was able to work on the data taking, quality monitoring, and ensuring the reliability of the detector. Figure 3.1 shows a picture of me in the cavern where CMS resides with the CMS detector in the background. The following chapter describes in detail both the CERN LHC facility as well as the CMS detector and its subsystems.

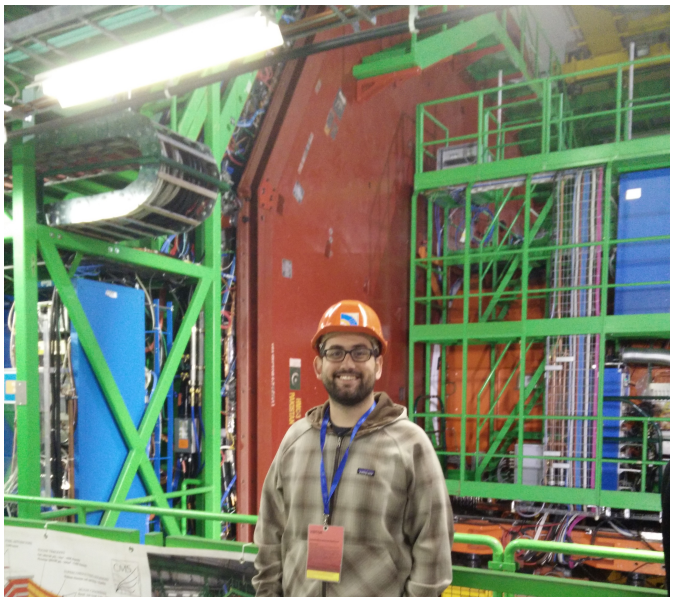

Figure 3.1: Picture of me in the CMS cavern during maintenance (beam off) in the data collection period. Picture taken by Dragos Velicanu (MIT), November 2015.

3.1 CERN LHC

The LHC is the largest particle accelerator in the world, which has achieved the current highest energy of 13 TeV for proton collisions and 5.02 TeV for heavy-ion collisions. The original design objective for the LHC was to produce the much sought-after Higgs Boson, as well as searches for beyond the standard model physics. Doing this search in a hadron collider allowed for a large reach in energy as well as minimal loss in energy due to synchrotron radiation [16]. Synchrotron radiation occurs when a charged particle is in a circular orbit or rather it has an acceleration perpendicular to its direction of motion. In such an instance, the emittance scales as the inverse of the mass and therefore larger mass hadrons will emit less radiation than smaller mass leptons, such as an electron. This is also useful for heavy-ions that can be accelerated in the same machine.

The CERN LHC is located at an average depth of 100 m underground on the border of Switzerland and France near the Jura mountains and Geneva. Located in the older Large Electron-Positron Collider tunnel, the LHC tunnel has a circumference of 27 km and two sets of accelerating rings, in the same enclosure, to accelerate beams in opposing directions which allows collisions to occur at various interaction points. At the time of this writing there are four interactions points (IP) where four separate experiments are located: A Toroidal Large LHC Apparatus (ATLAS), Compact Muon Solenoid (CMS), A Large Ion Collider Experiment (ALICE), and the Large Hadron Collider beauty (LHCb). The research presented in this paper will focus on CMS, which is located at IP5 (often referred to as P5) in Cessy, France. Figure 3.2 shows an overall view of the LHC as well as the four experiments described.

The central features of the LHC are the magnets and radio frequency (RF) cavities. These are the key components needed in order to have charged particle acceleration, a precursor to their collision.

3.1.1 Magnets

The main magnets used in the LHC consist of dipoles, multipoles, and insertion (inner triplet) magnets. It is first important to know how charged particles interact in a magnetic field. The Lorentz Force describes the motion of a charged particle with charge q in

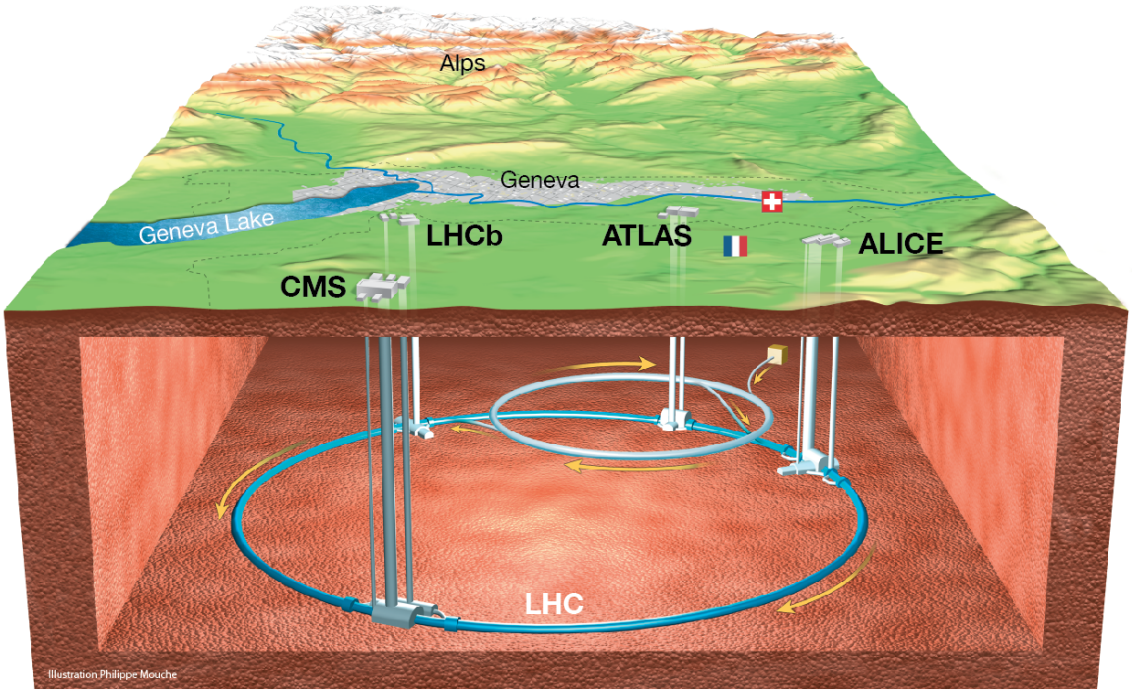

Figure 3.2: Overall view of the LHC as well as the four experiments. [17]

electromagnetic fields and is given by:

$$\vec{F} = q(\vec{E} + \vec{v} \times \vec{B}) \tag{3.1}$$

where $\vec{E}$ is the electric field, $\vec{B}$ is the magnetic field, and $\vec{v}$ is the velocity of the charged particle. Figure 3.3 shows a computer-generated image of one of the LHC dipoles and its components. The LHC contains 1232 dipole magnets that measure 15 m in length and are used to apply a magnetic field perpendicular to the motion of the hadron, causing the charged particles to move in an approximately circular orbit around the LHC ring. These magnets are electromagnets that are constructed with ≈ 160 superconducting cables and reaching a field of ≈ 8.33 T [18]. These magnets are crucial in attaining the design energy at the LHC while maintaining a circular orbit.

The multipoles at the LHC are used to focus the beam. Fig. 3.4 shows a drawing of two quadrupoles where one is used to focus or squeeze the beam horizontally while

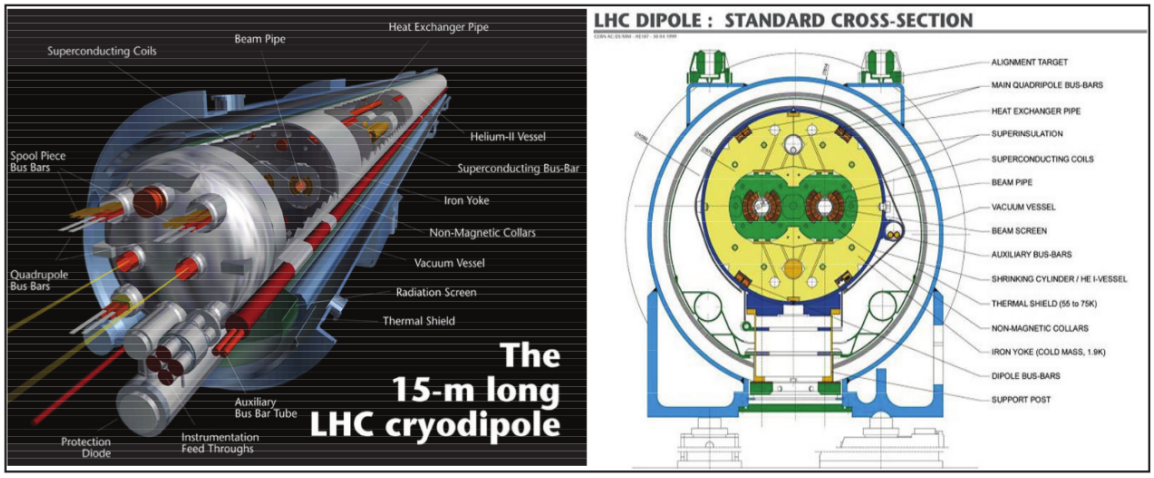

Figure 3.3: The LHC dipole magnet system. [16]

the other focuses the beam vertically. These magnets are crucial to make the bunches of colliding hadrons focused in a localized region so that when the two beams cross at an IP they have a greater probability of colliding. There are higher order magnets at the edges of the dipoles to account for small imperfections in the magnetic field at the ends. In addition to the quadrupoles for focusing the beam there also magnets needed to bring the two beams traveling in opposite directions together so that a collision can occur. There are three quadrupoles that create a system referred to as an inner triplet. Each IP has two inner triplets. These triplets squeeze each beam from ≈ 2 mm to $\approx 16\mu$m across [18].

3.1.2 RF Cavities

An RF cavity is the component that generates the acceleration of the hadrons that move throughout the LHC. They are the basis of a linear accelerator and combined with the aforementioned magnet systems are the basis of the circular collider known as the LHC. RF cavities are metal resonant chambers where an electromagnetic field is present. This field accelerates charged particles such as a proton or ion as it passes through the chamber.

"RF cavities can be structured like beads on a string, where the beads are the cavities and the string is the beam pipe of a particle accelerator, through which particles travel in a vacuum" - CERN website on RF Cavities [20].

The field in the RF cavities at the LHC is tuned to oscillate at 400 MHz. In Fig. 3.5 (left) one can see a diagram of the electric field as a function of time before and after a

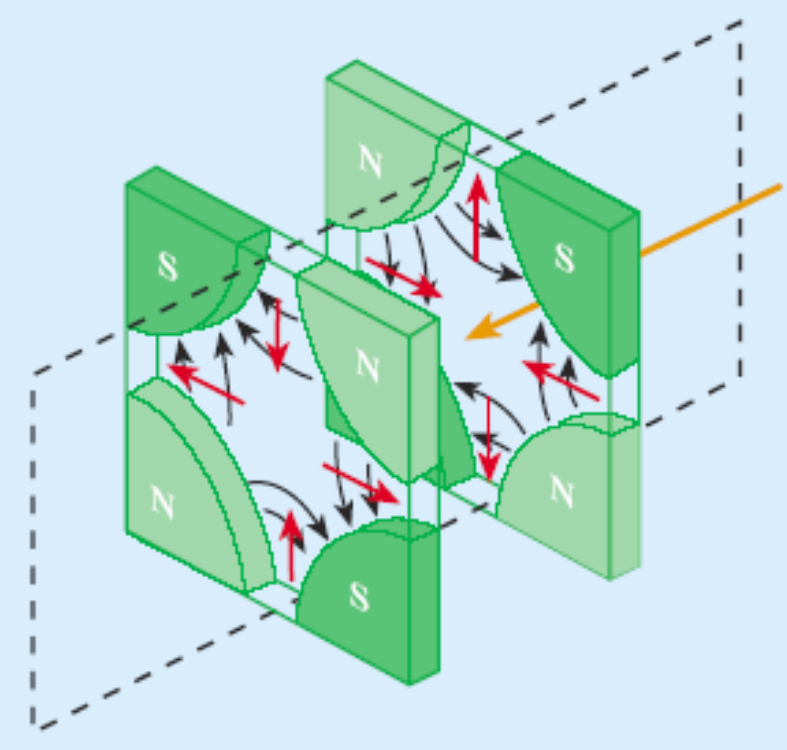

Figure 3.4: Drawing of two quadrupoles. [19]

transition through the chamber. If a particle is to arrive on time to a chamber it will feel the appropriate field, and therefore the appropriate accelerating force, and will not oscillate from chamber to chamber. Particles that arrive early will experience a smaller force, while the particles arriving late will experience a larger force. This causes the early and late particles to oscillate around the stable, on-time, particle through out the acceleration process. Once the particle has reached its peak velocity it will become stable and no longer feel a force from the RF cavities [20, 16]. Figure 3.5 (right) shows a picture of one of the LHC RF cavities underground, together with a person for scale. The LHC contains 16 RF cavities and each cavity can reach a maximum of 2 MV.

3.1.3 CERN Accelerator Complex

The CERN Accelerator Complex comprises multiple linear accelerator and rings, which utilize the previously mentioned technologies, at various stages of the acceleration of the hadrons. Figure 3.6 shows the overview of the complex and the various stages of acceleration. Protons and Ions, such as Pb, can be accelerated in this complex with slight

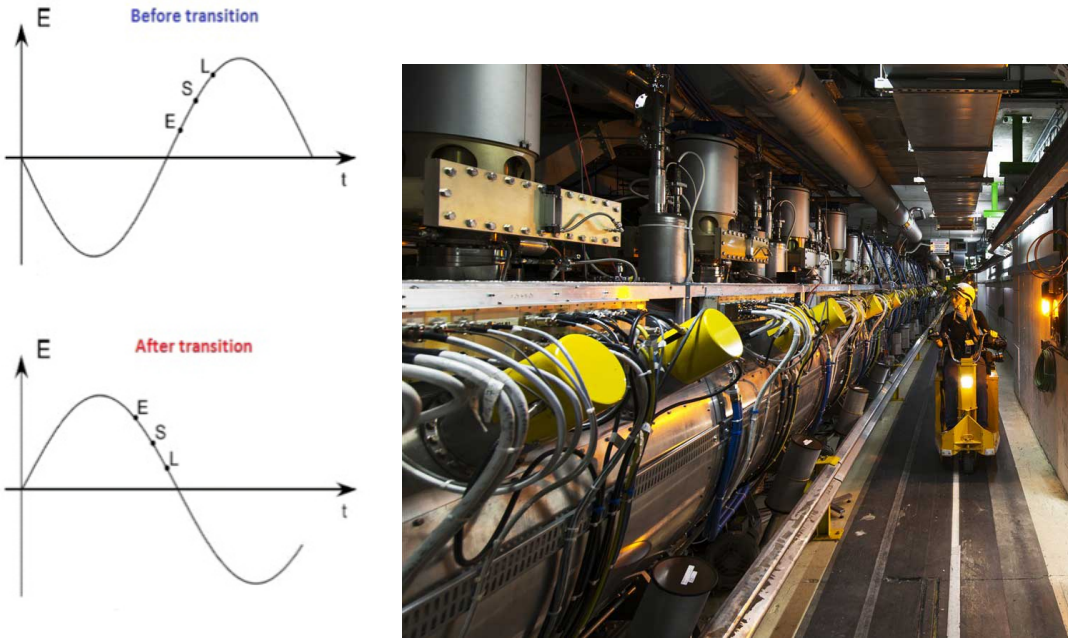

Figure 3.5: Diagram (left) of the Electric Field vs. time of various scenarios of particles in RF cavity for L (late), E (early), and S (on time) [21] and a picture (right) of one of the RF cavities at the LHC [20]

variation and operational procedure. The LHC has reached a peak center-of-mass energy of 13 TeV for proton-proton collisions which amounts to 6.5 TeV per beam and is the largest energy of colliding protons to date. For heavy ions, the LHC has reached the center-of-mass energy per nucleon pair of 5.02 TeV for Pb ions. This amounts to 2.51 TeV per nucleon. The design energy of the LHC was set to deliver 14 TeV proton collision and correspondingly 5.5 TeV Pb collisions. This goal has yet to be reached due to magnet and luminosity constraints.

To start the acceleration of protons, the collider physicists and engineers start with a bottle of Hydrogen gas. This Hydrogen gas comes in contact with an applied electric field that strips the electron from each atom, thus creating protons of positive charge. The protons then go through the following chain [22, 23]:

- Linac 2 - energy gain of 50 MeV;
- Proton Synchroton Booster (PSB) - accelerates to 1.4 GeV;

- Proton Synchroton (PS) - accelerates to 25 GeV;
- Super Proton Synchroton (SPS) - accelerates to 450 GeV;
- LHC- accelerates to desired energy (6.5 TeV maximally) 2.51 TeV per nucleon for Pb beams used in this analysis.

The lead ion acceleration starts with a solid piece of lead 2 cm in length and with a mass of $\approx$ 500 mg. This sample is heated to 500 °C in order to vaporize it and let off some small fraction of the atoms. The atoms are exposed to an electrical current in order to ionize a few electrons, thus creating a Pb ion. The Pb ions then go through the following chain [24, 25]:

- Linac 3 - energy gain of 4.5 MeV per nucleon;
- Low Energy Ion Ring (LEIR) - accelerates to 72 MeV per nucleon;
- Proton Synchroton (PS) - accelerates to 5.9 GeV per nucleon;
  - Pb^{54+} is stripped by a 0.8 mm aluminum foil to reach final ionization of Pb^{82+};
- Super Proton Synchroton (SPS) - accelerates to 177 GeV per nucleon;
- LHC- accelerates to 2.51 TeV per nucleon.

3.2 CMS (Compact Muon Solenoid)

Once proton and lead acceleration is achieved and collisions occur at the four interaction points, we need a way to measure the final state particles that are produced. The CMS detector at P5 in Cessy, France is located in a cavern $\approx$ 100 m underground in the LHC tunnel. This detector was named thus due to its emphasis in measuring muons that originate from the collision. The main feature of CMS is a superconducting solenoid with 6 m internal diameter and a magnetic field of 4 T. Inside of the solenoid there are a silicon tracker (pixel, strip), electromagnetic calorimeter, and hadronic calorimeter, each having a barrel and endcap components. On the outer portion of the solenoid resides the

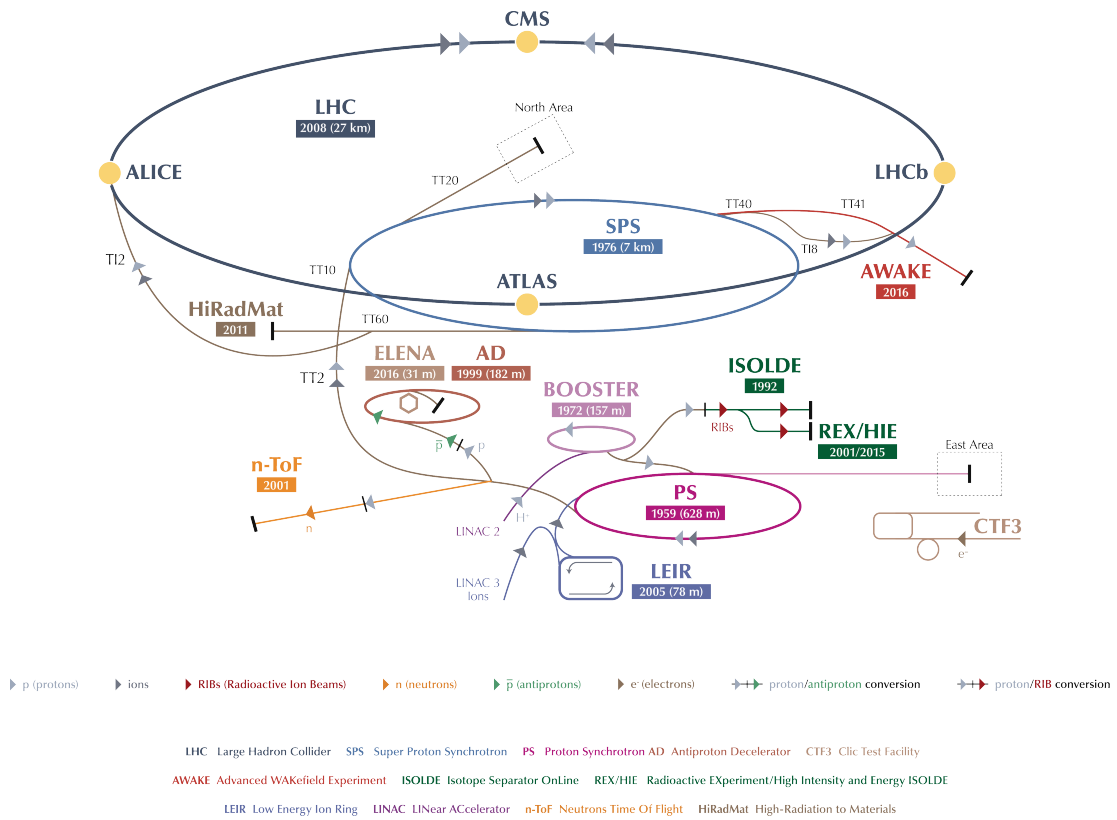

Figure 3.6: Overview of CERN Accelerator Complex [26]

muon detector in the endcaps and barrel. In the forward region there exists a hadronic calorimeter that is particularly useful in studying heavy-ion collisions. The rest of this section will discuss each of these components that form the basis of the CMS detector.

During design and construction of CMS the key goals of the detector (as motivated by LHC physics) were itemized in Ref. [28] and presented here for convenience:

- Good muon identification and momentum resolution over a wide range of momenta and angles, good dimuon mass resolution ($\approx 1\%$ at 100 GeV), and the ability to determine unambiguously the charge of muons with $p < 1$ TeV;

- Good charged-particle momentum resolution and reconstruction efficiency in the inner tracker. Efficient triggering and offline tagging of τ's and b-jets, requiring pixel detectors close to the interaction region;

- Good electromagnetic energy resolution, good diphoton and dielectron mass resolu-

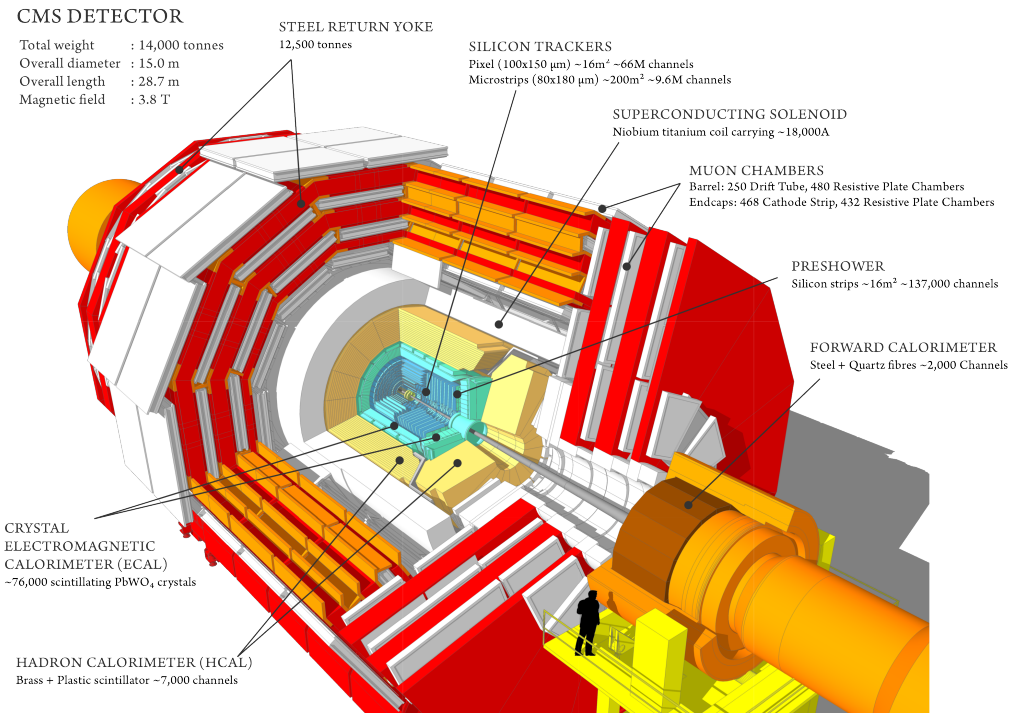

Figure 3.7: Overview of the CMS detector with a sectional wedge removed to show the inner and outer components [27].

tion ($\approx 1\%$ at 100 GeV), wide geometric coverage, π^0 rejection, and efficient photon and lepton isolation at high luminosities;

- Good missing-transverse-energy and dijet mass resolution, requiring hadron calorimeters with a large hermetic geometric coverage and with fine lateral segmentation.

3.2.1 CMS Coordinate System

The CMS detector uses a coordinate system that is right-handed and is described in terms of z, η and ϕ. The z coordinate describes the direction of the beam line and ϕ is the azimuthal angle in the $x - y$ plane that goes from 0 to 2π. The pseudorapidity (η) variable is another description of θ, where θ is defined from 0 to π, that is convenient in particle collider physics and is defined as:

$$\eta = -\ln[\tan(\theta/2)] \tag{3.2}$$

Figure 3.8 shows this coordinate system description and its relation to the x, y, z system that many are accustomed to. The x-coordinate points to the LHC center while the y-coordinate points up.

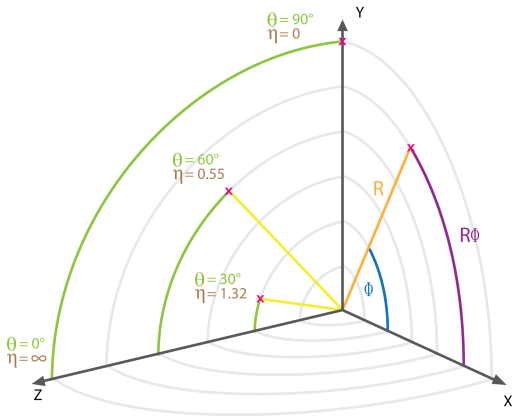

Figure 3.8: CMS coordinate system with the $x-y$ plane being the transverse to the beam and z being the beam direction [29].

3.2.2 Superconducting Magnet

The superconducting solenoidal magnet is a key feature to the detection of charged particles at CMS. Through the same physics described in Equation (3.2), the charged particles are bent in a magnetic field. The measured curvature in the detector, together with the knowledge of the B field, is used in the determination of the particles momentum. The magnet system consists of a superconducting solenoid that can produce a 4 T field. To achieve this there are 4 layers of winding made out of NbTi conductor. This solenoid is housed in the cold mass vacuum vessel with a 6.3 m internal diameter [28]. In addition to this solenoid system, CMS has a return yoke made of iron in order to maintain a strong uniform field outside of the solenoid to provide curvature for particles outside the magnet (mainly muons). During the commissioning of the CMS detector, the magnet was switched to operate at 3.8 T rather than 4 T due to safety concerns and with the goal of increasing the magnet lifetime [30]. The 3.8 T field has become the de facto operating field for the magnet. A picture of this system can be seen in Fig. 3.9.

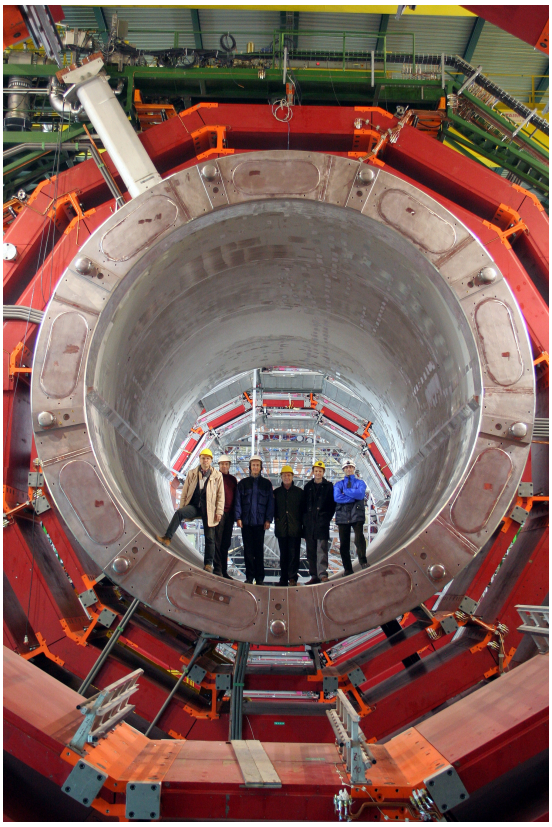

Figure 3.9: Picture of the superconducting solenoid (silver) and the iron return yoke (red) during construction [31]. For scale CMS members from CERN CMI group and of Saclay are standing on the vacuum vessel which contains the coils.

3.2.3 Silicon Tracker

The innermost part of the CMS detector is where the tracking system resides. This is the largest silicon tracking system ever built. The tracking system contains two type of technologies (pixel, strip) both made of silicon because of the granularity, speed, and radiation hardness. This is ideal considering the detector should have a large lifetime of $>$ 10 years in line with the magnet design lifetime. The environment is also radiation harsh, where at design luminosity there are $\approx$ 1000 particles from 20 overlapping proton collisions incident on the detector. This particle number is increased in heavy-ion operation. Therefore, silicon is the current optimal choice for the tracking system [28]. Figure 3.10 shows a cross section of the tracking system for both the pixel and strip detector. The pixel system has three barrel layers at locations $4.4 - 10.2$ cm and two disks at the endcaps. The strip detector contains ten barrel layers extending out to a radius

of 1.1 m as well as three inner endcap disks and 9 outer endcap disks. The tracking system has a coverage of $|\eta| \leq 2.5$. The technology of the silicon tracking system is such that it can easily detect charged particles that pass through and quickly reconstruct their positions while minimally perturbing their path. The analysis contained in this document is in particular interested in the measurement of muons. Figure 3.11 shows the resolution of single muons at 1, 10, and 100 GeV. The leftmost panel shows that the transverse momentum (p_T) resolution degrades with increasing values of η, but typical values are in the range $\sim 1\%$, providing excellent momentum resolution for dimuons in the kinematic region of this analysis.

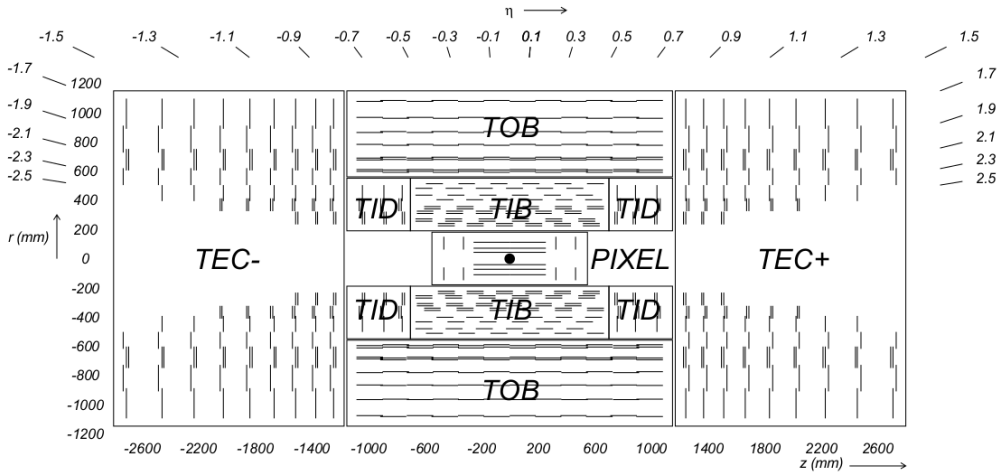

Figure 3.10: Cross section of the tracking system where each line represents a detector module and the double lines indicate a back-to-back module from [28]

3.2.3.1 Pixel detector

The pixel detector system is located closest to the beam pipe. It is excellent for primary vertex and secondary vertex reconstruction of collisions. The pixel detector contains 65 million pixels in total. Figure 3.12 shows a drawing of the pixel model with the sensors and read out chip. Each pixel cell has the dimensions of 100 μm $\times$ 150 μm with the barrel region containing three layers at radii of 4.4, 7.3, and 10.2 cm. The endcap portions of the pixel detector contain four disks at $z = \pm 34.5$ cm and $z = \pm 46.5$ cm. The pixel sensor comprises n-on-n technology which allows for the detector to be operating as partially depleted, a preventative measure in case the sensor becomes damaged from radiation [28,

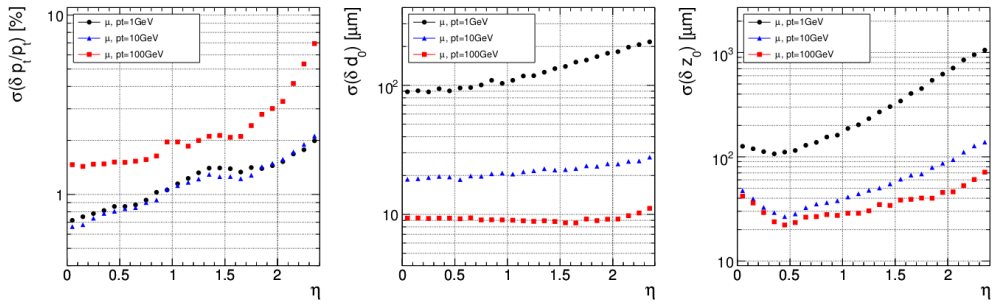

Figure 3.11: Single muon resolution for muons with transverse momenta of 1 (black points), 10 (blue points), and 100 GeV (red points). The resolution is shown for transverse momentum (left), transverse distance of closest approach (middle), and longitudinal distance of closest approach (right) from [28]

32, 33].

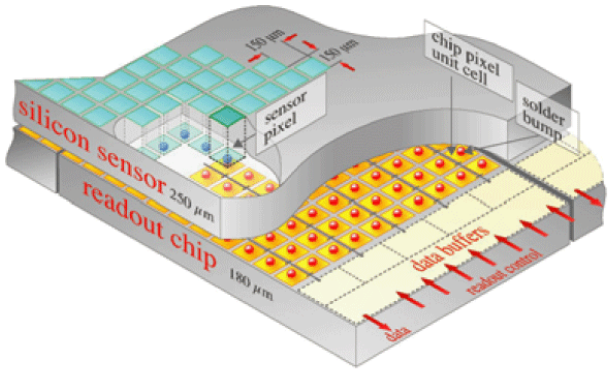

Figure 3.12: Drawing of a pixel module with the sensor and read out chip [32]

The barrel portion of the detector is visible in Fig. 3.13 (left) while the turbine-like endcap can be seen in Fig. 3.13 (right). The endcap structure has planes tilted at 20° to help induce charge sharing among pixels. As radiation damage occurs, the pixel depletion depth and/or the increase in bias voltage leads to reduction in charge sharing. This causes a reduction in the spatial resolution which can be resolved by allowing the sharing to occur thanks to the introduction of the turbine structure in the design of the endcap. The spatial resolution of the pixel detector is 15-20 μm [28].

3.2.3.2 Silicon Strip detector

The silicon strip detector is the outermost part of the tracking system. It encloses the pixel detector, as shown in Fig. 3.10, and is composed of four cylindrical shells of the tracker

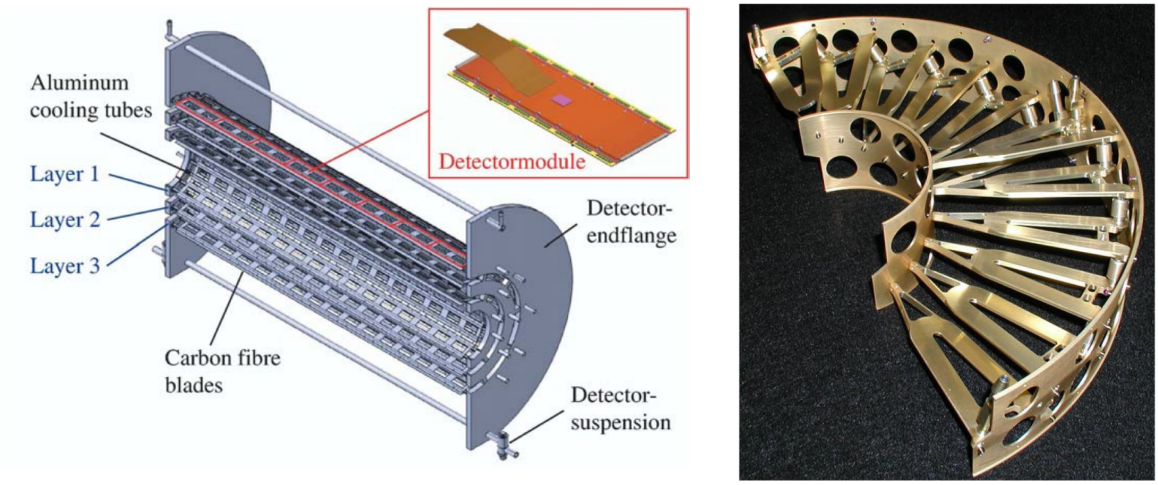

Figure 3.13: Drawing of barrel pixel detector support structure and detector module (left) and a picture of the endcap turbine-like support structure (right) [28].

inner barrel (TIB) closed off by the two inner endcaps composed of three tracker inner disks (TID). The outermost part contains the six outer barrel (TOB) concentric shells and is closed off with the tracker endcap (TEC) that contains nine disk layers. Figure 3.14 shows a picture of the inner barrel strip modules with the pixel system inside. The technology for the sensors in the strip modules is composed of p-on-n substrate design. The sensors were built on a substrate with a (100) crystal orientation denoting the Miller indices. During testing it was found that using (100) was preferred over (111) due to the fact that the (100) builds up less surface charge from irradiation. The strip tracker contains 24,244 sensors of various geometries and 9.6M readout channels [28, 34, 35]. Similarly to the pixel detector, the strip detector obtains "hits" which allow us to determine the location of the charged particle that passes through a given silicon detector. This location information allows us to then determine the momentum of the particle. When the charged particle passes through the detector, a small current is formed which lasts on the order of 1 ns and is amplified in order to be read out. Combining the information from the pixel and strip detector allows accurate measurement of a charged particle track through the detector out to a radius of 130 cm from the beam line.

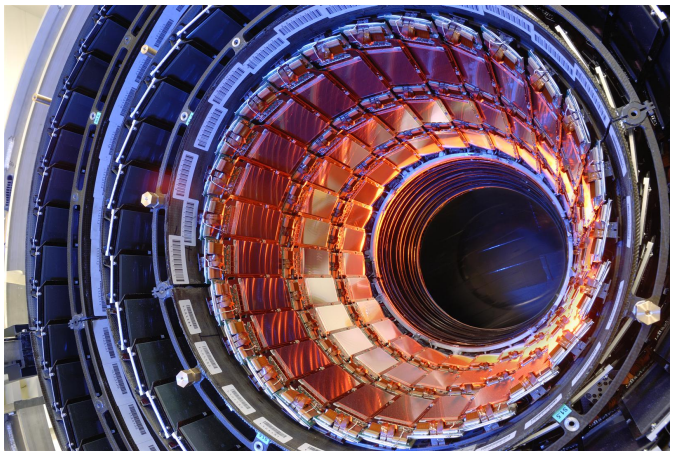

Figure 3.14: A picture of the silicon tracker with the inner barrel strip detector visible [28].

3.2.4 Electromagnetic Calorimeter

The Electromagnetic Calorimeter (ECAL), which measures the energy of an incident particle, resides outside the tracking system. The ECAL is made of lead-tungstate ($PbWO_4$) crystals. There are 61,200 crystals in the barrel region and 7,324 in the endcap regions. The $PbWO_4$ crystal is ideal for the design of an ECAL due to its large density and short radiation length: 8.28 g/cm^3 and 0.89 cm respectively. The ECAL is hermetic and has a coverage of $|\eta| < 1.479$ in the barrel region and $1.479 < |\eta| < 3.0$ in the endcap region. When an electromagnetically-interacting particle, in most interesting cases an electron or photon, is incident upon the crystal, the energy of the particle will be converted into light due to the scintillation properties of $PbWO_4$. In order to collect the light created, the crystals are first polished to achieve total internal reflection and minimal loss in light collection. The crystals are housed with photodectors at the end: avalanche photo-diodes (APDs) in the barrel and vacuum phototriodes (VPTs) in the endcaps. The dimensions of each crystal are 22×22 mm^2 at the front face and 26×26 mm^2 at the back face with a total length of 230 mm. Figure 3.15 shows crystals from the barrel and the endcap with their appropriate photodetectors attached. The figure also displays the difference between an unpolished and a polished crystal [28, 36]. When combined with information from the tracker, the ECAL + tracker can help discriminate photons from electrons, as the photons will not be detected in the tracker.

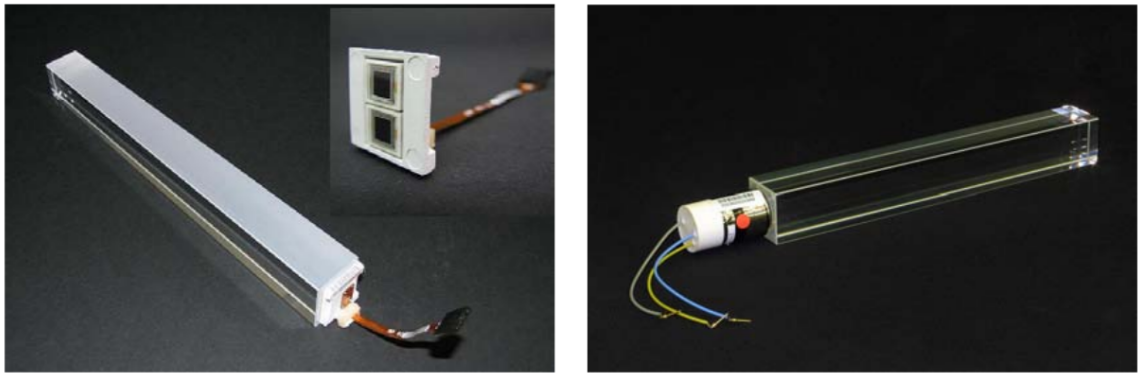

Figure 3.15: Single crystals of $PbWO_4$ with an unpolished barrel crystal containing an attached APD (left) and a polished endcap crystal with a VPT connected (right) [28].

3.2.5 Hadronic Calorimeter

The Hadronic Calorimeter (HCAL) is located on the outside of the ECAL and includes a hermetic barrel and endcap region. Figure 3.16 shows the barrel portion of the HCAL being lowered in the CMS cavern. The barrel region covers $|\eta| < 1.3$ while the endcap region covers $1.3 < |\eta| < 3.0$.

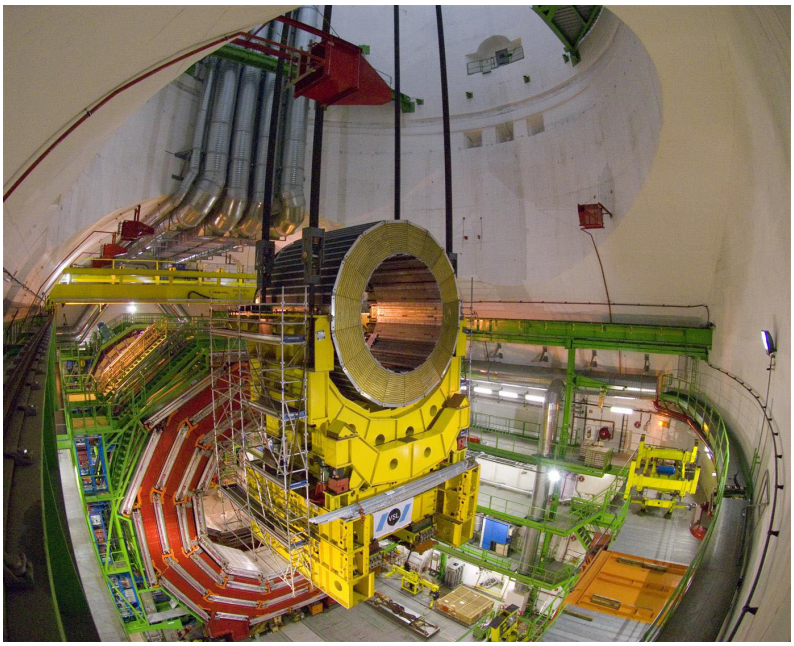

Figure 3.16: The HCAL Barrel on the plus side being lowered in the CMS cavern in 2007 [37].

The HCAL measures energy of hadrons, particles made of quarks and gluons, as

well as non interacting particles, such as neutrinos, via missing energy. During a collision, non-charged, non-interacting particles get measured via conservation of energy and momentum. We can deduce the missing energy and its location thus allowing the measurement of neutrinos. The HCAL is a sampling calorimeter made of alternating layers of brass absorber plates and plastic scintillators. The brass absorber is composed of 70% Cu and 30% Zn. Interestingly, the portion of the HCAL in the endcaps used brass that was collected from more than a million World War 2 cartridge shells from the Russian Navy [28, 38]. When a hadron traverses the HCAL it first collides with nuclei in the absorber and produces secondary particles. These particles travel through the scintillator and produce light that is collected by wavelength-shifting fibers and sent for processing. This process continues as particles that do not interact in the first region will undergo particle production in the next absorber layer, producing secondary particles that produce light signals in the next scintillator layer, creating what is known as a shower.

3.2.6 Muon System

As the name suggests, the Compact Muon Solenoid is an excellent muon detector by design. The outer portion of the superconducting solenoid is the iron return yoke and alternating layers of the muon detection system. During the design of CMS, the four-lepton channel for the Higgs boson decay was a high scientific priority, thus creating an excellent capability for measuring muons. Muons are good final state particles to use in an analysis of a process in heavy-ion collisions because they are fairly clean probes that interact electromagnetically and will not be affected by the QGP. Their cleanliness can also be attributed to their ability to penetrate the inner parts of the detector while minimally interacting until they reach the outermost region of CMS, where only the muon system and the iron return yoke of the magnet resides. Figure 3.17 shows the stopping power, $\langle -dE/dx \rangle$, of muons incident on copper as a function of the muon momentum. The Bethe region is the region of momentum of most interest in the analysis presented in this paper, where at lower p_T the muon is minimum ionizing and at large p_T small radiative effects begin to occur. This property of muons allows them to penetrate the medium of the detector with very little perturbation or loss in energy, thus making them

excellent final state probes.

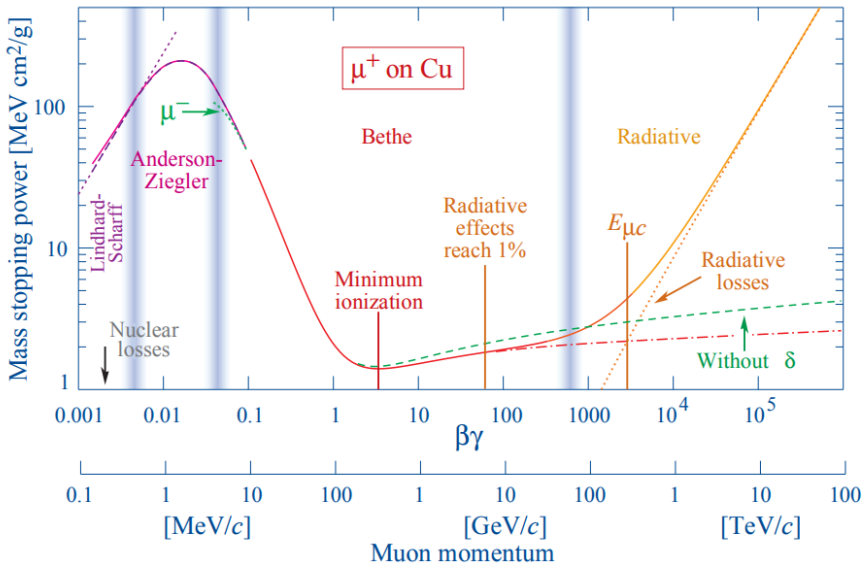

Figure 3.17: Stopping power, $\langle -dE/dx \rangle$, of muons incident on a copper target as a function of muon momentum [2].

Figure 3.18 shows a wedge of the CMS detector in the transverse plane. The light blue line represents a muon and it clearly exhibits the characteristic curvature of a charged particle. It is also noticeable that the magnetic field in the inner part of the solenoid is in an opposing direction to that on the outer part, as seen by the change in radius of curvature of the blue track, which is a distinct property of solenoidal magnetic fields. The other particle tracks shown in the figure display how clean the muons are given that all electrons, photons, and most hadrons are stopped, not including punch through or non-interacting neutrinos.

The muon systems were designed to provide excellent muon identification, momentum measurement, and triggering. The muon system is composed of three different gaseous detectors: Resistive Plate Chambers (RPC), Drift Tubes (DT), and Cathode Strip Chambers (CSC) [28]. Figure 3.19 shows a cross section of the CMS detector in the $r-z$ plane. The detector is symmetric about z (through full ϕ rotation) and r as this cross section is for the purposes of facilitating its visualization. The three muon systems are displayed in the this figure, with the CSCs (green) in the endcap region, DTs (tan) in the barrel, and RPCs (blue) covering both the barrel and endcap region of the detector. These three

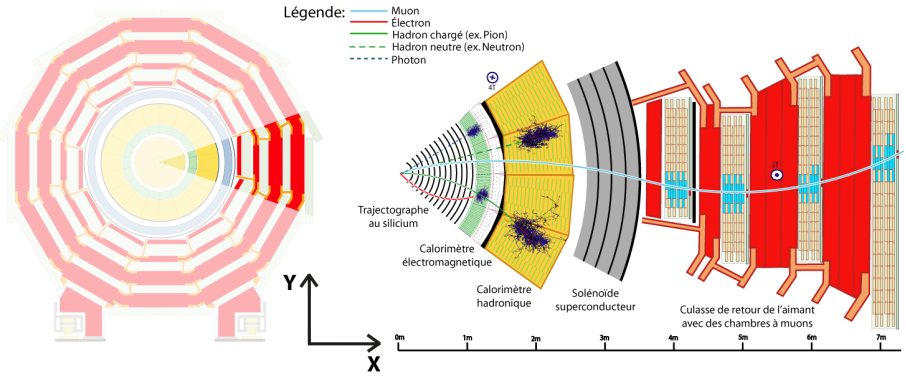

Figure 3.18: CMS wedge slice in the transverse plane showing the interactions of various particles in the detector. [39].

types of detector technologies will be discussed in the following subsections.

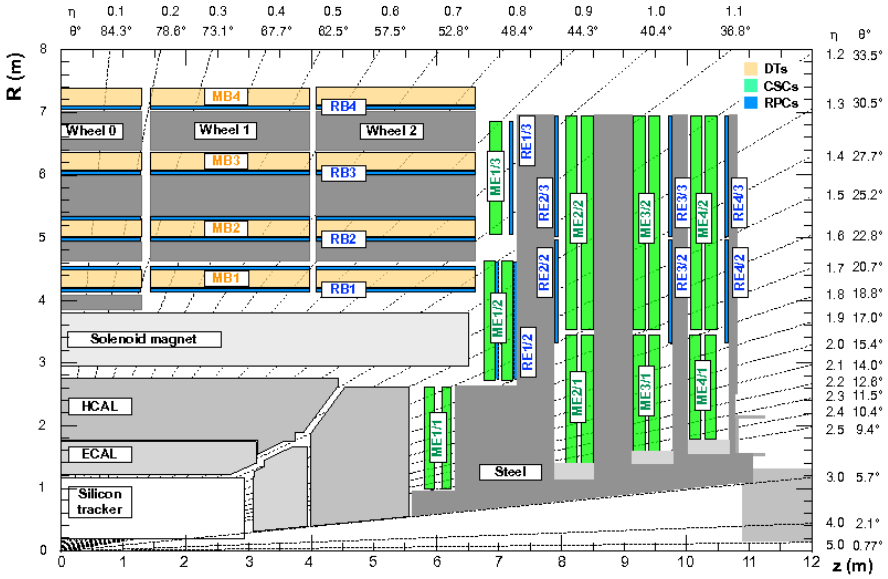

Figure 3.19: Cross section of CMS detector displaying the coverage of the various muon systems [40].

3.2.6.1 Drift Tubes (DT)

The DT detector covers the pseudorapidity range of $|\eta| < 1.2$ ("barrel") and contains four stations of concentric cylinders that alternate between the return yoke. The basic design of the drift chamber is a rectangular box with cathode side-walls, an anode wire in its center, and containing an Ar/CO_2 gas mixture. The first three stations are used

in measuring the position in the $r-\phi$ plane as well as the longitudinal z direction while the final station provides just the $r-\phi$ information. The inner three stations contain 60 drift chambers while the outermost station has 70 chambers. Each chamber contains 2-3 super layers which are each made of 4 layers of rectangular drift cells staggered by a half cell. The outer 2 super layers contain wires that are parallel to the beam line in order to extract the $r-\phi$ position. The innermost super layer of a chamber has wires perpendicular to the beam line in order to get the z position. Figure 3.20 shows a sketch of a single cell with a muon passing through [28].

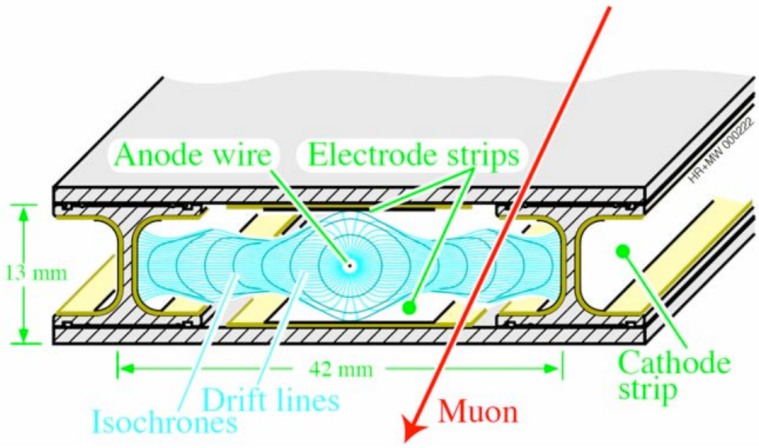

Figure 3.20: A single DT cell with a muon passing through (red), inducing a charge and signal on the wire in center [28].

3.2.6.2 Cathode Strip Chambers (CSC)

The CSC detector covers the pseudorapity range $0.9 < |\eta| < 2.4$ ("endcap") and contains four stations perpendicular to the beamline and alternating with the return yoke at each end of the CMS detector. The CSC provide a precise measurement of the position in the $r-\phi$ plane. Each CSC station is composed of a disk of chambers. There are 36 (or 72) chambers in each disk plane and 540 in total. The individual chambers are trapezoidal multiwire proportional chambers containing 6 anode wire planes and 7 cathode panels. The wires run azimuthally while the cathodes are milled into panels and run lengthwise at constant ϕ widths. The gas mixture used in each chamber is 40% Ar, 50% CO_2,

and 10% CF_4. The CO_2 allows for large gas gains while the CF_4 prevents the wires from polymerizing [28]. Figure 3.21 (left) shows the trapezoidal design and position of cathodes and strips orthogonal to each other, as described, hence allowing for 2-D information (r, ϕ) to be collected. Figure 3.21 (right) depicts a CSC chamber with a muon passing through it. When a muon passes through a CSC chamber it ionizes electrons from the gas which collect on the anode wire. The negatively-charged ions then move away from the wires and induce a charge on the cathode strips.

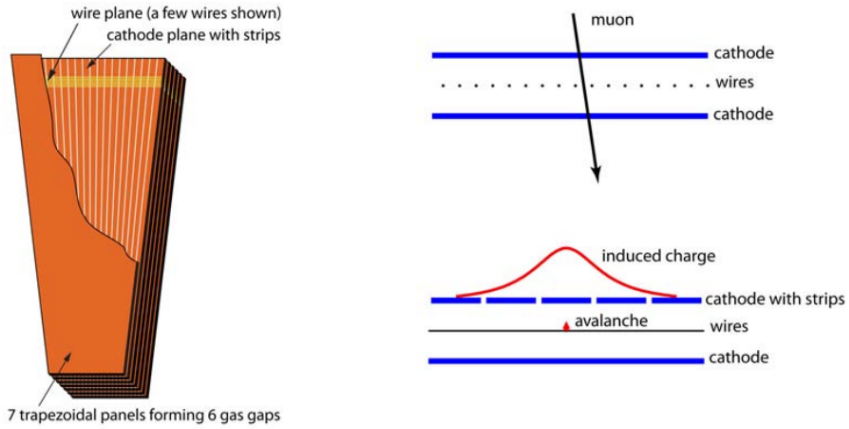

Figure 3.21: Sketch of the CSC chamber design (left) and depiction of the cathode strip induce charge and anode avalanche as a muon passes through a single detector [28].

During the data taking for this analysis in 2015, I was able to work at CERN providing quality monitoring and detector on-call service to the CSC system in which the voltage, temperature, pressure, signal from the wires/strips, and overall condition of this system was taken into account to ensure the best quality data were taken. Figure 3.22 shows a picture of Pieter Everaetes and I discussing the operation of the CSC system while on shift at P5.

3.2.6.3 Resistive Plate Chambers (RPC)

With the DT and CSC systems in place, CMS can both measure the position of muons accurately and can also trigger on the muon p_T, independent of all other CMS subsystems with rather good efficiency and background rejection. Since there is some uncertainty in the eventual background rates and the ability to measure the correct beam-crossing time

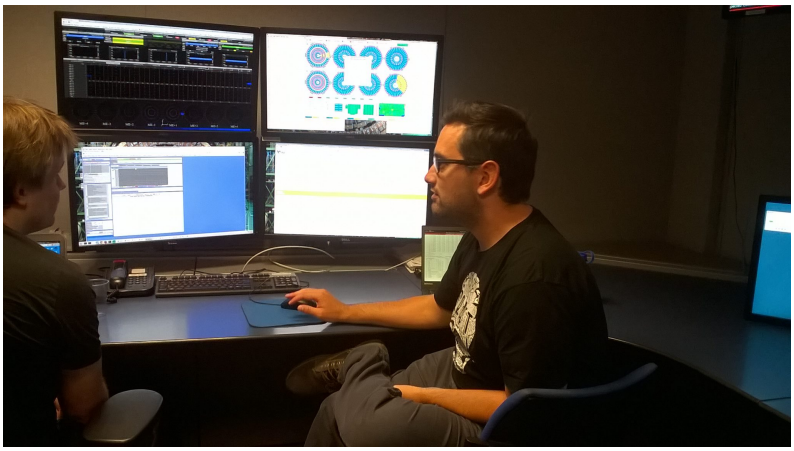

Figure 3.22: Picture of Pieter Everaetes of UCLA/CERN (left) and I (right) discussing a CSC timing study. Picture taken by Evan Wolfe (UVA), August 2015.

once the LHC is at full luminosity, another detector dedicated to triggering was created. This detector system is known as the Resistive Plate Chamber (RPC). RPCs cover a pseudorapidity of $|\eta| < 1.6$, and are faster at triggering than the CSC/DT but have poorer position resolution. The RPC is comprised of 6 layers in the barrel region, 2 in the first 2 stations, and 1 in the last 2 stations. The redundancy in the first two stations allows for the triggering to work even on low p_T muons that could stop sooner. In the endcap there are 4 RPC planes. The RPCs can *tag* the event, in a time shorter than 25 ns between consecutive LHC bunch crossings. This is the key to having the RPC as a dedicated trigger: to initially identify the location and timing information of muon candidates in a bunch crossing. The RPCs are a basic double gap module operated in avalanche mode with readout strips in between. In other words, one gap consists of two parallel plates, cathode and anode, separated by a gas volume. When a muon passes through the detector electrons are knocked off the gas atoms which then hit other atoms, causing the avalanche of electrons which then get picked up at the strips [28, 41]. Figure 3.23 shows the RPC strips with a single gap side on the bottom.

3.2.7 Hadronic Forward Calorimeter

The Hadronic Forward (HF) Calorimeter is located at both ends of the CMS detector at a shallow angle over pseudorapidity $2.9 < |\eta| < 5.2$. This detector system must be robust

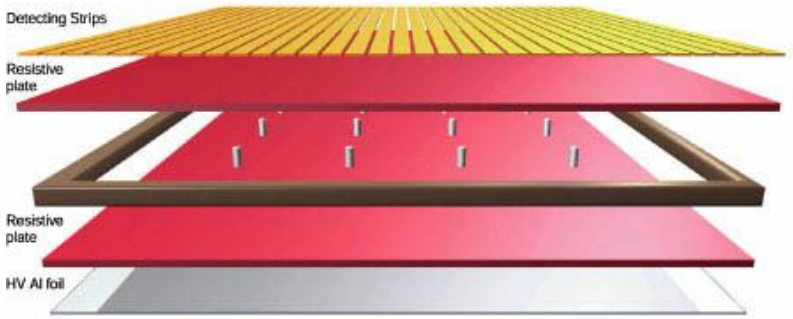

Figure 3.23: Design and layers of a single Resistive Plate Chamber single gap [41].

as it takes the largest particle energy flux of all detectors from a given LHC collision. The calorimeter is made of 5 mm thick grooved steel absorber plates and quartz fibers inserted in the grooves of the absorber. Half of the fibers are inserted into the full length of the absorber (165 cm) while the other have a depth of 22 cm. The two sets of fibers are read out separately and used to distinguish between photon/electron and hadron showers. A photon or electron will deposit a large portion of their energy in the first 22 cm thus allowing this distinction. When particles are incident on the HF detector the light signal is propagated through a quartz fiber and collected by a photomultiplier tube for amplification and read-out. For the purposes of this analysis, the HF Calorimeter is used to determine the transverse energy (E_T), centrality, in a heavy-ion collision [28]. The centrality is a measure of how two nuclei are incident upon eachother in a collision. When the two nuclei collide at a small impact parameter they produce more energy. The measurement of the energy in the HF and our knowledge of how much energy is deposited for a given impact parameter, the geometry of the colliding nuclei can be deduced and therefore the centrality. This will be discussed in more detail in the following chapter. Figure 3.24 shows a cross section of the HF calorimeter and its components along with the shielding and dimensions. In the next chapter I will go on to discuss the collection and quality selection process of data measured using the CMS detector.

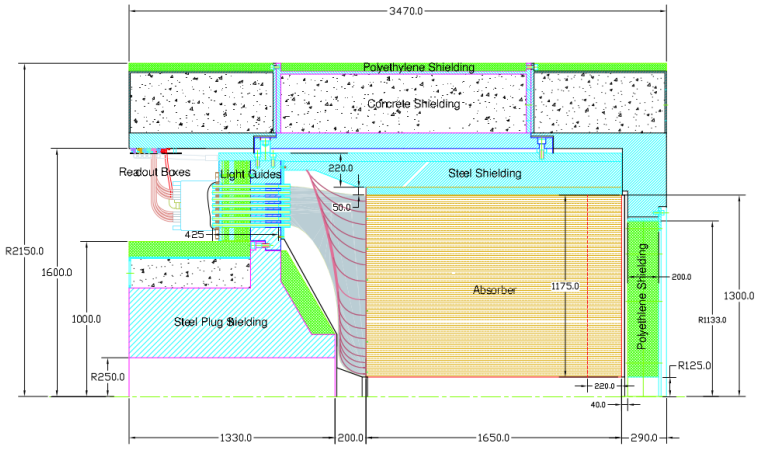

Figure 3.24: Cross sectional view of the HF calorimeter. The fibers are shown as the grey shaded region and the absorber as labeled is the tan region. [28].

Chapter 4

Data Selection and Simulation

The heavy-ion collision data used in this analysis originates from the November-December 2015 run at the CERN LHC. During this data-taking period, CMS collected an integrated luminosity of 28.0 pb^{-1} of $p+p$ data. After the initial collection of $p+p$ data, CMS collected an integrated luminosity of 464 pb^{-1} of Pb+Pb collision data (which will be referred to in this thesis as the Peripheral data set) and another sub-sample with integrated luminosity 368 pb^{-1} (which will be referred to as the DoubleMu0 data set). The $p+p$ and Pb+Pb collision data were taken at the center-of-mass energy per nucleon pair of $\sqrt{s_{\text{NN}}} = 5.02$ TeV. Additionally, for the evaluation of efficiencies and acceptance corrections related to these data, Monte-Carlo (MC) simulations of similar events and reconstruction algorithms were generated and studied. In this chapter I discuss data collection, triggering, simulation, and event selection.

4.1 Datasets

This analysis uses the prompt Analysis Object Data (AOD) datasets of $p+p$ and Pb+Pb collisions. Prompt AOD refers to the dataset type being prompt processing and the format structure of the file being in AOD which can be directly used for physics analysis. AOD is a subset of the Reconstructed (RECO) data without the digi information. Figure 4.1 graphically details the various subsets of data storage types. It is clear from the figure that AOD is a subset of RECO which is also a subset of RAW data. This AOD format already contains high level reconstructed objects such as muons, electrons, as well as

certain detector qualities of these objects in order for us to then apply criteria based on these quantities, as explained below.

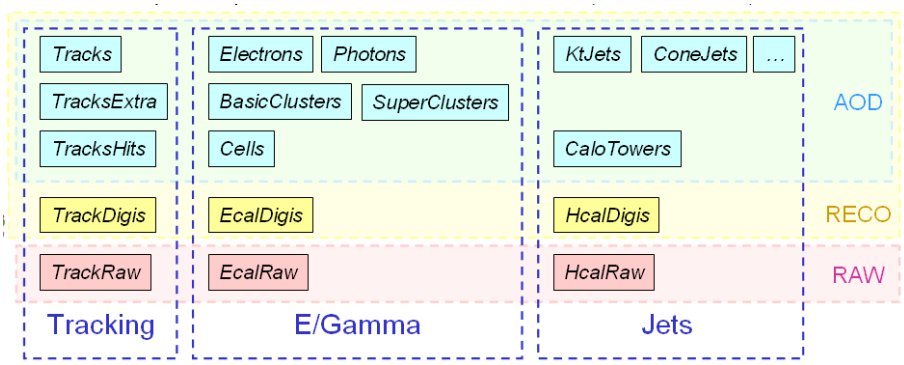

Figure 4.1: Diagram comparing data tier processing formats for AOD (green), RECO (yellow), and RAW (pink) [42].

The datasets were then processed in the CMS Software (CMSSW) version `CMSSW_7_5_X` with the following global tags:

- Pb+Pb data: `75X_dataRun2_PromptHI_v3`
- $p+p$ data: `75X_dataRun2_Prompt_ppAt5TeV_v1`

In order to be sure that the data being used/processed are of the greatest quality, a JSON file was used to mask runs and luminosity sections that were noted as bad for either detector or triggering failures. The JSON (specially formatted text file) files used for this analysis are:

- Pb+Pb : `/afs/cern.ch/cms/CAF/CMSCOMM/COMM_DQM/certification/Collisions15/HI/Cert_262548-263757_PromptReco_HICollisions15_JSON_MuonPhys_v2.txt`
- $p+p$: `/afs/cern.ch/cms/CAF/CMSCOMM/COMM_DQM/certification/Collisions15/5TeV/Cert_262081-262328_5TeV_PromptReco_Collisions15_25ns_JSON_MuonPhys.txt`

The analysis of the dataset starts with running it through the forked branch of `CMSSW_7_5_X` located at:

`https://github.com/CMS-HIN-dilepton/cmssw/tree/Onia_HI_75X`

In this git repository reside two important sub-directories notably the `HiAnalysis/HiOnia`

(Analyzer) and the `HiSkim` (Skimmer). In order to process the data as described with the above criteria one first has to skim the data, a process that cleans it from unwanted events and then run the analyzer on the resulting skimmed files to put it in a reasonable format for all users. The `HiSkim/HiOnia2MuMu/test/` directory contains the `onia2MuMuPATHI_7xy_PbPbPrompt_cfg.py` which is used to skim the initial dataset to a more manageable size while preserving the formatting. The `HiAnalysis/HiOnia/test/` directory contains the `hioniaanalyzer_PbPbPrompt_cfg.py` which is used to reformat the skimmed data files and do some light skimming and analysis.

Once these steps have been achieved the so-called `OniaTrees` will have been formed. These trees are used for all parts of the analysis and can be used on the laptop of any user given the proper ROOT and compiler versions. The code used to form this analysis is located on my personal github at:

`https://github.com/xadflores/UpsilonAna_Run2`

This code is meant to run over the OniaTrees of types data and MC depending on the specific macro options.

4.2 Triggering

The CMS trigger system consists of a Level-1 (L1) hardware programmable electronics trigger and a High Level Trigger (HLT) software trigger processed in a farms of commercial processors. The L1 trigger can access the coarse information from the calorimeters and muon system while the HLT trigger has all readout information. The L1 triggers are based generally on energy deposited in a calorimeter or hit patterns/track segments in the muon chambers. Figure 4.2 shows the architecture of the L1 triggering system. The purple side with muon system information, the 4μ denotes a 4 muon trigger decision.

The analysis presented in this work focuses on detecting muons. Therefore further discussions in this paper will focus on this aspect of CMS. The CMS muon trigger uses all three muon detector systems: CSC, DT, and RPC. The CSC provides 3-dimensional track segments to its local trigger while the DT chambers provide track segments from the ϕ projection and hit patterns from the η projection to its local trigger. The RPC detectors

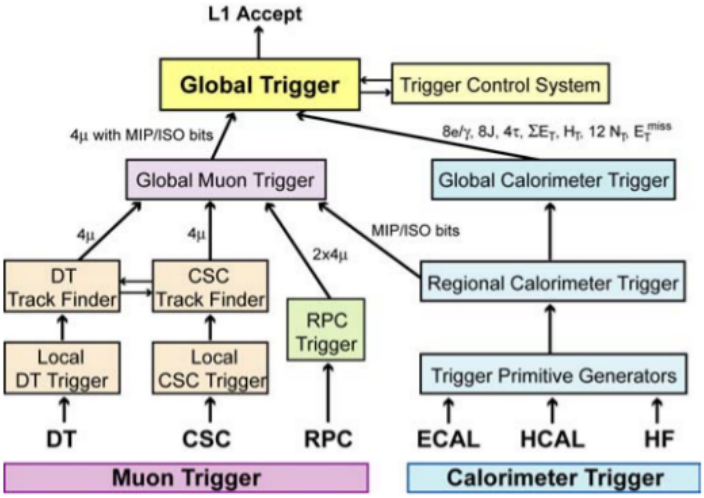

Figure 4.2: Level-1 trigger architecture with the left side in purple describing the muon system and the right blue side describing the calorimeter chain. [28].

send regional hit patterns to their own local trigger. There is some cross-talk between the CSC and DT, after their own local triggering, in which their track-finding algorithms share information to complete tracks and determine physical parameters. Once all this has taken place, all three detector systems send their local trigger information to the global trigger to decide if it is an L1 accept event (in combination with any calorimeter information in the event if so desired in a given trigger path).

Events in the $p+p$ dataset were selected by the `HLT_HIL1DoubleMu0_v1` trigger. This trigger is seeded by an online hardware-based L1 trigger, requiring two muon candidates in the muon detectors with no explicit transverse momentum thresholds, and single muon acceptance in the range $|\eta| < 2.4$. The high-quality condition, (`HighQ`) cut (algorithm bit `0x00e0`) was applied on the L1 muon candidates, requesting that muons are either:

- RPC unconfirmed candidates, or
- DT or CSC unconfirmed candidates, or
- DT/RPC or CSC/RPC matched candidates.

The trigger also required coincidence with the BPTX triggers to ensure that events consisted of real proton-proton collisions. The $p+p$ trigger described above was un-

prescaled (all events were kept) during the whole run. The integrated luminosity for this trigger using the previously mentioned JSON file for $p+p$ is $\mathcal{L}_{\text{int}} = 28.0$ pb^{-1}. The command used to estimate the luminosity in $p+p$ is:

```
brilcalc lumi -u /pb --hltpath HLT_HIL1DoubleMu0_v1 -i
/afs/cern.ch/cms/CAF/CMSCOMM/COMM\_DQM/certification/Collisions15/
5TeV/Cert_262081-262328_5TeV_PromptReco_Collisions15_25ns_JSON_MuonPhys.txt
```

using the brilcalc tool found here:
`https://cms-service-lumi.web.cern.ch/cms-service-lumi/brilwsdoc.html`.

The PbPb data sample consists of three trigger sets:

1. `HLT_HIL1DoubleMu0_v1`, `HLT_HIL1DoubleMu0_part1_v1`, `HLT_HIL1DoubleMu0_part2_v1`, `HLT_HIL1DoubleMu0_part3_v1`
2. `HLT_HIL1DoubleMu0_2HF_v1`, `HLT_HIL1DoubleMu0_2HF0_v1`
3. `HLT_HIL1DoubleMu0_Cent30100_2HF_v1`, `HLT_HIL1DoubleMu0_Cent30100_2HF0_v1`

The first four trigger paths, 1., all have trigger conditions identical to the one used in $p+p$ collisions. The trigger condition was distributed into separate paths due to the limited processing time for a single Physics Dataset (PD). During the run, after assessing the amount of integrated luminosity, trigger rates, and the PD processing time, the decision was made to implement the same trigger condition for four separate triggers and corresponding data paths. The goal was to combine the data in these four paths offline to provide the equivalent of a single `HLT_HIL1DoubleMu0` unprescaled trigger, while simultaneously keeping each path within the limits of the CPU processing time available for a single PD in the HLT farm. In the beginning of the LHC running period, `HLT_HIL1DoubleMu0_v1` was the only live trigger out of the four and was intermittently prescaled depending on the instantaneous luminosity.

In the second trigger set, 2., the conditions are virtually the same as `HLT_HIL1DoubleMu0`, but gated by two different HF coincidence triggers. The HF gates were installed to suppress the rate of cosmic muon contamination for low bunch crossing runs. They were prescaled by factor between 1 – 10 depending on the collision rates.

A combination of triggers (1.) and (2.) were used for the DoubleMu0 data set. The integrated luminosity of this trigger path for the Pb+Pb run is $\mathcal{L}_{\text{int}} = 368\ \mu\text{b}^{-1}$, obtained using similar brilcalc commands as the one mentioned above using the Pb+Pb version of the JSON file and above mentioned Pb+Pb triggers.

The last trigger set, 3., uses the same algorithm as Pb+Pb (2.). However, a tighter coincidence with the HF L1-calorimeter triggers is required. The trigger focuses on the peripheral region, therefore, only the dimuon events with deposited HF energy in the centrality range between 30% and 100% of the minimum-bias Pb+Pb cross section were selected with this trigger condition. This trigger was run unprescaled during the whole run and therefore sampled all the delivered luminosity. It is the data set used for the analysis of any events falling in the relevant centrality bins and is referred to as the Peripheral set or Peripheral data set. The integrated luminosity of this trigger is 464 μb^{-1}.

4.3 Centrality Determination

The centrality of a given heavy-ion collision event can be described as the amount of overlap of the two colliding nuclei. In the case for CMS the collisions that the LHC provides are lead ions, as described in detail previously. Experimentally it would seem hard to determine such a physical quantity on a rather small system size. When two colliding nuclei come in contact, the distance from their centers is known as the impact parameter b. A large impact parameter is referred to a peripheral, having $b \sim 2R$, where R is the radius of a single nuclei. Central collisions have an impact parameter of $b \sim 2R$. In a heavy-ion collision the range of impact parameters goes from 0 to ~ 15 fm. At CMS the sum of the transverse energy, ΣE_T, in the the forward and backward HF calorimeters is used to determine the centrality. This ensures that the determination of the event activity or centrality is in a region that is uncorrelated with the probes we are using in the analysis since we cannot measure muons in the same psuedorapidity as the HF coverage. Determining the centrality starts with a Glauber MC simulation [43] in combination with the ΣE_T. The measurements of ΣE_T are fit using the Glauber MC and the centrality classes for a given amount of measured E_T are thus obtained. Figure 4.3

shows the sum of the the transverse energy distribution in the HF calorimeter for Pb+Pb collisions at $\sqrt{s_{\mathrm{NN}}} = 5.02$ TeV.

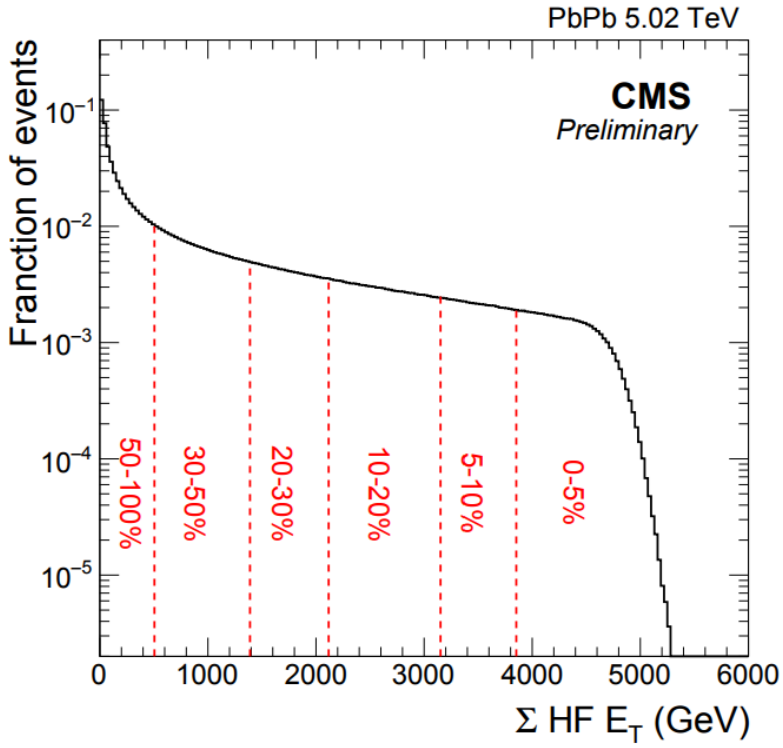

Figure 4.3: Distribution of the ΣE_T in the HF used to determine the centrality classes in 5.02 TeV Pb+Pb collisions. The red lines shows the centrality class boundaries. This was based on similar work as done at 2.76 TeV [44].

The average number of participating nucleons (N_{part}), number of binary collisions (N_{bin}), and the nuclear overlap (T_{AA}) for Pb+Pb collisions at $\sqrt{s_{\mathrm{NN}}} = 5.02$ TeV, is estimated using this Glauber model for each centrality class determined from the ΣE_T. The Glauber model values and centrality variables are summarized in Tables 4.1 and 4.2. A collision that occurs in the $0 - 5\%$ range is considered most central given the collision is almost head on. The centrality class of $70 - 100\%$ is considered very peripheral, which means the colliding nuclei have minimal overlap.

Table 4.1: Glauber model parameters for Pb+Pb collisions at $\sqrt{s_{\mathrm{NN}}} = 5.02$ TeV.

Parameter	Value
Nuclear radius	6.62 ± 0.06 fm
Skin depth	0.546 ± 0.010 fm
d_{min}	0.4 ± 0.4 fm
$\sigma_{\mathrm{NN}}^{\mathrm{inel}}$	70 ± 5 mb

Table 4.2: Centrality classes, number of participating nucleons (N_{part}), number of binary collisions (N_{bin}), and the nuclear overlap (T_{AA}) for Pb+Pb collisions at $\sqrt{s_{\mathrm{NN}}} = 5.02$ TeV, obtained using the Glauber model parameters of Table 4.1.

Centrality class	N_{part}	N_{bin}	T_{AA} (mb^{-1})
0–5%	384.3 ± 1.2	1819 ± 126	25.98 ± 0.43
5–10%	333.4 ± 2.6	1432 ± 99	20.46 ± 0.35
10–20%	264.3 ± 3.4	1005 ± 68	14.35 ± 0.29
20–30%	189.2 ± 3.7	606 ± 40	8.66 ± 0.24
30–40%	131.4 ± 3.6	349 ± 24	4.98 ± 0.20
40–50%	86.9 ± 3.4	186 ± 15	2.66 ± 0.16
50–60%	53.9 ± 3.6	90.7 ± 7.3	1.29 ± 0.10
60–70%	30.6 ± 2.0	40.1 ± 4.2	0.57 ± 0.06
70–100%	8.3 ± 1.2	7.7 ± 1.1	0.11 ± 0.02
0–10%	358.8 ± 1.9	1626 ± 112	23.22 ± 0.39
10–30%	226.7 ± 3.7	805 ± 54	11.51 ± 0.27
30–50%	109.2 ± 3.6	267 ± 20	3.82 ± 0.19
50–100%	21.9 ± 2.2	30.8 ± 3.2	0.44 ± 0.06

4.4 Simulation

The acceptance and efficiency is used to estimate the fraction of muons or dimuons that fail to be reconstructed because they do not hit the detector geometry or because the reconstruction algorithm do not find them. MC simulations of Υ(1S), Υ(2S), and Υ(3S) both for $p+p$ and Pb+Pb are used to estimate these quantities. MC samples are officially produced through the CMS framework using PYTHIA 8 [45] generated Υ for $p+p$ and PYTHIA 8 generated Υ embedded into HYDJET 1.9 [46] events in the case of Pb+Pb to simulate the increase in track multiplicity of the Pb+Pb events. Embedding greatly increases the file size and CPU time. Therefore the MC generates (or distributes) events into relatively wide dimuons p_T bins to have sufficient statistics at all p_T. The MC is produced in the general CMS production and is run through GEN-SIM-RECO chain which includes a GEANT4 description of the CMS detector.

The Pb+Pb samples were generated in the following dimuon p_T bins:

- Υ(1S): $[0-3], [3-6], [6-9], [9-12], [12-15], [15-30]$ GeV/c
- Υ(2S): $[0-3], [3-6], [6-9], [9-12], [12-15], [15-30]$ GeV/c
- Υ(3S): $[0-3], [3-6], [6-9], [9-30]$ GeV/c

Consequently, each Pb+Pb sample has to be normalized to have a continuous, smooth, and realistic p_T spectrum. Normalization factors (weights) are chosen to match the p_T distributions of the $p+p$ MC sample which is produced for the entire continuous p_T range. Possible kinematical differences between $p+p$ and Pb+Pb and data vs. MC are taken into account at a later stage. Equation (4.1) shows how this weight-normalization factor was determined for each p_T bin.

$$\text{weight}(p_T\text{-bin}) = \frac{\text{Number of generated pp events } (p_T\text{-bin})}{\text{Number of generated PbPb events } (p_T\text{-bin})} \tag{4.1}$$

Figure 4.4 shows the Pb+Pb MC p_T distributions after normalization factors are applied. For example, the left panel shows the case for the Υ(1S), where the 6 different p_T ranges for the MC simulation are displayed in different colors. The spectrum of the

$p+p$ MC sample (black line) obtained from PYTHIA is also overlaid for comparison. Table 4.3 contains the calculated weights associated with each sample and p_T bin. These weights are then applied to the MC before studies of efficiency or acceptance are carried out.

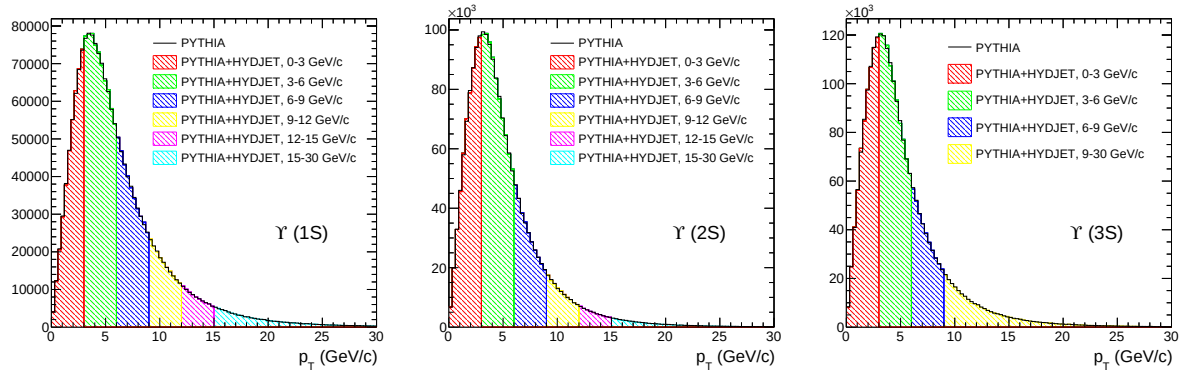

Figure 4.4: p_T spectra for $p+p$ (black line) and Pb+Pb (colors) MC samples after the normalization for Υ(1S) (left), Υ(2S) (middle), Υ(3S) (right).

4.5 Offline Selection

4.5.1 Muon and Dimuon Selections

The dimuon and muon selection and quality cuts for this analysis are a modified version ("Hybrid") of the CMS MuonPOG "Soft Muon" cuts with the addition of the "`isGlobal`" and removal of "`highPurity`" tracking condition, as explained below. The details of this study are described in Ref. [47], Section 2.1 "Low pT muon (onia analyses)". The "Hybrid Soft ID" single muon cuts are as follows:

- `isTrackerMuon and isGlobal` – This selects muon tracks that have at least a matched track in the muon station that in addition also matches a track in the silicon tracker, and where the combined information of the tracker and muon stations is used in a global track fit of reasonable quality.

- `isGoodMuon(TMOneStationTight)` – This selects a muon with at least one well matched track in the muon stations.

Table 4.3: p_T weights for various bins of Pb+Pb MC.

Sample	p_T (GeV/c)	weight
Υ(1S)	$0-3$	3.10497
	$3-6$	4.11498
	$6-9$	2.2579
	$9-12$	1.2591
	$12-15$	0.567094
	$15-30$	0.783399
Υ(2S)	$0-3$	5.89168
	$3-6$	9.08207
	$6-9$	3.106
	$9-12$	1.10018
	$12-15$	0.534916
	$15-30$	0.776183
Υ(3S)	$0-3$	6.86815
	$3-6$	8.29618
	$6-9$	6.75153
	$9-30$	5.48684

- `nPixWMea` > 0 − This selects muon tracks that must have at least one silicon pixel hit. This cut guarantees a good p_T measurement and suppresses in-flight decay muons.

- `nTrkWMea` > 5 − The muon track must have at least six silicon tracker hits. Further suppression of muons from decays in-flight.

- $|\mathtt{d_{xy}}| < 0.3$ − The distance of the muon track from the closest primary vertex must be less than 3 mm in the transverse direction.

- $|\mathtt{d_z}| < 20$ − The distance of the muon track from the closest primary vertex must be less than 20 cm in the longitudinal direction.

Additionally we select single muons in the following kinematic range

$$p_T(\mu) > 4 \text{ GeV}/c, |\eta(\mu)| < 2.4, \tag{4.2}$$

which allows Υ mesons to be measured down to $p_T = 0$. The dimuon kinematic range studied for this analysis is in the region

$$p_T(\mu\mu) < 30 \text{ GeV}/c, |y| < 2.4. \tag{4.3}$$

When forming a muon pair, the two muons must form a vertex with a probability larger than 1%.

4.5.2 Data Binning

In this analysis, multiple triggers were used, as described in Section 4.2. In studying these PD's it was decided to use the DoubleMu0 data set for the centrality-integrated values, p_T dependence, $|y|$ dependence, and the centrality 0-30% data. While we used the Peripheral data set for studying events of centrality 30-100% due to the increase of the peripheral statistics.

The bins for analyzing these data were chosen to be as follows, along with their corresponding data set.

p + p and Pb+Pb DoubleMu0

Υ(2S) Analysis

- Integrated MinBias (MB): Centrality [0–100]%;
- p_T [GeV/c]: $\in$ [0–5.0], [5.0–12.0], [12.0–30.0];
- $|y^{\mu\mu}|$: $\in$ [0–1.2], [1.2–2.4];
- Centrality [%]: $\in$ [0–5], [5–10], [10–20], [20–30].

Υ(3S) Analysis

- Integrated MinBias (MB): Centrality [0–100]%;
- Centrality [%]: $\in$ [0–10], [10–30].

Pb+Pb Peripheral

Υ(2S) Analysis

- Centrality [%]: $\in$ [30–40], [40–50], [50–60], [60–70], [70–100].

Υ(3S) Analysis

- Centrality [%]: $\in$ [30–50], [50–100].

When analyzing data that is either MinBias or as a function of centrality, Equations (4.2) and (4.3) hold. When analyzing p_T or $|y|$, Equations (4.2) are applied and Equation (4.3) is allowed to change corresponding to the bin in question. For instance, $|y|$ is held constant at $|y| < 2.4$ when studying the various dimuon p_T bins and vice-versa.

Chapter 5

Analysis

This chapter discusses the analysis of the Υ data collected in 2015 at the CERN LHC using the CMS detector. Specifically, this chapter will detail the fitting of the $\Upsilon(n\mathrm{S})$ mass spectrum, the efficiency and the corresponding systematics. As mentioned previously, the signal in question is that of an Υ decaying to two oppositely-charged muons. Figure 5.1 shows an event of an $\Upsilon(1\mathrm{S}) \to \mu^+\mu^-$ candidate detected in a Pb+Pb collision by CMS in 2015. In order to study the Υ, we form a dimuon out of the two muons seen in the image, and the invariant mass of the dimuon is consistent with the $\Upsilon(1\mathrm{S})$ mass. Given the momentum of the individual muons and their corresponding geometrical locations we can determine the invariant mass of the Υ candidates and their corresponding kinematic quantities. This dimuon invariant mass spectrum becomes the basis for the analysis presented in this thesis.

5.1 Fitting

This section details the methods used to extract the Υ signals, and for estimating the excited-to-ground state ratios in the $p+p$ and Pb+Pb data sets. It starts with a discussion about the mathematical constructs and leads into the study of MC and data to determine the signal and background models.

The invariant mass range for fitting was originally set to previously analyzed Υ production at $\sqrt{s_{NN}} = 2.76$ TeV in Ref. [48]. Specifically, the dimuon invariant mass range 7.5–14 GeV/c^2 was preferred for most kinematic and centrality bins, except for the lowest

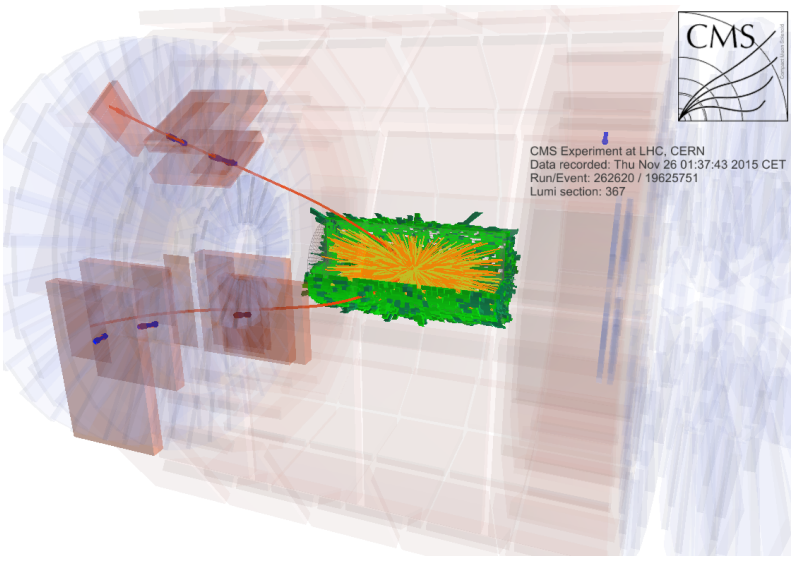

Figure 5.1: Event display for a dimuon event with an Υ(1S) candidate in a Pb+Pb collision at 5.02 TeV.

p_T bin, 0 – 5 GeV/c. This lowest p_T bin had the mass range restricted to 8–14 GeV/c^2. This was due to the fact that the $p_T > 4$ GeV/c selection on the single muons kinematically restricts the range of the dimuon. Those dimuons with low transverse momentum will show a kinematic peak at a mass range close to twice the value of the single muon cut. As one select muons with larger p_T, the kinematic peak moves to lower masses. For our choice of kinematic bins, the effect plays a role in the 0–5 GeV/c bin. The approach taken in the CMS B-Physics (BPH) group, e.g. Ref. [49] was to start the fit at higher masses, for example 8 or even 8.5 GeV/c^2.

In this analysis, we have studied several cases. In one case, keeping the low invariant mass limit for the fit range for the lowest p_T bin. In a second case, where we raised the limit keeping the fit function the same, and a final case where we added an additional error function to help describe the background shape. The rationale for the latter case is that the shape of the background at low invariant mass is coming from a convolution of error functions, where each of those error functions would be obtained in the limit of a narrow kinematic bin in both p_T and rapidity. Therefore, including two error functions in the fit is one simplified way of taking into account this effect. Both the fit with an increased lower mass limit and the fit with the two error functions give results with a

reasonable χ^2.

For simplicity, we settle on the following range for the invariant mass spectrum for all analysis bins,

$$8 \leq m_{\mu\mu} \ < 14\text{GeV}/c^2. \tag{5.1}$$

Single ratios ($\mathcal{R}_{\text{n1}}$, where $n = 1 - 3$ for the various Υ states) are extracted from extended unbinned maximum-likelihood fits by simultaneously fitting the ratio of the yields of the excited, $\Upsilon(2S)$ and $\Upsilon(3S)$, states to the $\Upsilon(1S)$ ground state. A fit is performed to the opposite sign dimuon invariant mass spectrum. These single ratios are studied in both Pb+Pb and $p+p$ data to form the previously-mentioned double ratios.

It has been previously determined that the use of a Crystal-Ball (CB) function can best represent the shape of the signal in the Υ peaks [50]. This consists of a Gaussian that is then connected analytically (i.e. such that the function itself and its first derivative are both continuous) to a low-mass power-law tail, as first implemented in Ref. [50]. It is given by:

$$\text{CB}(x;\bar{x},n,\alpha,\sigma) = N \begin{cases} \exp(-\frac{(x-\bar{x})^2}{2\sigma^2}) & \text{for } \frac{x-\bar{x}}{\sigma} > -\alpha \\ A(B-\frac{x-\bar{x}}{\sigma})^{-n} & \text{for } \frac{x-\bar{x}}{\sigma} \leq -\alpha\,, \end{cases} \tag{5.2}$$

where

$$\begin{aligned} A &= \left(\frac{n}{|\alpha|}\right)^n \exp\left(-\frac{|\alpha|^2}{2}\right)\,, \\ B &= \frac{n}{|\alpha|} - |\alpha|\ . \end{aligned}$$

A signal probability density function (PDF) consisting of the sum of two Crystal Ball functions was preferred over a single Crystal Ball, based on goodness-of-fit tests performed on Monte Carlo simulations of the Υ dimuon decays as well as from previous analyses [48]. We also considered as a signal PDF a Crystal Ball plus a Gaussian. The need for two Crystal Ball functions is justified physically because of the varying mass resolution with increasing dimuon rapidity. This arises from the varying momentum resolution of the single-muon reconstruction in the forward and backward regions (endcaps) of the CMS muon system, which has degraded resolution compared to the midrapidity barrel region.

The double Crystal Ball fit and the Crystal Ball in summation with a Gaussian fit proved to be the most effective signal models when fitting the Υ peak. This was determined from a study on MC generated Υ(1S) events which were embedded in both Pb+Pb and $p+p$ underlying events and discussed in Section 5.1.1.

The resulting signal PDF used for the $\Upsilon(1S)$ resonance is as follows:

$$\Sigma_{1S}\left(m_{\mu\mu}; m_0, n, \alpha, \sigma_0, f, x\right) = f\mathrm{CB}_1\left(m_{\mu\mu}; m_0, n, \alpha, \sigma_0\right) + (1-f)\,\mathrm{CB}_2\left(m_{\mu\mu}; m_0, n, \alpha, x\cdot\sigma_0\right) \ . \quad (5.3)$$

Where the six parameters for Σ_{1S} are m_0 (mean or mass), σ_0 (standard deviation), n (power law exponent), α (location of transition from Gaussian to power law), f (relative combination of two Crystal Ball functions), and x (σ_2/σ_0). In order to reduce the number of free independent parameters in the fit, we employ the same values of m_0, n, and α for both Crystal Ball functions. The additional free parameter, x, for the second Crystal Ball (CB_2) represents the ratio of the two σ parameters, and is used to account for the varying mass resolution in the various regions of the detector. In other words, this function models the reconstruction of the Υ peaks as a simple combination of two identical Crystal Ball functions except with different mass resolutions.

5.1.1 MC Signal Study

The Υ(1S) $p+p$ and Pb+Pb MC data samples were used to determine the best signal model. Additionally, once the best signal model is chosen its parameters were extracted to use in the fit model for data. Nominally, as described previously the Crystal Ball function is used often for fitting the opposite sign dimuon spectrum of signal peaks such as the $\Upsilon(n\mathrm{S})$ family. As mentioned in the previous section, the two signal models studied were the summation of two Crystal Ball functions and the summation of a Crystal Ball and Gaussian functions. Table 5.5 shows the the chi^2/dof as a goodness-of-fit measure between the two Crystal Ball (2CB) and Crystal Ball in summation with a Gaussian(CB + Gauss) for the various kinematic and integrated bins. From these results, it was determined to use the two Crystal Ball PDF, as in Equation 5.3 for this analysis. Figure 5.2 shows the two example fits for the pp MC in the forward rapidity bin where the left plot (2CB)

is clearly a better fit than the right plot (CB + Gaus). The Crystal Ball plus Gaussian was discarded as a nominal fit function. However, this function was used to estimate systematic uncertainties on the yield and single ratio extraction procedure.

χ^2/dof	pp		PbPb	
	2CB	CB + Gauss	2CB	CB + Gauss
$p_T < 5.0$	1.46	1.79	2.72	3.16
$5.0 < p_T < 12.0$	1.47	1.69	2.71	2.70
$12.0 < p_T < 30.0$	0.915	1.05	1.9	2.12
$\|y\| < 1.2$	1.47	1.84	3.28	3.49
$1.2 < \|y\| < 2.4$	0.925	2.05	2.81	3.69
Integrated	2.11	2.77	2.83	2.97

Table 5.1: Goodness of fit for two Crystal Balls or Crystal Ball plus a Gaussian for $p+p$ and Pb+Pb.

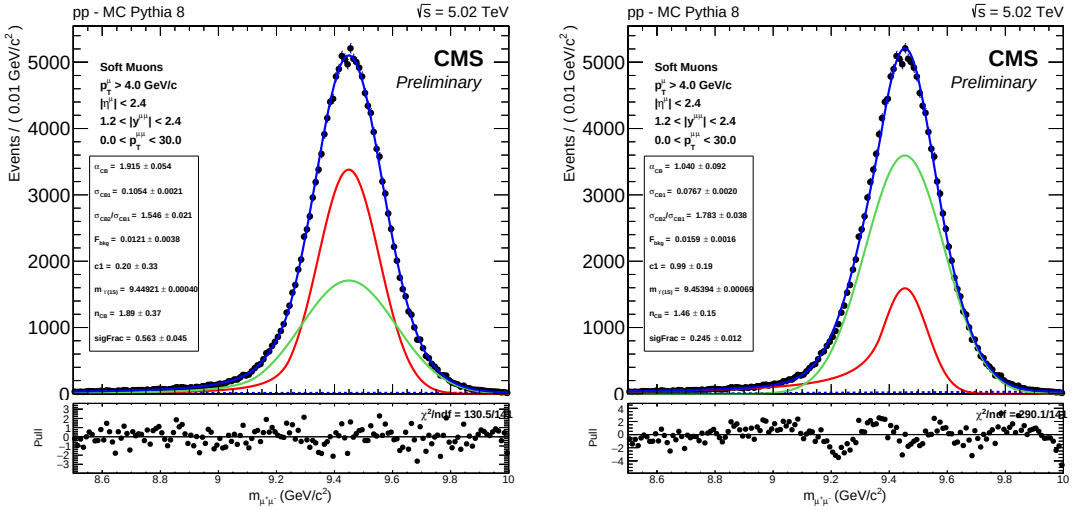

Figure 5.2: Υ(1S) invariant mass spectrum fit to pp MC using two Crystal Balls where the blue line is the total fit and the red and green are individual Crystal Balls (left) and using Crystal Ball plus Gaussian where the blue is the total fit and the red is the Crystal Ball while the green is the Gaussian (right) for $|y^{\mu\mu}| \in$ [1.2-2.4]

Once the sum of two Crystal Ball functions was chosen as the nominal signal model, we can explore the signal parameters and fits to $p+p$ and Pb+Pb MC data sets in the

bins of this analysis. Figures 5.3– 5.8 show the results of the two Crystal Ball fits in the integrated, p_T, and $|y|$ bins, respectively. The solid blue line is the total fit result while the green and red lines represent the two Crystal Balls that make up the signal. The blue dashed line is a first order Chebychev polynomial to account for any background, although it is very minimal in MC simulations. All the parameters both signal and background are free in these MC fits in order to produce reasonable fits for the extraction of signal parameters.

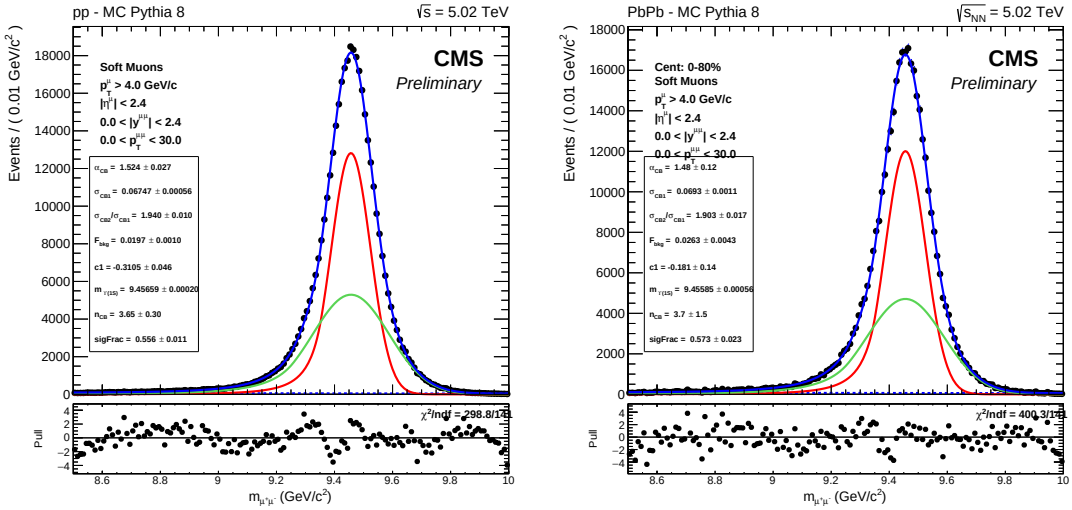

Figure 5.3: Integrated MC fit to $p+p$ (left) and Pb+Pb (right) simulations of the Υ(1S) invariant mass spectrum using a double Crystal Ball function where the blue line is the total fit and the red and green are individual Crystal Balls.

Tables 5.2 and 5.3 show the Υ(1S) signal parameters for $p+p$ and Pb+Pb obtained from MC fits to the invariant mass spectra. These signal parameters are as described in Section 5.1.

5.1.2 Excited State Signal

For the PDFs of the Υ(2S) and Υ(3S) excited states, the parameters n, α, f and x are constrained to be identical to those of the Υ(1S) PDF, Eq. (5.3). In order to account for the mass-dependent detector resolution, we assumed that both the width, $\sigma_{n\mathrm{S}}$, and the

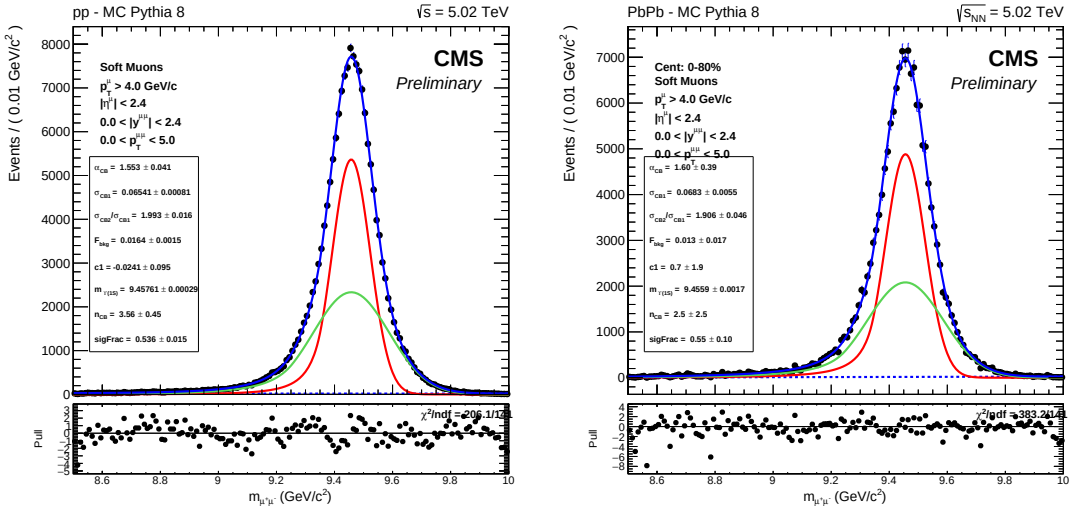

Figure 5.4: Fit to MC $p+p$ (left) and Pb+Pb (right) simulations for the range p_T [GeV/c] $\in$ [0-5.0] of the Υ(1S) invariant mass spectrum using a double Crystal Ball function. Where the blue line is the total fit and the red and green lines are individual Crystal Balls.

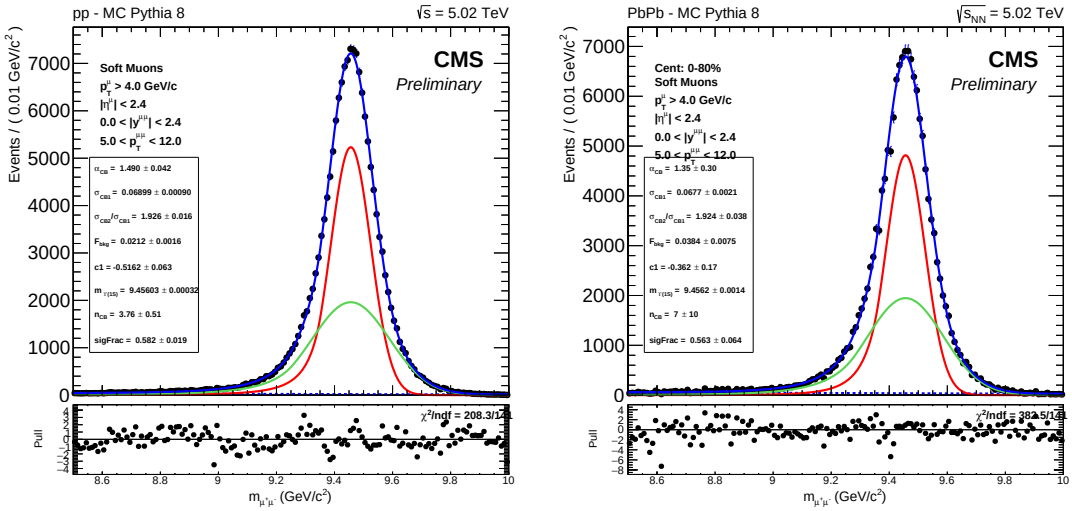

Figure 5.5: Fit to MC $p+p$ (left) and Pb+Pb (right) for the range p_T [GeV/c] $\in$ [5.0-12.0] of the Υ(1S) invariant mass spectrum using a double Crystal Ball function. Where the blue line is the total fit and the red and green lines are individual Crystal Balls.

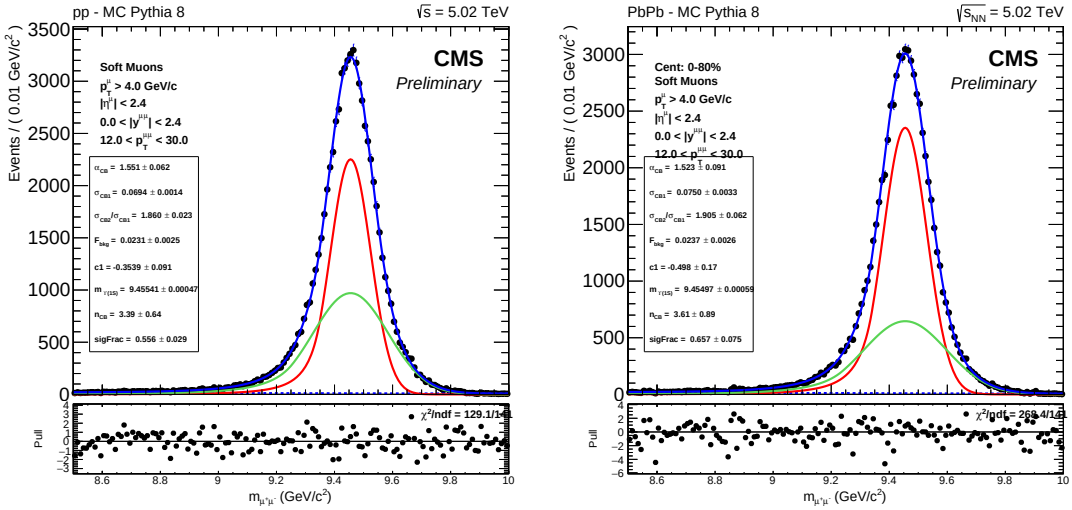

Figure 5.6: Fit to MC $p+p$ (left) and Pb+Pb (right) simulations for the range p_T [GeV/c] $\in$ [12.0-30.0] of the Υ(1S) invariant mass spectrum using a double Crystal Ball function. Where the blue line is the total fit and the red and green lines are individual Crystal Balls.

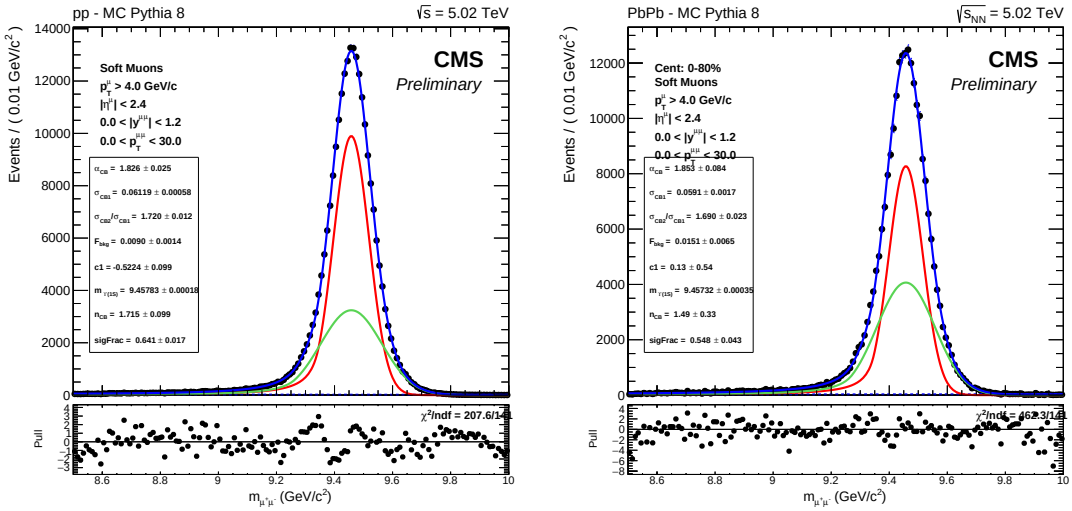

Figure 5.7: Fit to MC $p+p$ (left) and Pb+Pb (right) simulations for the range $|y^{\mu\mu}| \in$ [0-1.2] of the Υ(1S) invariant mass spectrum using a double Crystal Ball function. Where the blue line is the total fit and the red and green lines are individual Crystal Balls.

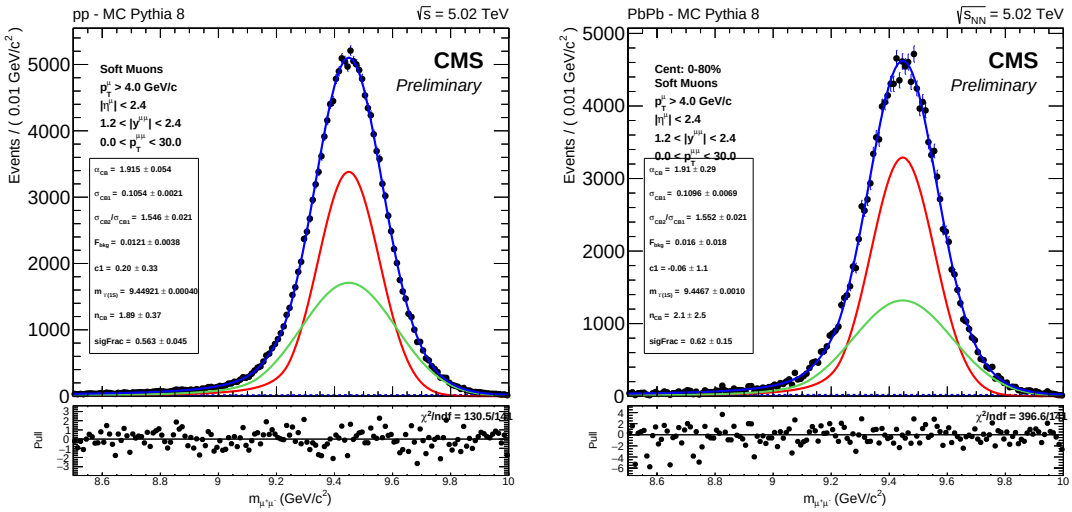

Figure 5.8: Fit to MC $p+p$ (left) and Pb+Pb (right) simulations for $|y^{\mu\mu}| \in [1.2\text{-}2.4]$ of the Υ(1S) invariant mass spectrum using a double Crystal Ball function. Where the blue line is the total fit and the red and green lines are individual Crystal Balls.

pp MC	Signal Parameters				
	σ_0	α	n	$x = \frac{\sigma_2}{\sigma_0}$	f
$p_T < 5.0$	0.0654	1.55	3.56	1.99	0.536
$5.0 < p_T < 12.0$	0.0690	1.49	3.76	1.93	0.582
$12.0 < p_T < 30.0$	0.0694	1.55	3.39	1.85	0.556
$\|y\| < 1.2$	0.0612	1.82	1.72	1.72	0.641
$1.2 < \|y\| < 2.4$	0.105	1.91	1.89	1.55	0.563
Integrated	0.0675	1.52	3.65	1.94	0.556

Table 5.2: MC fit parameters for sum of two Crystal ball signal PDFs in $p+p$.

PbPb MC	Signal Parameters				
	σ_0	α	n	$x = \frac{\sigma_2}{\sigma_0}$	f
$p_T < 5.0$	0.0683	1.60	2.48	1.91	0.573
$5.0 < p_T < 12.0$	0.0677	1.35	6.67	1.92	0.563
$12.0 < p_T < 30.0$	0.0750	1.52	3.61	1.905	0.657
$\|y\| < 1.2$	0.0591	1.85	1.49	1.69	0.548
$1.2 < \|y\| < 2.4$	0.110	1.905	2.11	1.55	0.618
Integrated	0.0693	1.48	3.74	1.90	0.573

Table 5.3: MC fit parameters for sum of two Crystal ball signal PDFs in Pb+Pb.

mass, $m_{n\mathrm{S}}$, scale as

$$\begin{aligned} m_{nS} &= m_0 \frac{m^{n\mathrm{S}}_{\mathrm{PDG}}}{m^{1\mathrm{S}}_{\mathrm{PDG}}} \\ \sigma_{n\mathrm{S}} &= \sigma_0 \frac{m^{n\mathrm{S}}_{\mathrm{PDG}}}{m^{1\mathrm{S}}_{\mathrm{PDG}}} \ . \end{aligned}$$

With this prescription, the Υ(nS) PDF reads

$$\Sigma_{n\mathrm{S}}\left(m_{\mu\mu}; m_0, n, \alpha, \sigma_0, f, x\right) = \Sigma_{1\mathrm{S}}\left(m_{\mu\mu}; m_0 \frac{m^{n\mathrm{S}}_{\mathrm{PDG}}}{m^{1\mathrm{S}}_{\mathrm{PDG}}}, n, \alpha, \sigma_0 \frac{m^{n\mathrm{S}}_{\mathrm{PDG}}}{m^{1\mathbf{S}}_{\mathrm{PDG}}}, f, x\right) \ .$$

With this assumption, all the parameters that define the shape of the Υ ground state and the excited states can be obtained using the MC simulations of the ground state alone. The 5 shape parameters n, α, f, σ_0, and x are thus determined from Monte Carlo simulations and the fit to the data is performed with these parameters fixed from the values in Tables 5.2 and 5.3. The parameter m_0 for the ground state mass is kept free in the fit to the data, as well as the parameter to estimate the yield. The excited states only have a yield (or in our case, a ratio) parameter left free in the fit, with all the other parameters constrained as discussed above. The signal $\mathcal{S}$ is defined as a weighted sum of

the Υ(1S), Υ(2S), and Υ(3S) PDF [1],

$$\mathcal{S}(m_{\mu\mu};\mathcal{N}_{1S},\mathcal{R}_{21},\mathcal{R}_{31},m_0\big|\ n,\alpha,\sigma_0,f,x) = \mathcal{N}_{1S}[\Sigma_{1S}(m_{\mu\mu}) + \mathcal{R}_{21}\Sigma_{2S}(m_{\mu\mu}) + \mathcal{R}_{31}\Sigma_{3S}(m_{\mu\mu})] \quad (5.4)$$

We introduce the notation

$$\mathcal{R}_{21} \equiv \left(\frac{\mathcal{N}_{2S}}{\mathcal{N}_{1S}}\right), \quad (5.5)$$

$$\mathcal{R}_{31} \equiv \left(\frac{\mathcal{N}_{3S}}{\mathcal{N}_{1S}}\right). \quad (5.6)$$

where $\mathcal{N}_{1S}$, $\mathcal{N}_{2S}$, and $\mathcal{N}_{3S}$ are the raw yields of the Υ(1S), Υ(2S), and Υ(3S), respectively. $\mathcal{N}_{1S}$, $\mathcal{R}_{21}$, $\mathcal{R}_{31}$, and m_0 are left as free parameters in the fit to the data. The fixed signal parameters are released when estimating systematic uncertainties to the signal extraction. This is discussed in Sec. 5.3.

The three signal peaks in the data lie atop a continuum of dimuons identified as background showing a smooth kinematic turn-on shape that, combined with the falling spectrum at higher masses, produces a shoulder/peak structure below the Υ mass, where the position of the kinematic peak is due in part to the choice of single muon p_T cuts. The location of the peak will be different depending on the dimuon kinematic bin under study. For example, for the bins that include dimuons down to $p_T = 0$, the peak will be visible near a mass equal to roughly twice the single muon p_T cut of 4 GeV, i.e. $m \approx 8$ GeV. For the bins at higher p_T, the kinematic peak will show up at lower mass values and can lie outside the fit range. These are all things that we need to consider when discussing the background to the data.

5.1.3 Background Model

This section details the study of the background model. The background shape was studied for various possible alternative functions of the opposite-sign dimuon spectrum. From previous analyses [8, 48], a background containing an error function (Erf) multiplied by an exponential (Exp) was determined to be the optimal description of the underlying

[1] In the following, we shall use for brevity the shorthand notation $\mathcal{S}(m_{\mu\mu};\mathcal{N}_{1S},\mathcal{R}_{21},\mathcal{R}_{31},m_0) \equiv \mathcal{S}(m_{\mu\mu};\mathcal{N}_{1S},\mathcal{R}_{21},\mathcal{R}_{31},m_0 \mid n,\alpha,\sigma_0,f,x)$.

N	NLL	p(H0: N = 1)	p(H0: N = 2)	p(H0: N = 3)
1	-977001.14			
2	-977001.14	**100.0**%		
3	-977000.90	**100.0**%	100.0%	
4	-977000.64	100.0%	100.0%	100.0%
5	-977001.63	99.8%	98.6%	83.3%

Table 5.4: Negative log-likelihoods for fits with Erf*Exp + Polynomial (or Constant). Where N describes the type of function from lowest number of parameters to largest and this is studied in centrality bin 0-100%. In addition the p-values of the LLR-test for the null-hypothesis are listed. Tests of which the null-hypothesis cannot be rejected for two consecutive orders are highlighted in bold, together with the corresponding order.

dimuon background distribution. With this as the starting point, a family of functions were studied in order to determine the best model. Table 5.4 Shows an example of the results to a Log-likelihood ratio (LLR) study for the integrated [0–100]% central Pb+Pb fits. The value N refers to the numbers of the parameters needed to describe the background shape, where 1 is the lowest number of parameters and 5 is the highest number of parameters considered. This study was performed over all analysis bins for Pb+Pb and *pp* data and it was concluded that the best fit function for the background is the error function times an exponential for all bins except the last two p_T bins [5-12] and [12-30] GeV/c were best fit by a simple exponential without the error function.

The values of N refer to the following fit functions studied:

- 1 = ErrFunction*Exp;
- 2 = ErrFunction*Exp + constant;
- 3 = ErrFunction*Exp + 1st order Poly;
- 4 = ErrFunction*Exp + 2nd order Poly;
- 5 = ErrFunction*Exp + 3rd order Poly;

An error function multiplied by an exponential is used for the PDF of the background shape. The error function is motivated by the shape of the kinematic peak produced by the single-muon-p_T cuts. The exponential component is motivated by the dominance of the combinatorial background, which should fall with energy according to a statistical phase space factor, i.e. an exponential. There are additional physics contributions to the background, the dominant ones being the Drell-Yan muon pairs, and also muon pairs from the weak decay of bare-bottom-hadron pairs, e.g. $b\bar{b} \rightarrow B^+B^- \rightarrow \mu^+\mu^- + X$ and also open-charm-hadron pairs, but at a much lower rate. (We take into account alternative PDFs for the background as systematic uncertainties in Sec. 5.3.) The nominal Background PDF, $\mathcal{B}$, used in the analysis is constructed as

$$\mathcal{B}\left(m_{\mu\mu};\mu,\sigma,\lambda\right) = \exp\left(-\frac{m_{\mu\mu}}{\lambda}\right)\frac{1+\mathrm{Erf}\left(\frac{m_{\mu\mu}-\mu}{\sqrt{2}\sigma}\right)}{2}\ . \tag{5.7}$$

The background shape depends on three parameters left free during fitting and are as follows:

- μ, the parameter that controls the location of the kinematic "turn-on". This parameter is the location at which the argument of the Erf is equal to 0, and the Erf value is also 0. If one derives the Erf as the integral of a Gaussian, this parameter would mark the location of the mean of the Gaussian.

- σ, the width parameter, equal to the σ parameter of the Gaussian distribution from which the error function can be derived. In our case, this parameter is sensitive to the mass resolution as well as the convolution of the kinematic single muon p_T cut and the underlying dimuon p_T distribution,

- λ, the decay constant of the exponential function.

In order to fit the data we need to know something about the initial background parameter values to help our fits converge accurately and in a timely manner. The same-sign dimuon mass spectrum can be used as a first-order approximation to the background shape. It should have the similarly-described turn on and kinematic peak. Figures 5.9 to

5.14 show the fit to same-sign dimuon spectrum. Table 5.5 shows the extracted parameters for the background from these like sign fits to $p + p$ and Pb+Pb data. These parameters are used as initial seed parameters for fitting the opposite-sign data.

Like Sign Fits	pp			PbPb		
	μ	σ	λ	μ	σ	λ
$p_T < 5.0$ (GeV/c)	8.98	0.970	6.29	8.50	0.798	4.49
$5.0 < p_T < 12.0$ (GeV/c)	-	-	21.3	-	-	8.52
$12.0 < p_T < 30.0$ (GeV/c)	-	-	12.7	-	-	18.9
$\|y\| < 1.2$	8.54	1.48	11.2	7.82	1.05	8.23
$1.2 < \|y\| < 2.4$	8.64	1.10	4.50	8.18	1.20	2.97
Integrated	8.52	1.28	7.95	7.86	1.02	6.08

Table 5.5: Background fit parameters from like-sign fits for $p+p$ and Pb+Pb data.

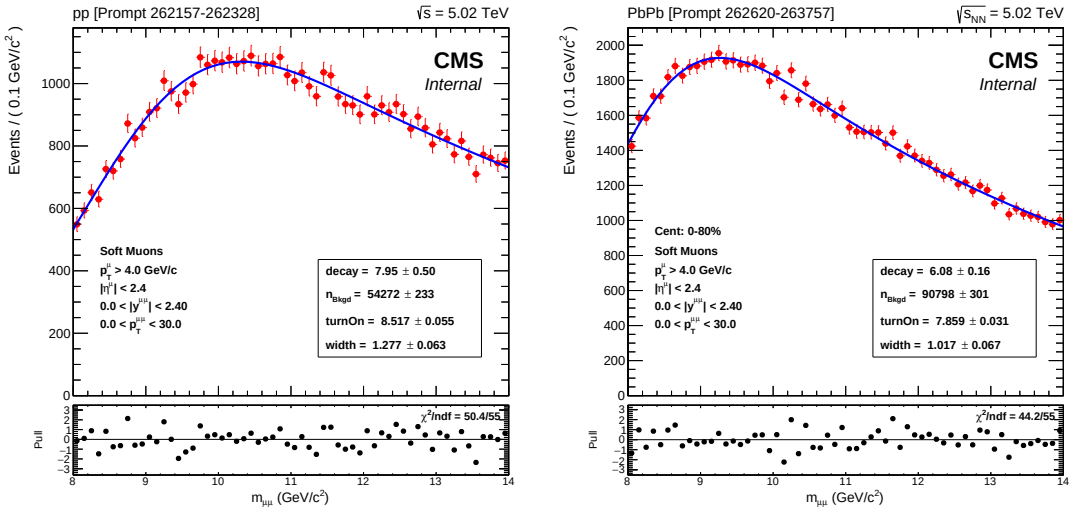

Figure 5.9: Integrated like-sign dimuon fit to $p+p$ (left) and Pb+Pb data (right)

From the studies using the LLR test and fits to like-sign data, we find that the background shape $\mathcal{B}$ from Eq. 5.7 does a reasonable job of fitting the background for most analysis bins. In the two high-p_T bins, the dimuon p_T is sufficiently high that the kinematic peak resulting from the single muon p_T cuts shows up at masses below our fitting range. Therefore, a fit with a simple exponential is preferred, as seen in Figs. 5.11 and 5.12.

Once the background and signal models are combined, the background parameters can be studied. The centrality, y, and p_T dependence of the μ parameter are shown

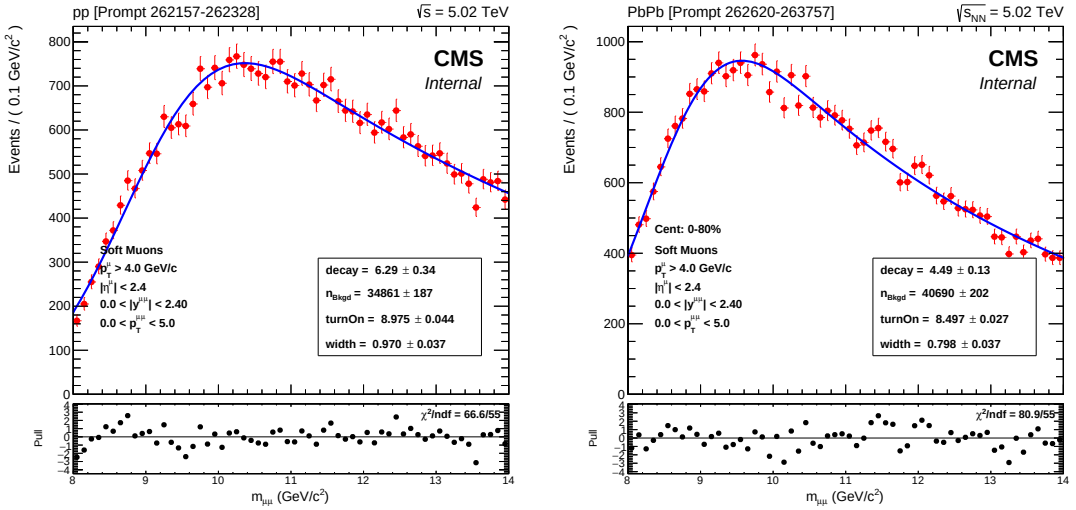

Figure 5.10: Like-sign dimuon fit to $p+p$ (left) and Pb+Pb data (right) for p_T [GeV/c] $\in$ [0-5.0].

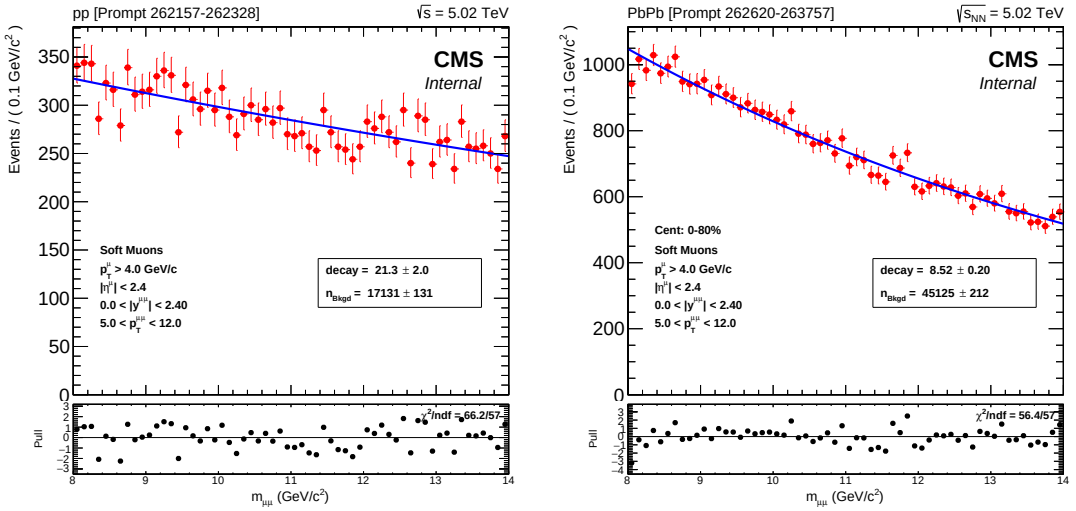

Figure 5.11: Like-sign dimuon fit to $p+p$ (left) and Pb+Pb data (right) for p_T [GeV/c] $\in$ [5.0-12.0].

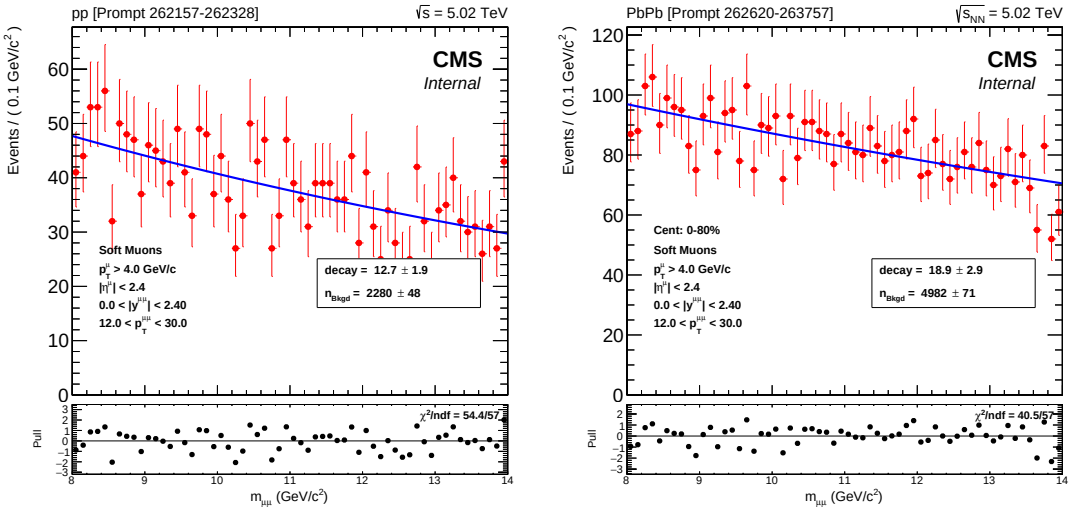

Figure 5.12: Like-sign dimuon fit to $p+p$ (left) and Pb+Pb data (right) for p_T [GeV/c] $\in$ [12.0-30.0].

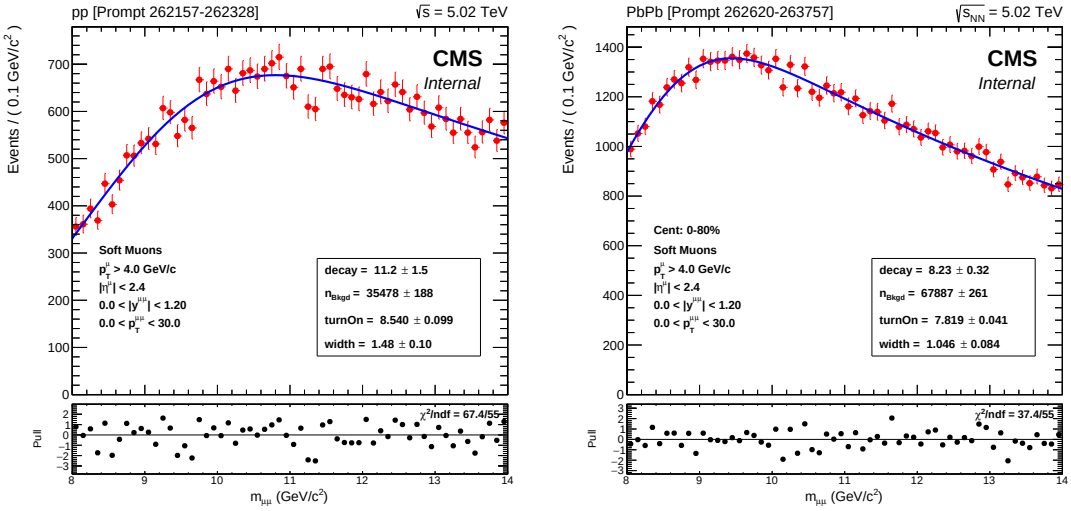

Figure 5.13: Like-sign dimuon fit to $p+p$ (left) and Pb+Pb data (right) for $|y^{\mu\mu}| \in$ [0-1.2]

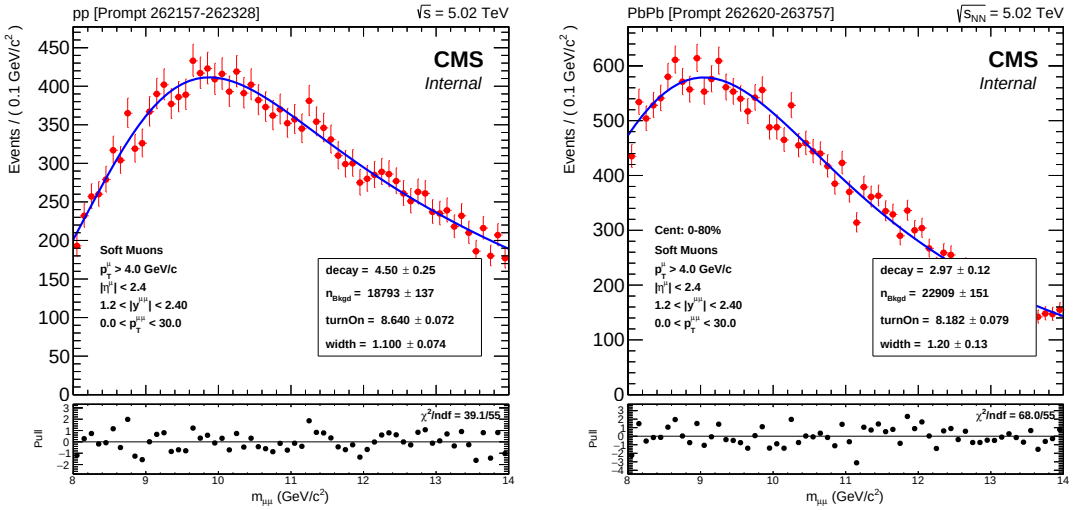

Figure 5.14: Like-sign dimuon fit to $p+p$ (left) and Pb+Pb data (right) for $|y^{\mu\mu}| \in$ [1.2-2.4]

in Fig. 5.15. These were extracted from fits to opposite-sign dimuon data as will be described in the following section. Similar plots for the Erf width parameter σ, and for the exponential decay constant λ are shown in Figs. 5.16 and 5.17.

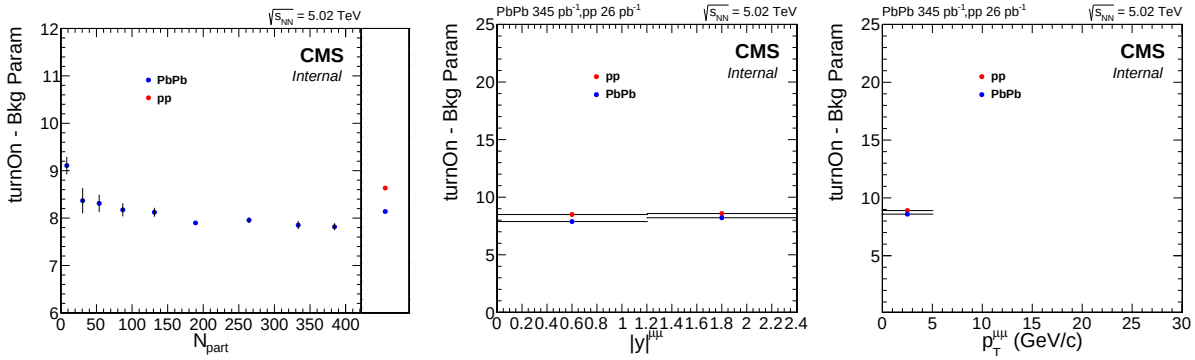

Figure 5.15: The Erf mean parameter μ fit results vs. centrality (left), y (center), and p_T (right).

Note that the plot of the μ parameter as a functiong of centrality has a zero-suppressed vertical axis. All the other frames do not. The blue points are for the Pb+Pb results and the red points are for $p+p$ fits. The parameters of the background model can change. For example, a change in the kinematics of the bin is expected to change the shape of the kinematic turn-on modeled with the μ parameter. The shape of the underlying invariant

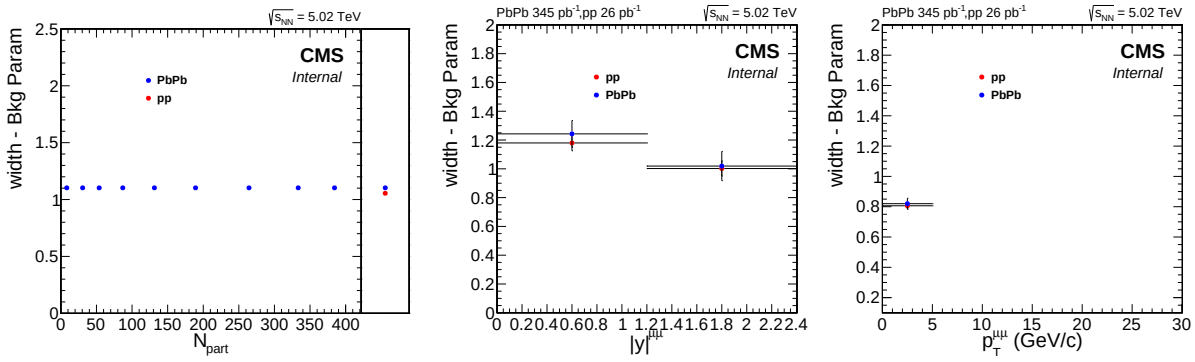

Figure 5.16: The Erf width parameter σ fit results vs. centrality (left), y (center), and p_T (right).

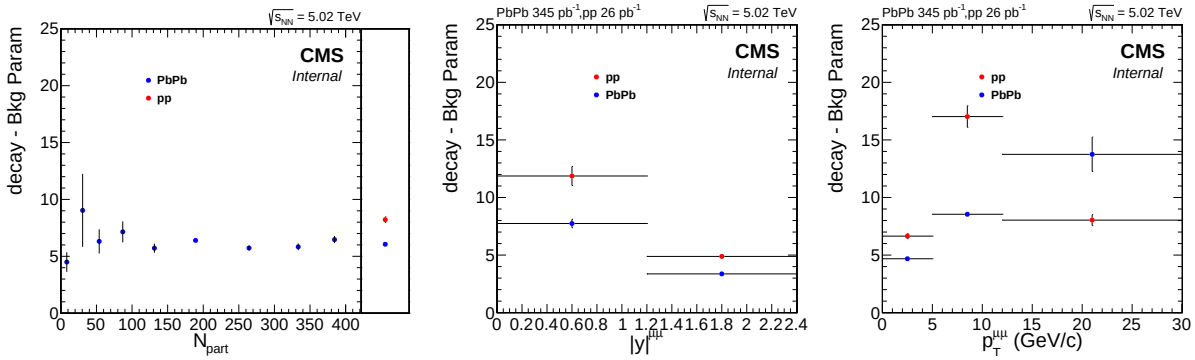

Figure 5.17: The exp decay parameter λ fit results vs. centrality (left), y (center), and p_T (right).

mass distribution, containing contributions from combinatorial background, Drell-Yan muon pairs, and muon pairs coming from uncorrelated charm and bottom semi-leptonic decays, can also change with centrality and kinematics. The width parameter is observed to remain constant as a function of centrality and is the same value within errors for $p+p$ and Pb+Pb. This is expected since the width of the Erf is driven largely by resolution which remains relatively constant across all centrality bins. In order to improve the stability of the fits, for the nominal results as a function of centrality, we therefore hold the width parameter fixed to the Pb+Pb centrality integrated value ($\approx$ 1.1 GeV/c^2) shown in the left sub-panel of the σ as a function of centrality plot of Fig. 5.16. The p_T- and y-dependent fits had all background parameters free. Note also that in the p_T plots for the μ and σ parameters, only the lowest p_T bin is displayed. In the bins with

higher dimuon p_T, the effect of the cut on single muons of $p_T(\mu) > 4$ GeV/c produces a kinematic turn-on effect at invariant masses below our fitting range. We therefore do not need to include the Erf to describe the background shape in the fit. Hence the two p_T bins above 5 GeV/c only need the exponential PDF with the decay constant λ shown in Fig. 5.17, right, for all p_T bins.

Finally, the fit function $\mathcal{F}$ can be summarized as the sum of signal events and background events:

$$\mathcal{F}(m_{\mu\mu};\mathcal{N}_{1S},\mathcal{R}_{21},\mathcal{R}_{31},\mathcal{N}_{\rm bkgd},m_0,\mu,\sigma,\lambda) = \mathcal{S}(m_{\mu\mu};\mathcal{N}_{1S},\mathcal{R}_{21},\mathcal{R}_{31},m_0) + \mathcal{N}_{\rm bkgd}\mathcal{B}(m_{\mu\mu};\mu,\sigma,\lambda) \quad (5.8)$$

where the normalization $\mathcal{N}_{\rm bkgd}$ is the number of background dimuons.

5.1.4 Yield and Ratio extraction

This section details the fitting of the opposite-sign dimuon mass spectra using the PDFs described in the previous sections. We begin with the integrated results in $p+p$ and Pb+Pb and then move on to the centrality, ${p_T}^{\mu\mu}$, and $y^{\mu\mu}$ dependent bins.

5.1.4.1 Integrated fits

Figure 5.18 shows the invariant mass distribution and the fit using Eq. 5.8, where the left panel shows the $p+p$ distribution and the right panel the Pb+Pb distribution. The data points are the solid black circles in the top panels. The total fit functions are represented by a solid blue line, representing the signal plus background, while a dashed blue line represents the background-only component of Eq. 5.8. The magenta, red, and green lines represent the signal PDF of the Υ(1S), Υ(2S), and Υ(3S)respectively. The bottom panels in each case show the pull distribution, i.e. the difference between the data points and the fit function divided by the error. The χ^2 per degree of freedom, obtained from the fit in the top panel, is displayed in the bottom panel also.

The data in Fig. 5.18 are integrated in the p_T range 0–30 GeV/c, and in the rapidity range $|y| < 2.4$. For the Pb+Pb data, we integrate over the 0–100% centrality range. For both the $p+p$ and the Pb+Pb data, the χ^2 per degree of freedom is close to unity,

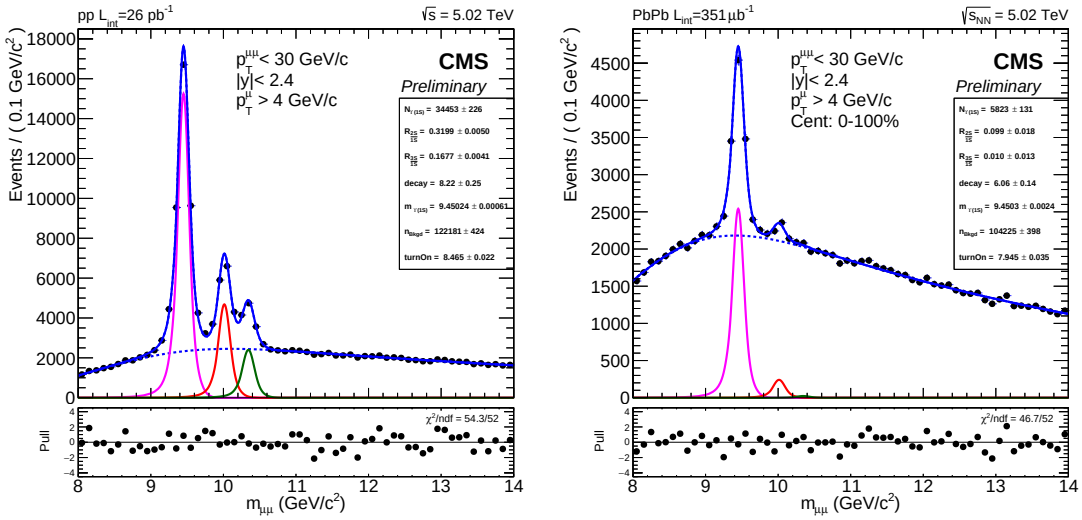

Figure 5.18: Fit to the $p+p$ (left) and Pb+Pb (right) invariant mass distributions using a double Crystal Ball function, where the data are integrated over p_T and y, and for the case of Pb+Pb also over all the centrality bins used in the analysis. The data are black points and the lines are the fits, with more details in the text.

indicating a reasonable goodness of fit (we remind the reader that the fits are done using the unbinned data and with the maximum likelihood method, so the χ^2 is kept simply as a goodness-of-fit measure, but it does not play a role in the fit). The pull distribution in the bottom sub-panel shows the points have typical deviations of less than 3σ and no systematic deviations in the region of interest.

The results from the $p+p-$integrated fit and of the Pb+Pb$-$integrated fit are used in the extraction of the double ratio for the 0–100% bin. We also use the data in Fig. 5.18 to extract the 95% confidence upper limits on the Υ(3S) double ratios for the 0–100% centrality integrated Pb+Pb bin. The $p+p$ data in Fig. 5.18 is also used for the denominator for all the bins of the double ratios as a function of centrality since $p+p$ collisions do not have centrality information because of the system size.

5.1.4.2 Centrality Binning

The centrality binning for the Pb+Pb data for the extraction of the Υ(2S) single ratios is as follows: Centrality [%]: $\in$ [0–5], [5–10], [10–20], [20–30], [30–40], [40–50], [50–60], [60–70], and [70–100].

The most central bins are shown in Fig. 5.19, with the top 5% in the left panel and

the 5–10% centrality bin in the right panel. The color scheme and layout of the figures are the same as for the integrated bins in Fig. 5.18. The χ^2 per degree of freedom is also close to unity for of the figures displaying centrality results. The most peripheral bin is shown in Fig. 5.23 where we see the least amount of data but also an absence of Υ(3S) even in the most peripheral case.

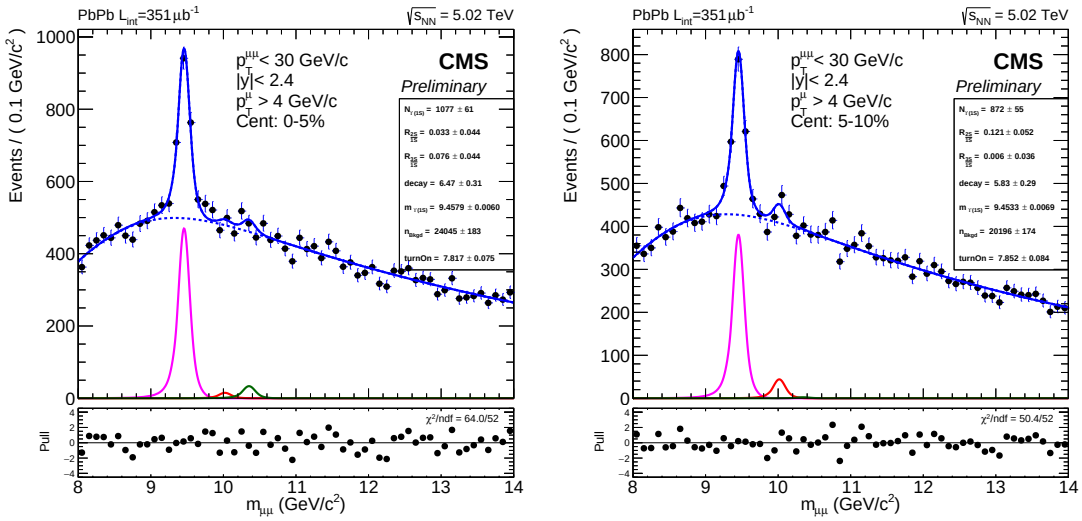

Figure 5.19: Fits to Pb+Pb dimuon mass data, for centrality bins [0-5]% (left) and [5-10]% (right). The data are black points and the lines are the fits, with more details in the text.

Most of the Υ data are in the most central events, as expected for hard processes which roughly scale with the number of binary collisions. Of course, the precise details of this scaling are the physics of interest in this thesis. From these figures, we extract the Υ(2S) single ratios as a function of centrality that are used to form the double ratio.

5.1.4.3 Transverse Momentum Binning

The p_T binning used for this analysis is as follows: p_T [GeV/c]: $\in$ [0–5.0], [5.0–12.0], [12.0–30.0].

Figures 5.24, 5.25, and 5.26 show the dimuon invariant mass distributions around the Υ peak in the relevant p_T bins. Figure 5.24 shows the lowest p_T bin in the analysis, [0–5.0] GeV/c, for $p+p$ data in the left panel and for Pb+Pb data in the right panel. The effect of the kinematic peak due to the single muon p_T cut is most visible in this lowest p_T bin. The fits for this p_T bin include the error function term, as discussed in Sec 5.1.3. The fits

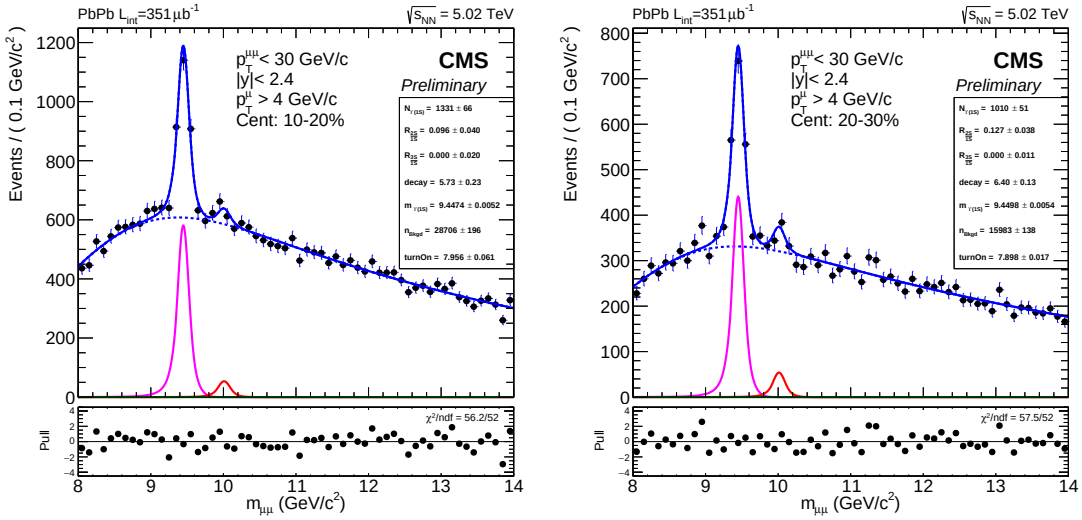

Figure 5.20: Fits to Pb+Pb dimuon mass data, for centrality bins [10-20]% (left) and [20-30]% (right). The data are black points and the lines are the fits, with more details in the text.

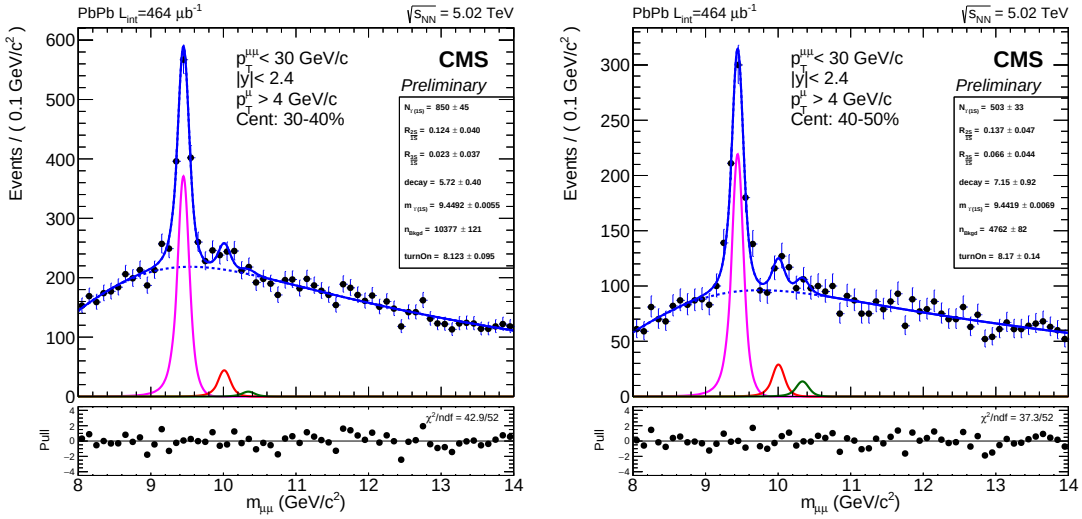

Figure 5.21: Fits to Pb+Pb dimuon mass data, for centrality bins [30-40]% (left) and [40-50]% (right). The data are black points and the lines are the fits, with more details in the text.

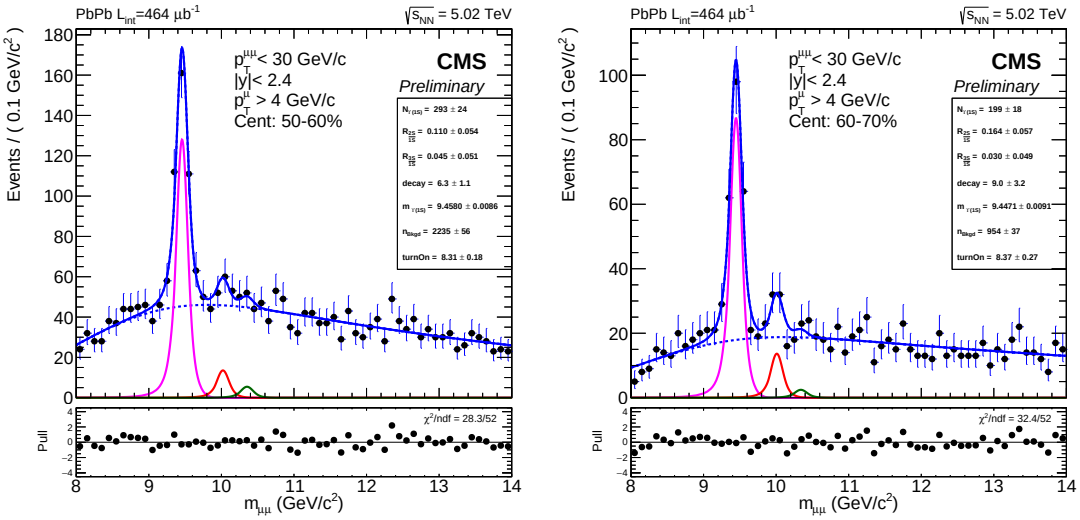

Figure 5.22: Fits to Pb+Pb dimuon mass data, for centrality bins [50-60]% (left) and [60-70]% (right). The data are black points and the lines are the fits, with more details in the text.

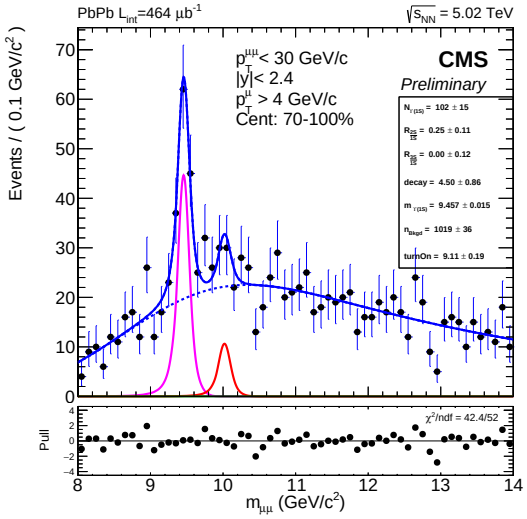

Figure 5.23: Fit to Pb+Pb dimuon mass data for the most peripheral bin [70-100]%. The data are black points and the lines are the fits, with more details in the text.

in Figures 5.25 and 5.26, done for the p_T [5.0–12.0] GeV/c bin and the [12.0–30.0] GeV/c bin (respectively), do not need the error function term and only include the exponential. The color scheme for the figures are again the same as for the integrated bins in Fig. 5.18.

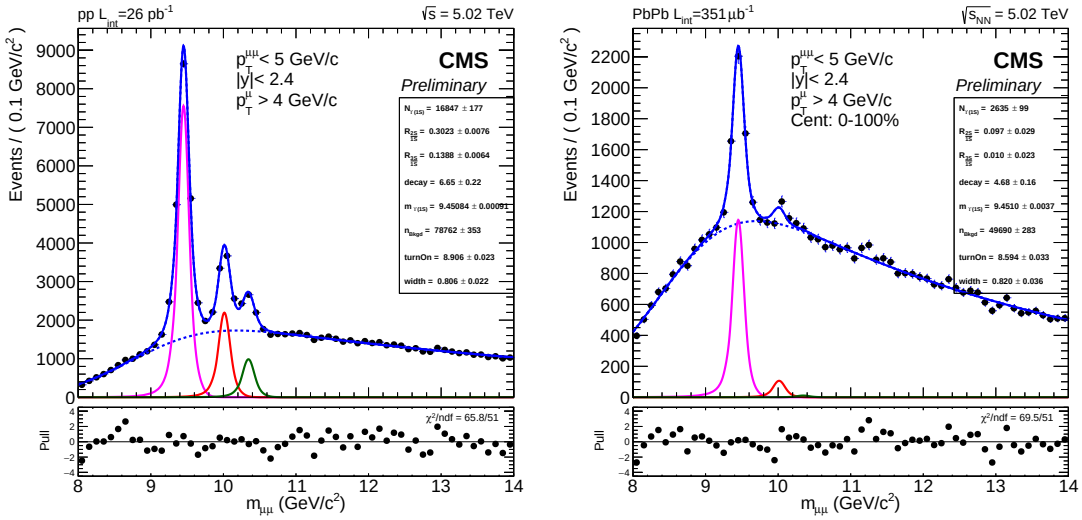

Figure 5.24: Fit to $p+p$ (left) and Pb+Pb (right) for p_T [GeV/c] $\in$ [0-5.0]. The data are black points and the lines are the fits, with more details in the text.

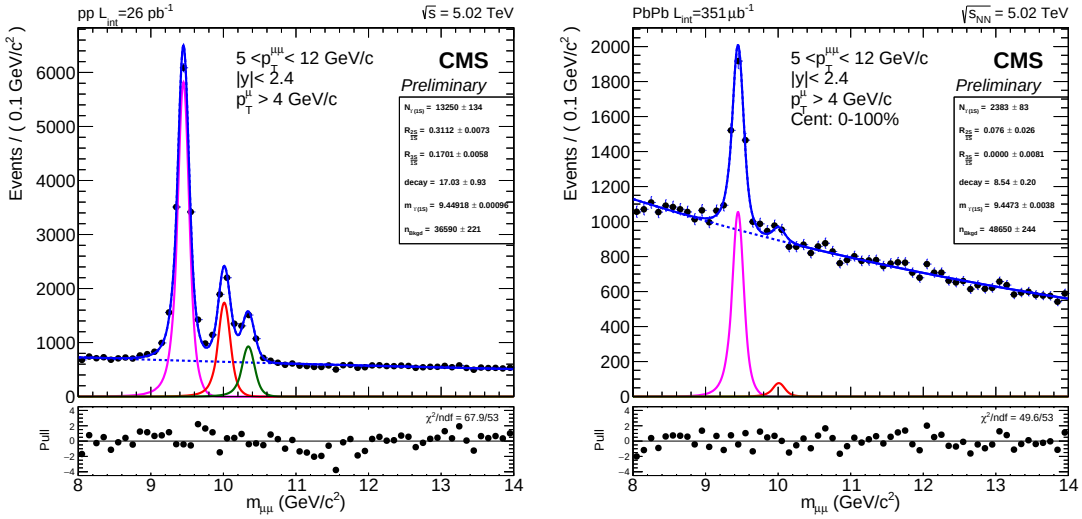

Figure 5.25: Fit to $p+p$ (left) and Pb+Pb (right) for p_T [GeV/c] $\in$ [5.0-12.0]. The data are black points and the lines are the fits, with more details in the text.

5.1.4.4 Rapidity Binning

The rapidity binning for this analysis is as follows: $|y^{\mu\mu}|$: $\in$ [0–1.2], and [1.2–2.4].

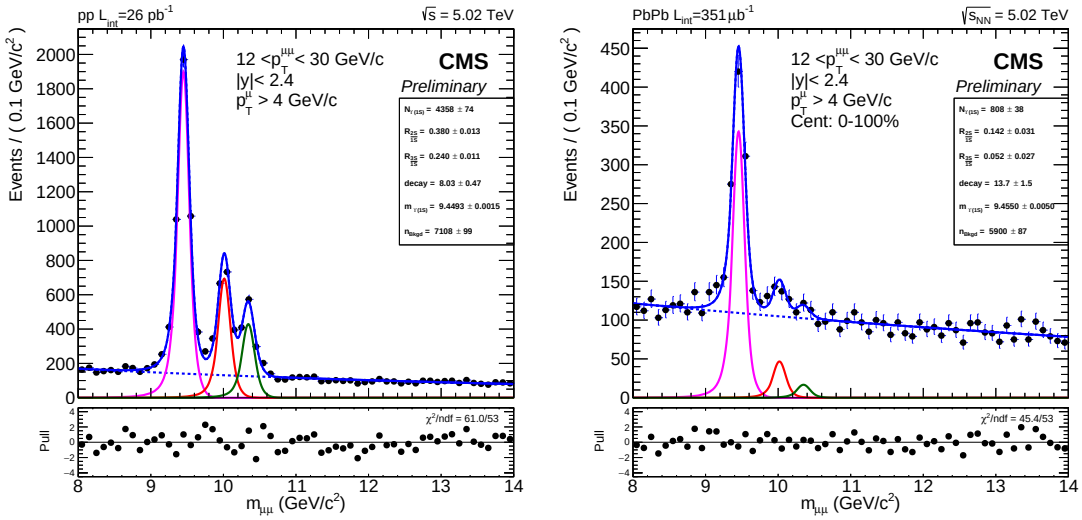

Figure 5.26: Fit to $p+p$ (left) and Pb+Pb (right) for p_T [GeV/c] $\in$ [12.0-30.0]. The data are black points and the lines are the fits, with more details in the text.

The figures below show the dimuon invariant mass distributions around the Υ peak in the relevant y bins. Figure 5.27 shows the dimuon invariant mass distribution in the y [0–1.2] bin, and Fig. 5.28 shows the distribution in the $y \in$ [1.2–2.4] bin where one can see the broadening of the mass peak as described earlier as motivation for the double CB in the signal PDF. Note that both the mid-rapidity, Fig. 5.27, and forward rapidity, Fig. 5.28, bins have reasonable pulls and chi-squares, indicating that the broadening of the mass distribution is appropriately modeled in the MC simulations. See Tables 5.2 and 5.3 for a comparison of the σ_0 and x parameters in these bins. The color scheme and layout of the figures are the same as for the integrated bins in Fig. 5.18.

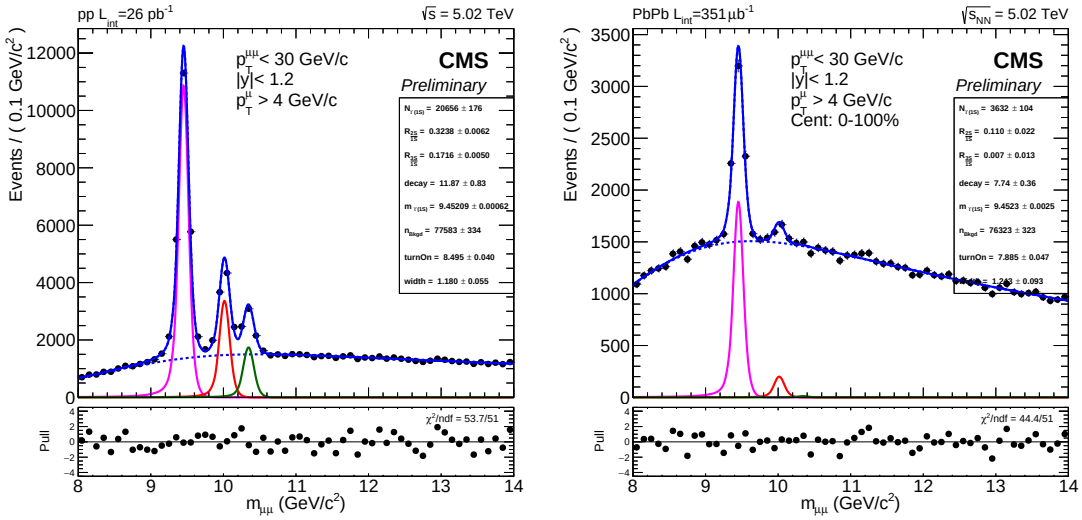

Figure 5.27: Fit to $p+p$ (left) and Pb+Pb (right) for $|y^{\mu\mu}| \in$ [0-1.2]. The data are black points and the lines are the fits, with more details in the text.

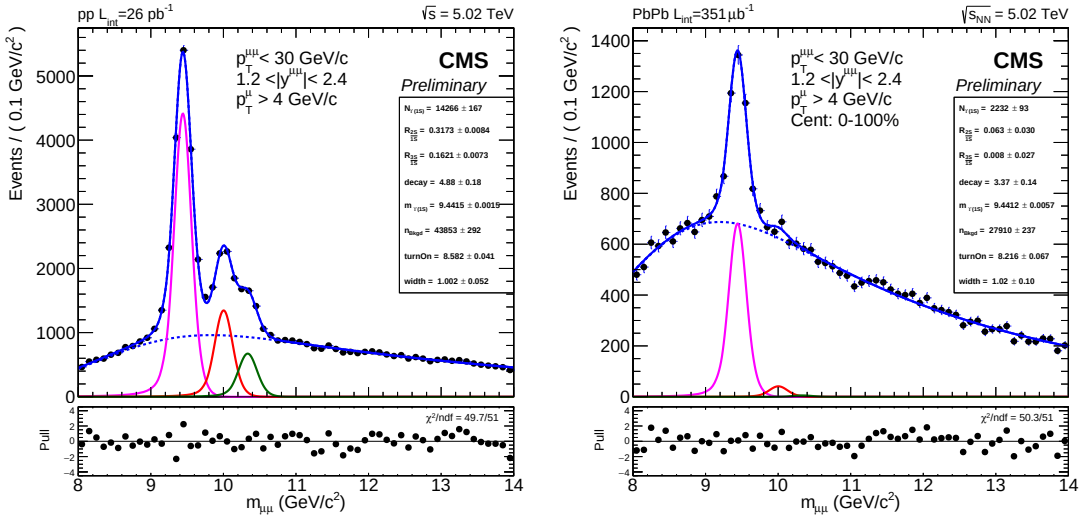

Figure 5.28: Fit to $p+p$ (left) and Pb+Pb (right) for $|y^{\mu\mu}| \in$ [1.2-2.4]. The data are black points and the lines are the fits, with more details in the text.

5.1.5 Single Ratios

The single ratios are obtained from the fits, as they are parameters that are used to construct the signal PDF. We present the single ratio parameters $\mathcal{R}_{21}$ in Fig. 5.29 for reference. The single ratios shown here are not corrected for acceptance or efficiency. This will be done in a follow-up analysis, but all the ingredients to do so are contained in this analysis. However, it is worth noting that these could be comparable to theoretical calculations as long as the single muon acceptance cut of $p_T(\mu) > 4$ GeV/c is applied to the theory calculation as well.One can see that, except for the most peripheral bin, the Pb+Pb single ratios are much lower than the $p+p$ single ratios. The double ratios are used to quantify this relative suppression, and are the focus of this thesis.

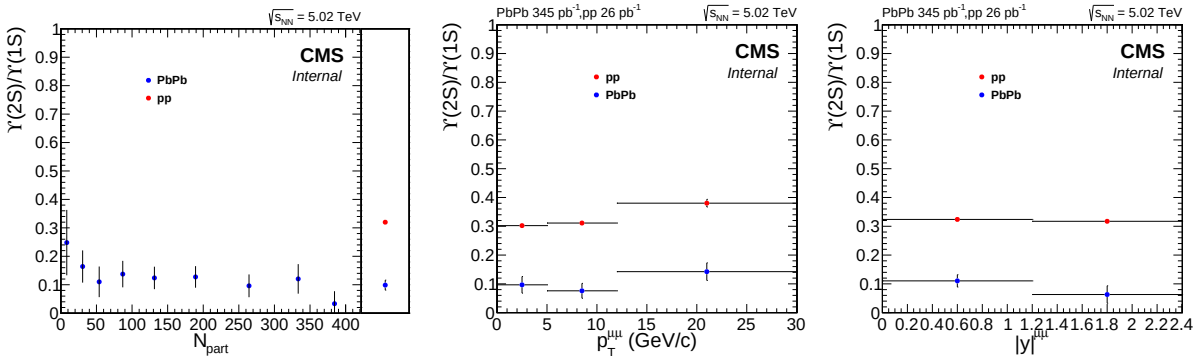

Figure 5.29: The single ratio $\mathcal{R}_{21}$ vs. centrality (left), p_T (center), and y (right).

For completeness, we also show the Υ(1S) mass parameter, m_0, used in constructing the signal PDF in Fig. 5.30. The Υ(1S) mass can deviate from the PDG value due to imperfect muon momentum calibrations, which will translate to systematic shifts in the invariant mass scale. The data vs. MC differences indicate that there is such a momentum scale difference that is not present in simulations. However, we do expect that the scale shifts be similar between $p+p$ and Pb+Pb and that they be consistent with those observed in the analysis of the 2.76 TeV data.

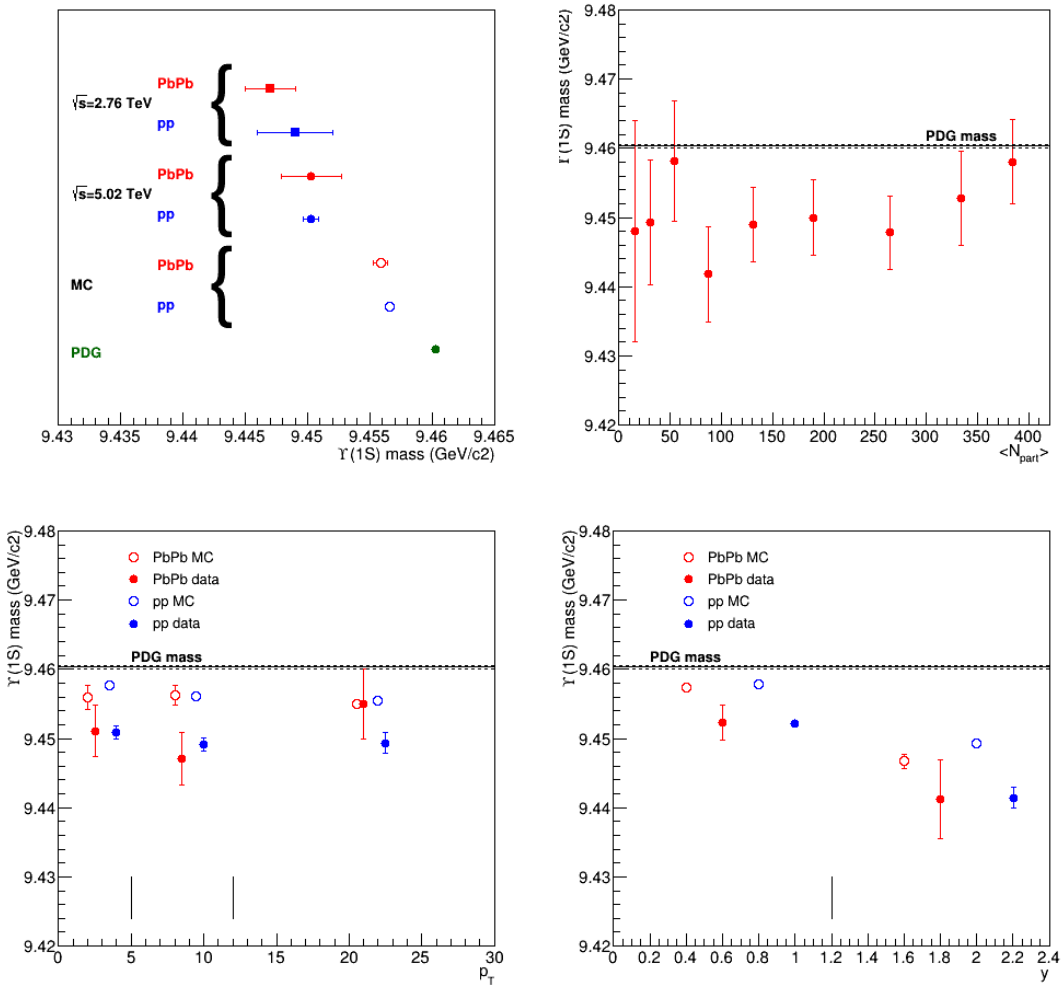

Figure 5.30: The Υ(1S) mass parameter. Top left, comparison of 2.76 TeVand 5.02 TeVresults with simulations and with PDG value, followed by Υ(1S) mass as a function of centrality (top right), p_T (bottom left), and y (bottom right).

5.1.6 Upper limit extraction of Υ(3S)

This section details the upper limit extraction for the double ratio of the Υ(3S). Fits are performed to the $p+p$ and Pb+Pb data as described in Section 5.1. The analysis bins for this study have wider centrality percentile bins than for the Υ(2S)$\dot{\text{T}}$hey were chosen to increase the statistics of the Υ(3S) in each bin. The binning for the Υ(3S) is given by: Centrality [%]: $\in$ [0–10], [10–30], [30–50], and [50–100].

Once the fits are performed, they are then used as input for the Feldman-Cousin (FC) CLs prescription [51, 52] to extract 95% and 68% confidence intervals. The expected value for most of the analysis bins of the double ratio, obtained from their respective fits, are close to zero. The confidence level intervals are used to determine how well we know these values.

The Figures 5.31 and 5.32 detail the fits to the various centrality bins for the obtaining the Υ(3S) double ratios as well as the confidence level for the two cases, 95% and 68% confidence intervals.

The FC method is applied using `RooStats` and in particular the `HypoTestInverter` class. See the following slides for a `RooStats` tutorial on calculations such as these:
`https://agenda.infn.it/getFile.py/access?\contribId=15&resId=0&materialId=slides&confId=5719`
The test statistic as input for this calculation is the profile-likelihood ratio. We report the results for both the asymptotic and frequentist calculations. We then compare the calculations to check their agreement. To include systematic uncertainties in the calculation, we introduce nuisance parameters, employed as follows: will be used as nuisance parameters where the following will be employed:

- systematic uncertainty due to the deviation of double ratio from background PDF model variations;
- systematic uncertainty due to the deviation of double ratio from signal PDF variation;
- systematic uncertainty due to the deviation of the double ratio of the efficiencies

from unity.

The double ratio, using the notation introduced in Eq. (5.6) is defined as follows:

$$\mathcal{DR}_{31} = \frac{\mathcal{R}_{31}|_{\mathrm{PbPb}}}{\mathcal{R}_{31}|_{pp}}$$

where in this calculation $\mathcal{R}_{31}|_{\mathrm{PbPb}}$ is a parameter allowed to vary between 0 and 1 while $\mathcal{R}_{31}|_{pp}$ is held constant to the fit value. We also performed a simultaneous fit of the $p+p$ and Pb+Pb data in this process as an alternative procedure to ensure the correct values are extracted for the double ratio and its correlations.

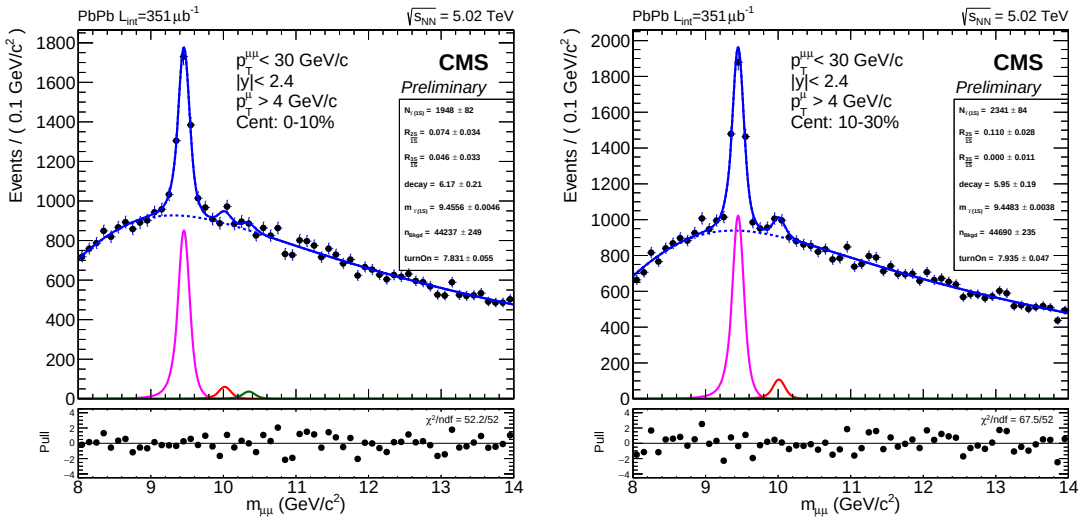

Figure 5.31: Fits to PbPb dimuon mass data [0-10]% (left) and [10-30]% (right). These fits to data are used in the extraction of the Υ(3S) upper limits.

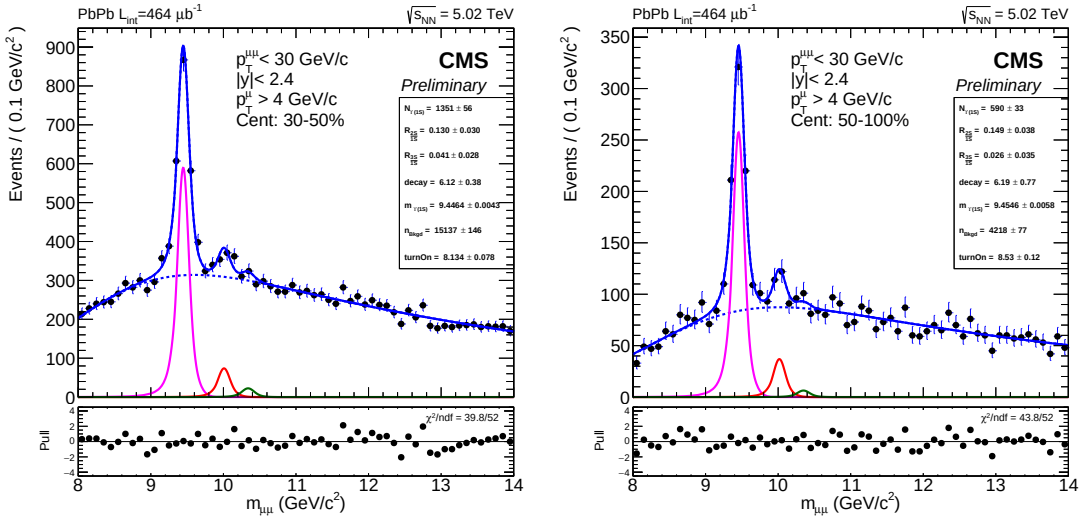

Figure 5.32: Fits to Pb+Pb dimuon mass data [30-50]% (left) and [50-100]% (right). These fits to data are used in the extraction of the Υ(3S) upper limits.

5.1.6.1 95% Confidence Level (CL) Results

Figure 5.33 shows the integrated (0-100%) in Pb+Pb and integrated $p+p$ result taking the fits from Figure 5.18 as input for the 95%, Asymptotic [53] (left) and the Frequentist (right). The red horizontal lines indicate the p-values for p = 0.05 (left) and p = 0.32 (right). The red points show the calculated p-values represented as the ordinate plotted for a given value of the parameter of interest, in this case the double ratio, represented in the abscissa. The location where the p-value curve reaches the specified level, e.g. p = 0.05, that abscissa is taken as the limit for the corresponding confidence interval (95% for p = 0.05). Additionally the location where the p-value has a maximum indicates that that is the point where if one did a fit, you would expect the parameter to reach its maximum likelihood, i.e. that $\mathcal{DR}_{31} \approx 0.07$ in Fig. 5.33. The Asymptotic and the Frequentist scan (which takes a lot more cpu time) are in good agreement.

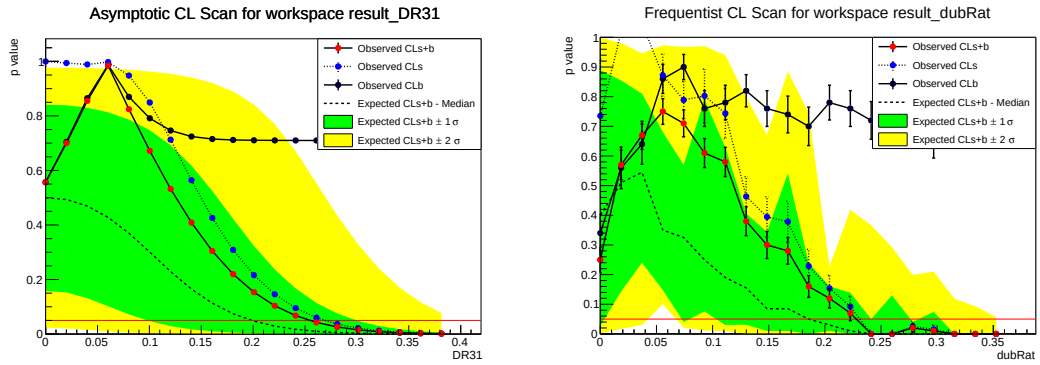

Figure 5.33: 95% Confidence scan of the Υ(3S) double ratio with the Asymptotic calculation (left) and Frequentist (right) in centrality range [0–100]%.

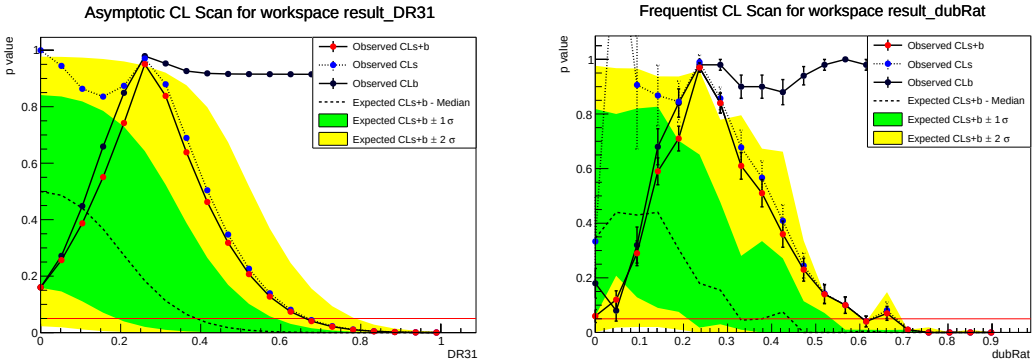

Figure 5.34: 95% Confidence scan of the Υ(3S) double ratio with the Asymptotic calculation (left) and Frequentist (right) in centrality range [0–10]%.

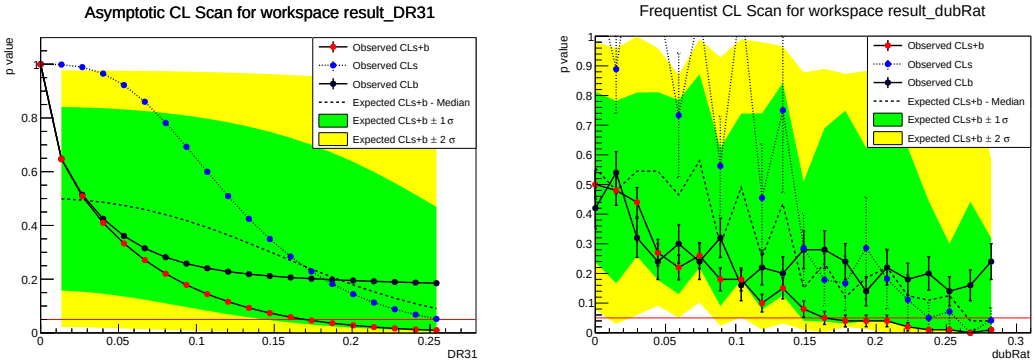

Figure 5.35: 95% Confidence scan of the Υ(3S) double ratio with the Asymptotic calculation (left) and Frequentist (right) in centrality range [10–30]%.

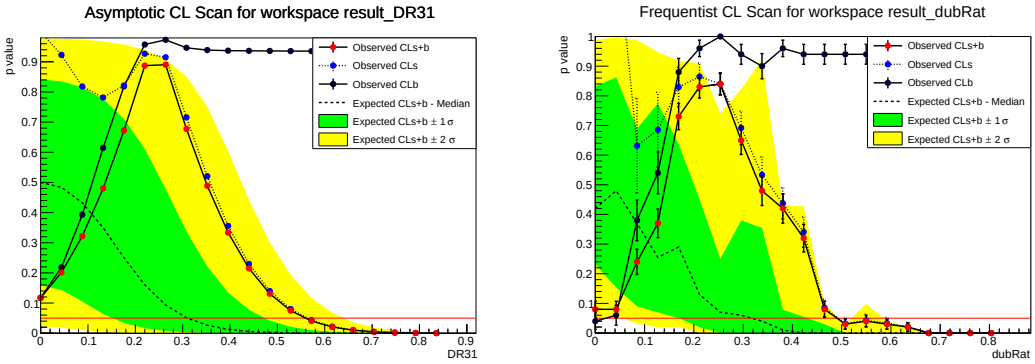

Figure 5.36: 95% Confidence scan of the Υ(3S) double ratio with the Asymptotic calculation (left) and Frequentist (right) in centrality range [30–50]%.

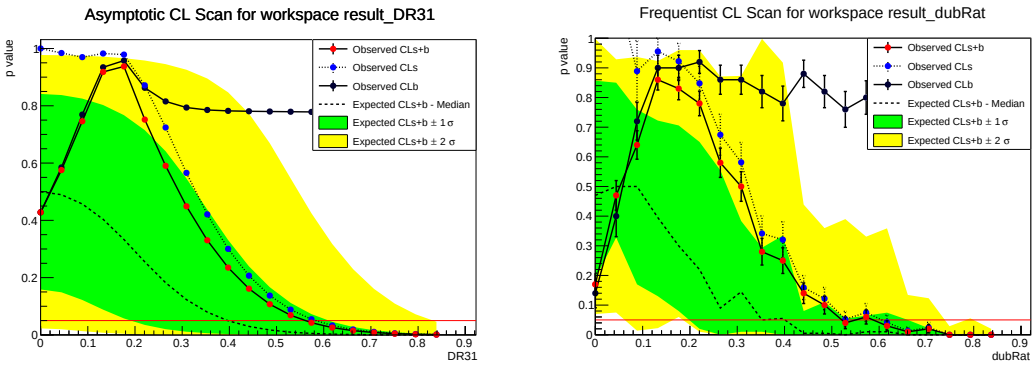

Figure 5.37: 95% Confidence scan of the Υ(3S) double ratio with the Asymptotic calculation (left) and Frequentist (right) in centrality range [50–100]%.

5.1.6.2 68% Confidence Level (CL) Results

Figure 5.39 scans have red points below the red line both at low values of the $\mathcal{DR}_{31}$ and at high values of the $\mathcal{DR}_{31}$ allowing extraction of a confidence interval that has both lower and upper bounds at this confidence level. Fore Figures 5.40 and 5.41 the Asymptotic scan (left) indicates that the limit is going to be very small, so you then chose to zoom in to small values when you did the Frequentist scan (right).

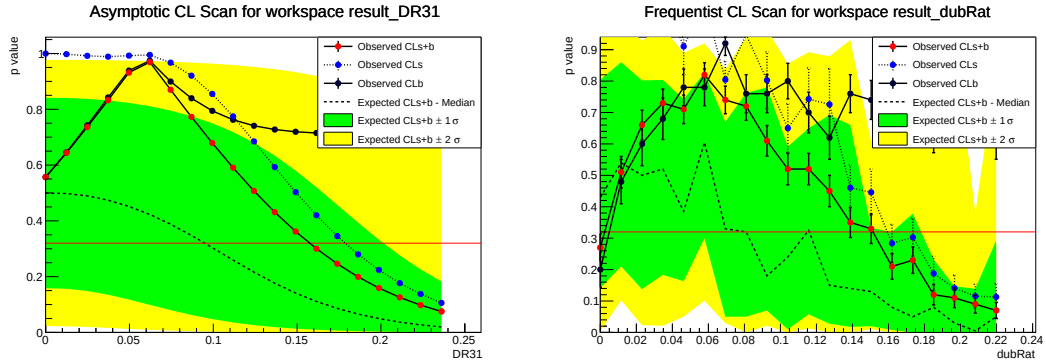

Figure 5.38: 68% Confidence scan of the Υ(3S) double ratio with the Asymptotic calculation (left) and Frequentist (right) in centrality range [0–100]%.

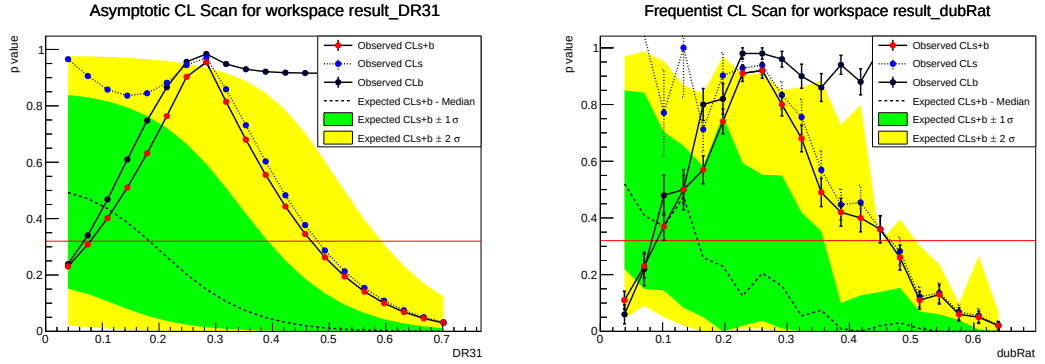

Figure 5.39: 68% Confidence scan of the Υ(3S) double ratio with the Asymptotic calculation (left) and Frequentist (right) in centrality range [0–10]%.

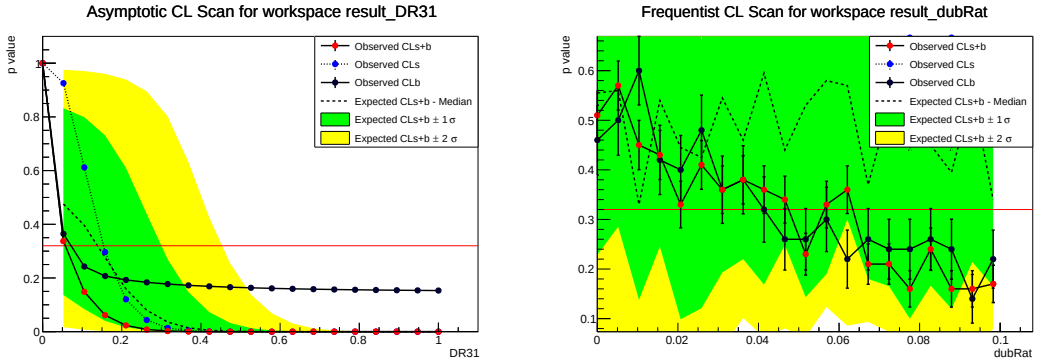

Figure 5.40: 68% Confidence scan of the Υ(3S) double ratio with the Asymptotic calculation (left) and Frequentist (right) in centrality range [10–30]%.

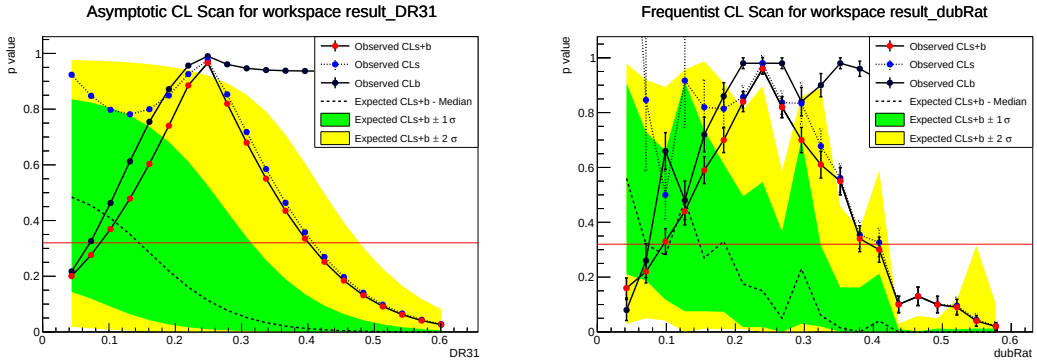

Figure 5.41: 68% Confidence scan of the Υ(3S) double ratio with the Asymptotic calculation (left) and Frequentist (right) in centrality range [30–50]%.

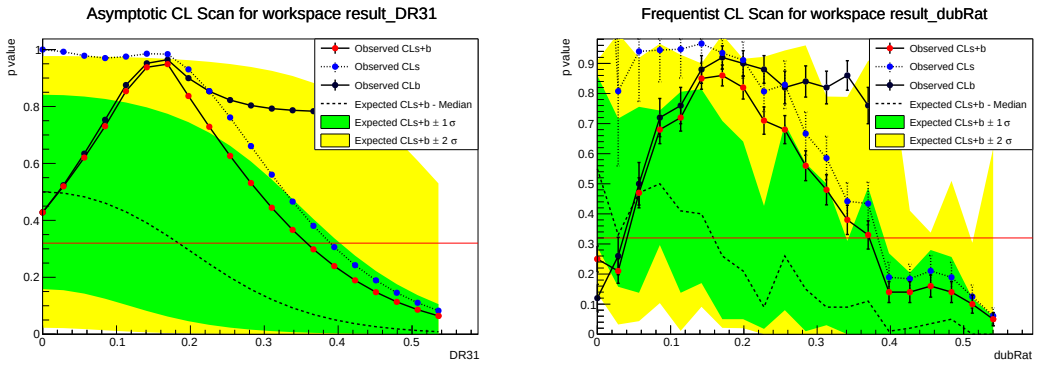

Figure 5.42: 68% Confidence scan of the Υ(3S) double ratio with the Asymptotic calculation (left) and Frequentist (right) in centrality range [50–100]%.

Figure 5.43 shows a comparison of the confidence level interval calculated for the asymptotic (red boxes) and frequentist scan (blue boxes) for the 68% CL. Figure 5.44 shows a comparison of the confidence level interval calculated for the asymptotic (red arrows) and frequentist scan (blue arrows) for the 95% confidence level upper limit. It was chosen to use the asymptotic scan for the final result due to its close value to the frequentist as seen in the figures as well as its fast computation, which allowed for the analysis to be done multiple times for various changes in systematic values and overall approach.

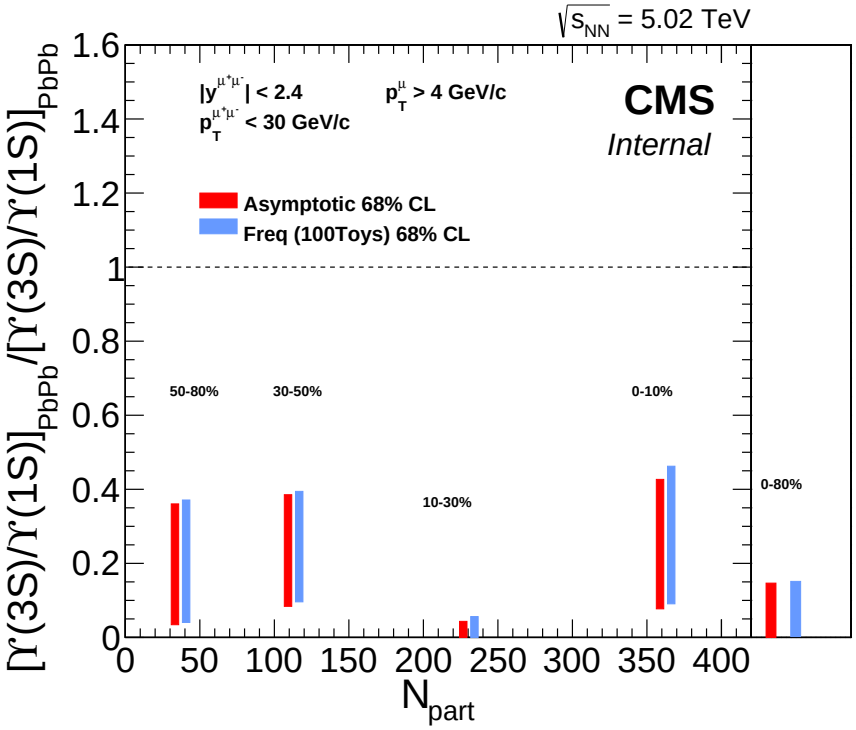

Figure 5.43: Comparison of the Double ratio of the $\Upsilon(3S)$ for the Asypmtotic (red boxes) and the Frequentist (blue boxes) for the 68% CL

In addition to the confidence level upper limit on the Υ(3S) double ratio, I also calculated the confidence level upper limit was calculated similarly for the Υ(2S) centrality 0–5% bin. This was deemed necessary because the single ratio in this bin, as seen in the previous section, has a statistical error larger than the value itself, implying a value of $\mathcal{DR}_{21}$ consistent with zero. Figure 5.45 shows the confidence level scan for the Υ(2S) in the most central bin (0–5%) using the asymptotic calculation for the 68 and 95% confidence

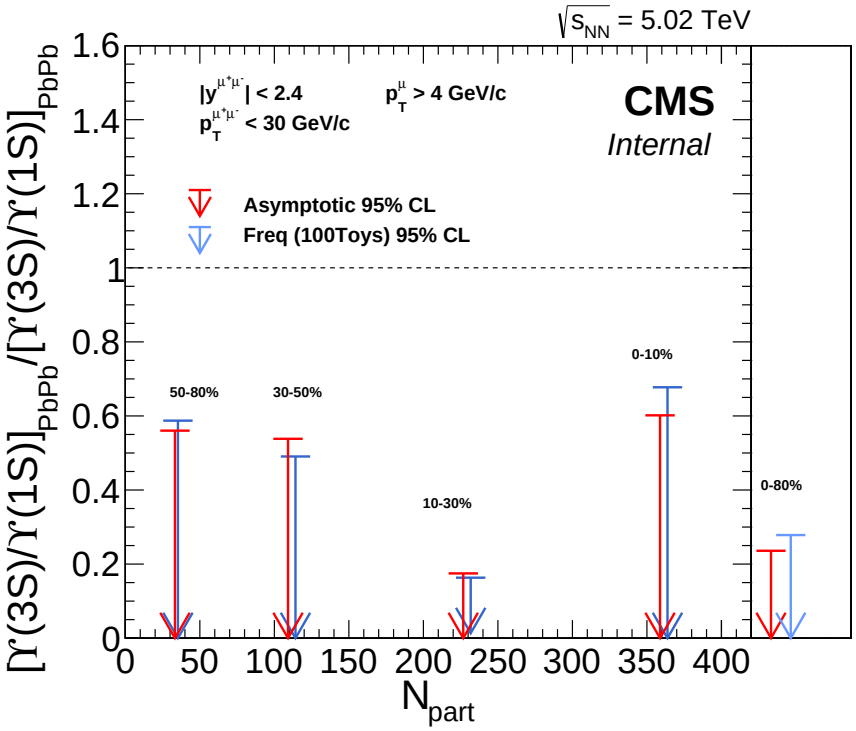

Figure 5.44: Comparison of the Double ratio of the $\Upsilon(3S)$ for the Asypmtotic (red arrows) and the Frequentist (blue arrows) for the 95% CL

level intervals.

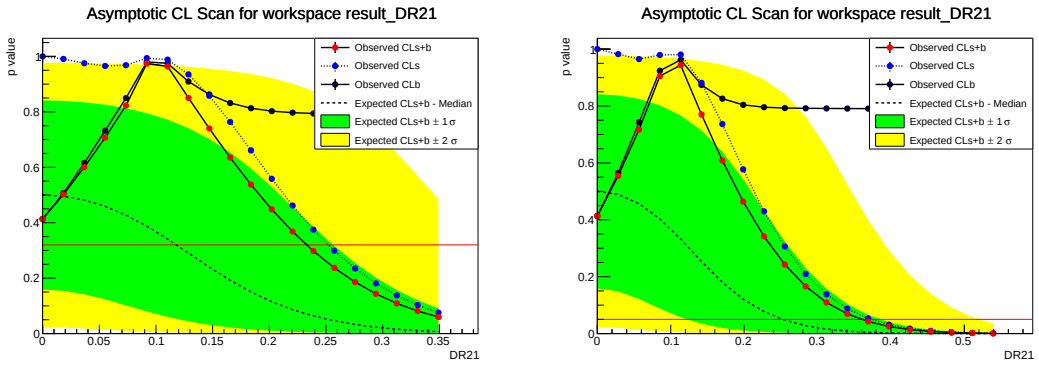

Figure 5.45: Confidence scan of double ratio of $\Upsilon(2S)$ with Asymptotic calculation for 68% (left) and 95% (right) in Centrality [0-5]%

5.1.7 Tabulated results

This section details all the results of the fits in Section 5.1.4. In particular, the yield $\mathcal{N}_{1S}$ and the single ratios ($\mathcal{R}_{21}$ and $\mathcal{R}_{31}$) are tabulated. Table 5.6 contains the resulting fits to data for the kinematic study of the yields and ratios as a function of dimuon p_T and y.

Table 5.6: Fit results of signal yields and ratios for $p+p$ and Pb+Pb.

Fit Results	$p+p$ value $\pm$ stat. error			PbPb value $\pm$ stat. error	
Kinematic Region	$\mathcal{N}_{1S}$	$\mathcal{R}_{21}$	$\mathcal{R}_{31}$	$\mathcal{N}_{1S}$	$\mathcal{R}_{21}$
$p_T < 5.0$	16847±177	0.302±0.008	0.139±0.006	2634±99	0.097±0.029
$5.0 < p_T < 12.0$	13250±134	0.311±0.007	0.170±0.006	2383±82	0.076±0.026
$12.0 < p_T < 30.0$	4358±74	0.380±0.013	0.240±0.011	808±38	0.142±0.031
$\|y\| < 1.2$	20656± 176	0.324±0.006	0.172±0.005	3632±104	0.110±0.021
$1.2 < \|y\| < 2.4$	14266 ± 167	0.317±0.008	0.162±0.007	2232±93	0.063±0.030

Table 5.7 contains the resulting fits to data for the yields and ratios as a function of event centrality (in % of Pb+Pb hadronic cross section). Integrated centrality values for Pb+Pb are also given, as well as the integrated $p+p$ results. The values for $\mathcal{R}_{31}$ are not present in Table 5.6 and Table 5.7 for Pb+Pb collisions because, as noted before, we extract upper limits due to the strong suppression observed for the Υ(3S). The upper limit results are given in Table 6.2 in the next chapter.

Table 5.7: Fit results for the signal yields in Pb+Pb centrality bins of the analysis, as well as for the centrality integrated 0–100% bin, and for $p+p$ data.

Fit Results	Yields/Ratios ± stat. error		
Centrality %	$\mathcal{N}_{1S}$	$\mathcal{R}_{21}$	$\mathcal{R}_{31}$
0-5	1077 ± 61	0.033 ± 0.044	-
5-10	872 ± 55	0.121 ± 0.052	-
10-20	1331± 66	0.096 ± 0.040	-
20-30	1010± 51	0.127 ± 0.038	-
30-40	850 ± 45	0.124 ± 0.040	-
40-50	503 ± 33	0.137 ± 0.047	-
50-60	293 ± 24	0.110 ± 0.054	-
60-70	199 ± 18	0.164 ± 0.057	-
70-100	102 ± 14	0.25 ± 0.11	-
0-100	5823 ± 130	0.099 ± 0.018	-
$p+p$	34452 ± 226	0.320 ± 0.005	0.168 ± 0.004

5.2 Efficiency and Acceptance

This section describes the estimation of the detector acceptance and muon trigger/identification efficiency. The acceptance is a measure of the coverage of the detector in which the muons can be reconstructed. It is constrained by the geometry of the muon detectors and p_T of the muon. The magnitude of the magnetic field, as well as the geometry of the solenoid itself, are such that muons need a transverse momenta of at least 3.5 GeV/c to reach the barrel region and 1.5 GeV/c to reach the endcap. The efficiency in this analysis can be defined as the probability for dimuons in the acceptance region to fire the trigger, be reconstructed in the tracker, and pass the muon ID cuts. The efficiency and acceptance corrections are expected to cancel in the double ratio since any correction for an Υ in Pb+Pb should cancel with any correction from an Υ in $p+p$. This allows us to not correct the yields or single ratios when forming the double ratio. We study the details of this cancellation and estimate uncertainties to any possible non-cancellation of these correction factors.

5.2.1 Reweighting the pythia distributions

The acceptance and efficiency correction factors are computed from PYTHIA simulations as described in 4.4. The kinematic distributions in PYTHIA are based on Leading Order (LO) diagrams of Quarkonia production, including singlet and octet contributions, and are good approximations of the distributions seen in data. However, they do not reproduce all the details of the data. As previously mentioned when computing the double ratio, the acceptance corrections in $p+p$ and Pb+Pb are expected to cancel. Any possible deviations from unity in the acceptance ratio arises from different kinematic distributions in $p+p$ and Pb+Pb which could be due to the physics of interest. In order to study any possible deviations, it is necessary to reweight the p_T and $|y|$ distributions in the MC simulations so that the distributions match those seen in real data.

The distributions obtained in data and MC simulation of dimuon p_T for Υ(1S) and Υ(2S) are given in Fig. 5.46. The red points are the Pb+Pb data while the black points are the $p+p$ data. The corresponding colored histograms depict the MC simulation. The p_T distribution for each state in $p+p$ and Pb+Pb for both Data and MC was found to

Table 5.8: Fit Coefficient

	Υ state	n_1	n_2	T_1	T_2
pp	1S	2.003 ± 0.000	2.009 ± 0.000	3.809 ± 0.205	7.237 ± 0.494
	2S	3.986 ± 1.792	2.308 ± 0.124	4.041 ± 1.148	1.721 ± 0.354
PbPb	1S	1.780 ± 0.149	1.003 ± 0.001	7.343 ± 0.665	9.667 ± 0.142
	2S	99.999 ± 95.460	2.363 ± 0.181	7.005 ± 3.536	1.983 ± 1.162

follow the Tsallis distribution,

$$\frac{dN}{dp_T} = Cp_T[1 + \frac{(m_T - m)}{nT}]^{-n}, \tag{5.9}$$

where

$$C = \frac{(n-1)(n-2)}{nT[nT + (n-2)m]}, \quad m_T = \sqrt{m^2 + {p_T}^2}.$$

The Data/MC ratios, shown in Fig. 5.47, are fitted to a ratio of two Tsallis functions, used for weighting the MC p_T spectra. The coefficients of these fitted Data/MC functions are indicated in table 5.8 where "1" notes the first Tsallis parameters corresponding to data and "2" denotes the one parameters corresponding to MC.

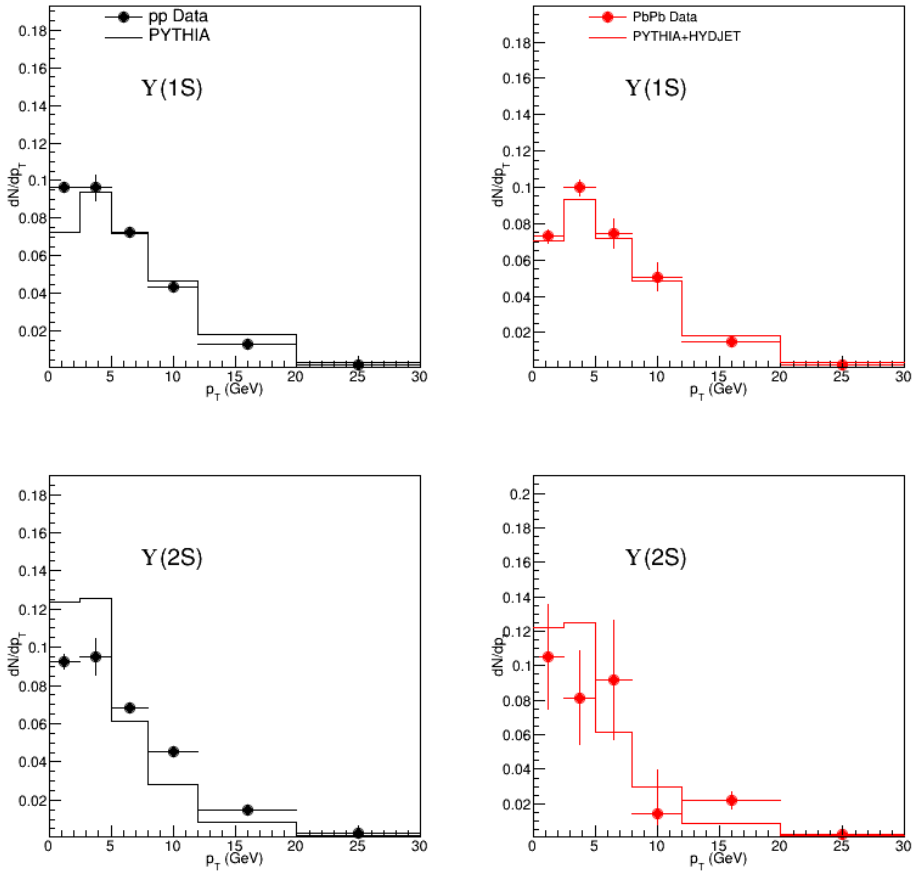

Figure 5.46: The measured p_T distributions compared to those obtained from PYTHIA simulations.

5.2.2 Acceptance

The acceptance is calculated using generator level non-embedded $(p+p)$ PYTHIA MC simulations for Υ(1S) and Υ(2S). The acceptance for single muons and dimuons are as mentioned in Eq. (4.2) and (4.3). In general, the acceptance is defined as the number of generated dimuons in the geometrical acceptance, as described in the previous equations, in the numerator and the total number of generated dimuons in the denominator. The acceptance is calculated for both the unweighted sample and one that is weighted by $p+p$ and Pb+Pb. A comparison of the resulting acceptance differences using the weighted Pb+Pb and $p+p$ data show that these differ by at most 1.4%. The acceptance values are detailed in Table 5.9, including ratios of reweighted Pb+Pb and $p+p$ data for the case

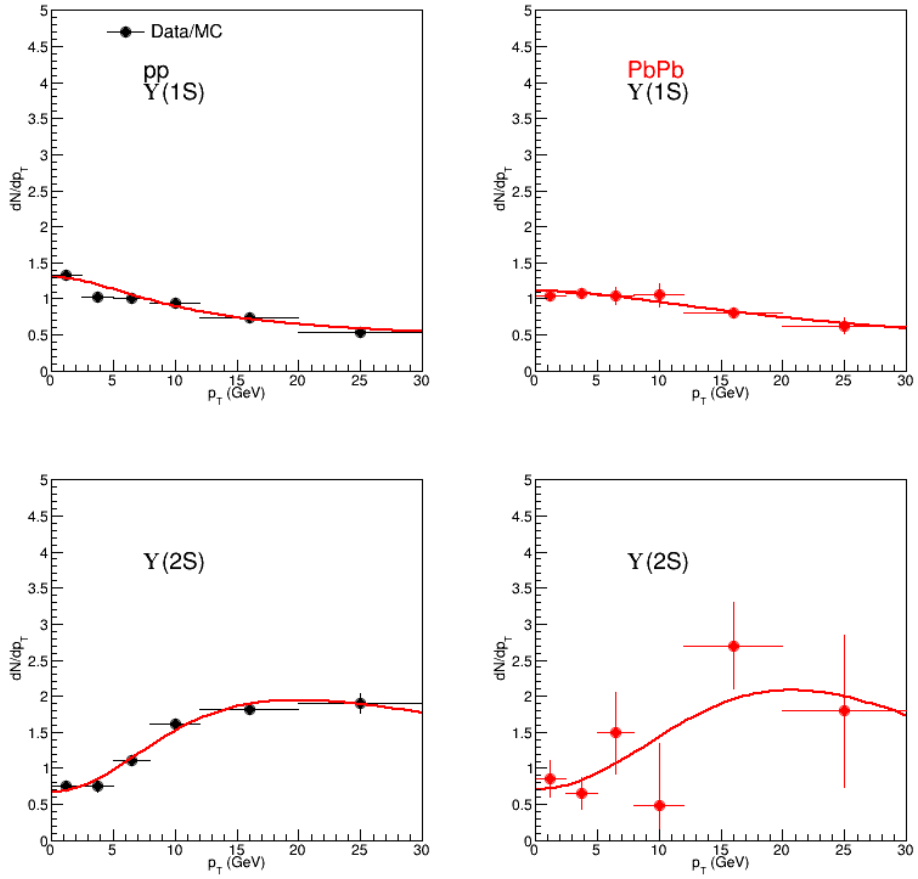

Figure 5.47: Data/MC ratios of p_T spectra and their fit functions, given by a ratio of Tsallis functions.

of the Υ(1S) and the computed single ratio, Υ(2S)/Υ(1S)), of the reweighted acceptance for each collision system. This study for the acceptance was not used for any possible corrections nor was it used for any systematic due to the small deviations, as well as, the possibility that the physics of interest would be corrected out of the results.

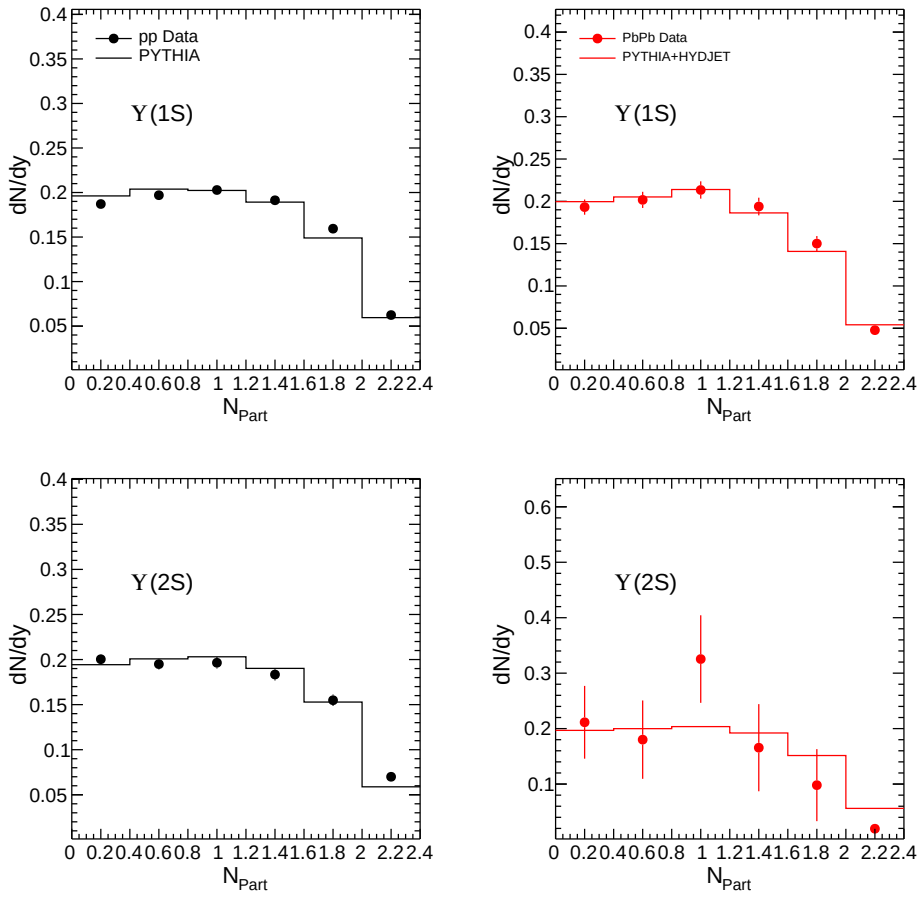

Figure 5.48: The measured data and PYTHIA distributions as a function of rapidity. Note the horizontal axis has an incorrect label.

5.2.3 Efficiency

This section details the reconstruction efficiency of dimuons in MC for both $p+p$ and Pb+Pb. The generated dimuons and single muons are first required to fall in within the acceptance of the detector. Additionally, the reconstructed dimuons must be ones that satisfy the trigger condition (`HLT_HIL1DoubleMu0`, as noted in Sec. 4.2), and its individual muons must pass the muon ID cuts for the appropriate charge. The list of the muon ID and dimuon variables and their cuts can be found in Section 4.5. The nominal efficiencies were calculated by applying a weighting factor obtained from the ratio of fits to the dN/dp_T spectrum as described in Section 5.2.1. The efficiency is defined as follows:

- **Denominator** The set of all generated dimuons that satisfy the acceptance condi-

Acceptance	Υ(1S)			Υ(2S)			Υ(1S)	2S/1S	
Bin	MC	pp	PbPb	MC	pp	PbPb	PbPb/pp	pp	PbPb
p_T, y integrated	0.225	0.218	0.221	0.272	0.275	0.276	1.014	1.261	1.249
$p_T < 2.5$ GeV/c	0.258	0.258	0.258	0.375	0.372	0.371	1.000	1.442	1.438
$2.5 < p_T < 5$ GeV/c	0.155	0.155	0.155	0.216	0.215	0.215	1.000	1.387	1.387
$5 < p_T < 8$ GeV/c	0.185	0.184	0.184	0.215	0.216	0.216	1.000	1.174	1.174
$8 < p_T < 12$ GeV/c	0.29	0.289	0.289	0.304	0.306	0.306	1.000	1.059	1.059
$12 < p_T < 30$ GeV/c	0.475	0.466	0.47	0.473	0.483	0.484	1.008	1.036	1.030
$\|y\| < 0.4$	0.253	0.244	0.247	0.304	0.309	0.311	1.012	1.266	1.259
$0.4 < \|y\| < 0.8$	0.251	0.243	0.246	0.303	0.308	0.309	1.012	1.267	1.256
$0.8 < \|y\| < 1.2$	0.251	0.242	0.245	0.302	0.307	0.308	1.012	1.269	1.257
$1.2 < \|y\| < 1.6$	0.249	0.241	0.244	0.302	0.306	0.307	1.012	1.270	1.258
$1.6 < \|y\| < 2.0$	0.221	0.216	0.218	0.270	0.270	0.270	1.009	1.250	1.239
$2.0 < \|y\| < 2.4$	0.098	0.096	0.097	0.119	0.117	0.117	1.010	1.219	1.206

Table 5.9: Acceptance, obtained from MC simulations, and by reweighting the simulation using Pb+Pb and $p+p$ p_T spectra measured in real data. Ratios of the acceptances from reweighted data, Pb+Pb/$p+p$, and for 2S/1S with both $p+p$ reweights and with Pb+Pb reweights are also shown.

tions in Sections 4.5.

- **Numerator** Consists of the subset of those dimuons in the denominator that are also successfully reconstructed as described above.

The efficiency is analyzed in the bins of this analysis as detailed in Section 4.5.2. The p_T, $|y|$ and centrality dependence of the efficiencies of Υ(1S) and Υ(2S) in the MC are calculated for Pb+Pb and $p+p$ and are shown in Figures 5.49 through 5.53. The centrality in CMS is measured in bins of 0.5% centrality therefore 200 is really 100%, as seen in the horizontal axis of these figures.

Table 5.10 shows the efficiency values and their asymmetric errors for $p+p$ Υ(1S), Pb+Pb Υ(1S), $p+p$ Υ(2S), and Pb+Pb Υ(2S) in bins of p_T, $|y|$, integrated p_T and $|y|$, and Centrality as appropriate.

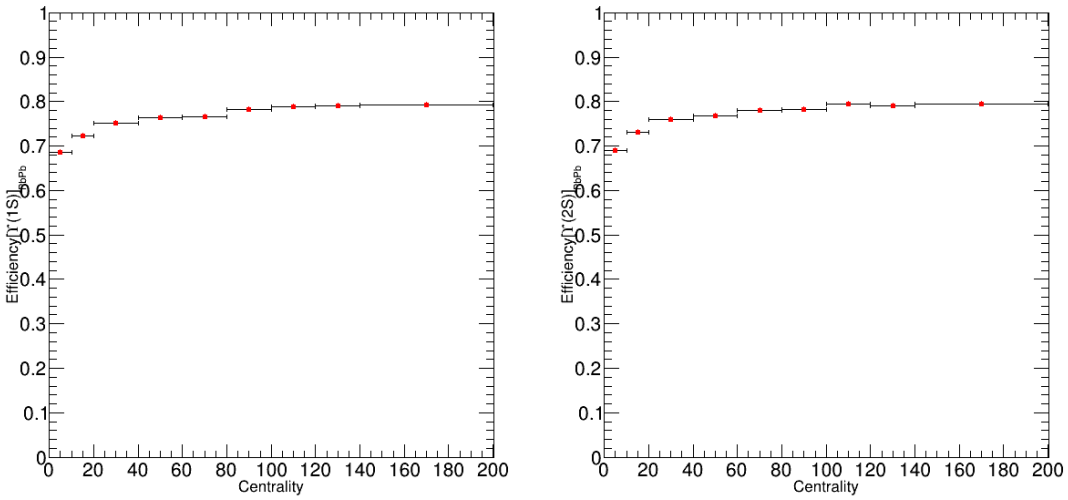

Figure 5.49: Efficiency of Υ(1S) (left) and Υ(2S) (right) as a function of centrality in Pb+Pb.

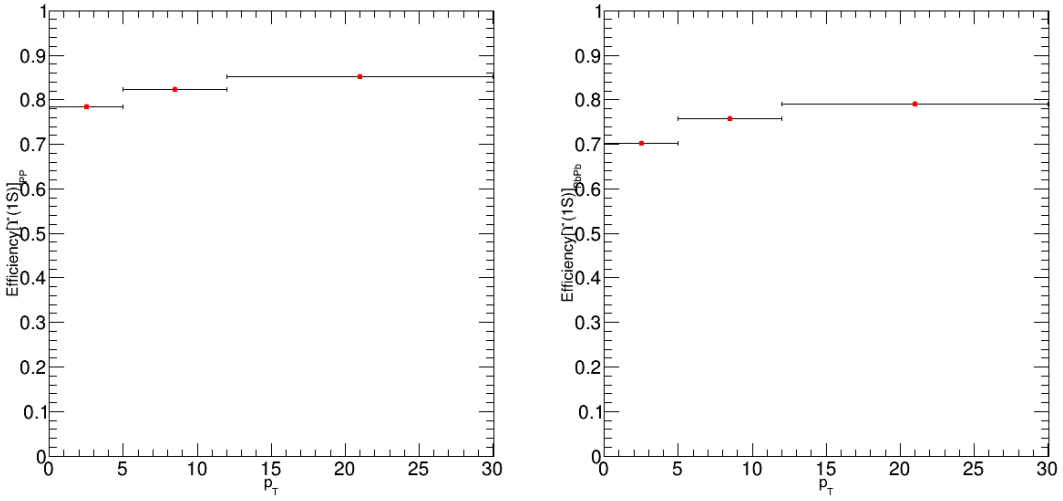

Figure 5.50: Efficiency of Υ(1S) as a function of p_T in $p+p$ (left) and Pb+Pb (right).

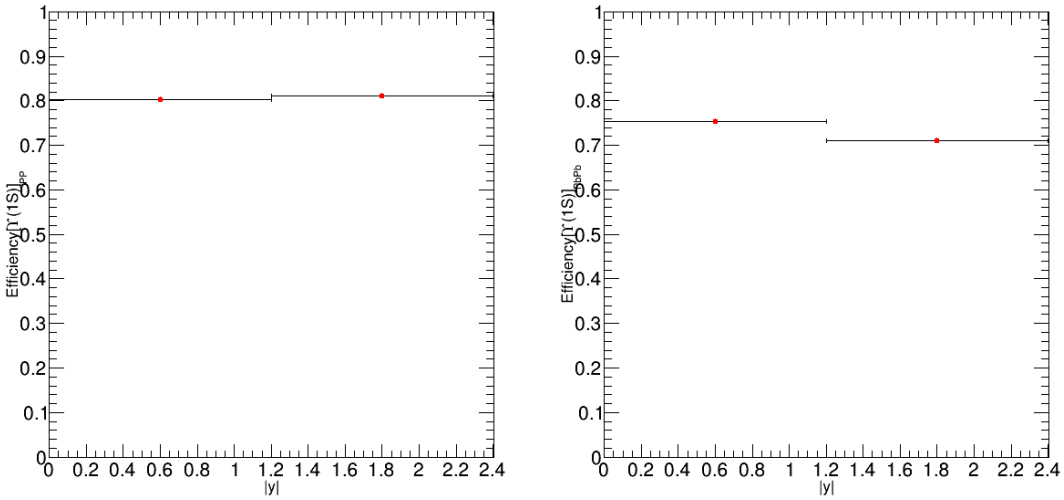

Figure 5.51: Efficiency of Υ(1S) as a function of $|y|$ in $p+p$ (left) and Pb+Pb (right).

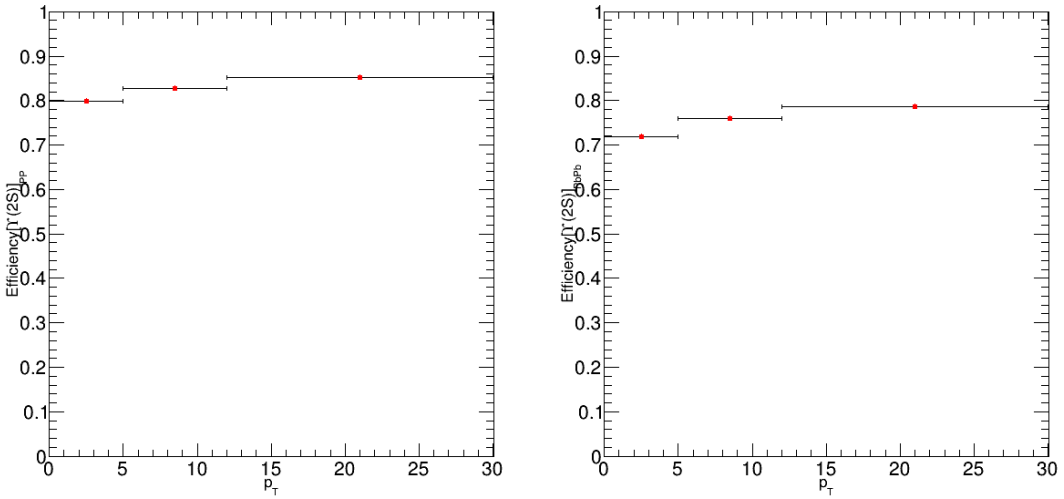

Figure 5.52: Efficiency of Υ(2S) as a function of p_T in $p+p$ (left) and Pb+Pb (right).

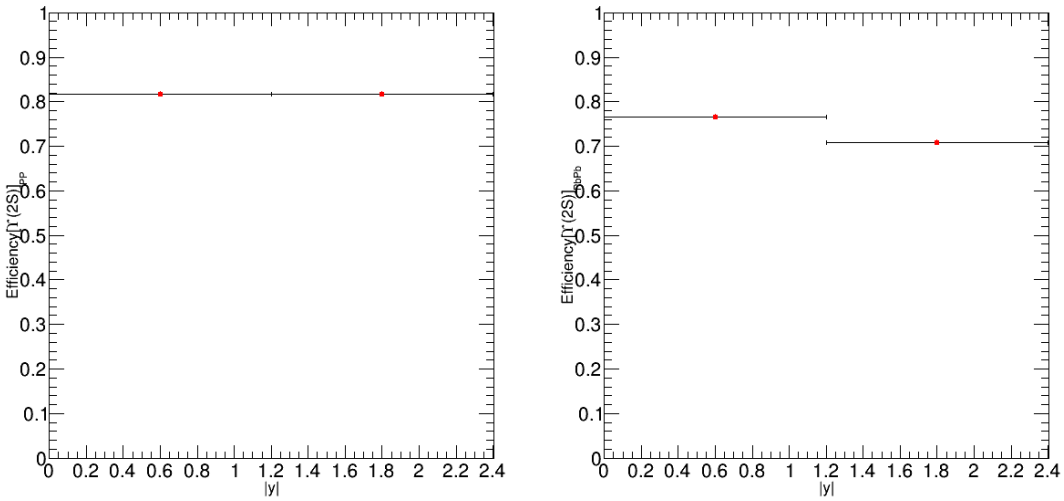

Figure 5.53: Efficiency of Υ(2S) as a function of $|y|$ in $p+p$ (left) and Pb+Pb (right).

Bin	pp (1S)			PbPb (1S)			pp (2S)			PbPb (2S)		
	Efficiency	Error		Efficiency	Error		Efficiency	Error		Efficiency	Error	
		+	-		+	-		+	-		+	-
$p_T < 5$ GeV/c	0.7836	0.0009	0.0009	0.7020	0.0030	0.0030	0.7991	0.0006	0.0006	0.7194	0.0031	0.0031
$5 < p_T < 12$ GeV/c	0.8234	0.0008	0.0009	0.7580	0.0024	0.0024	0.8277	0.0009	0.0009	0.7592	0.0030	0.0030
$12 < p_T < 30$ GeV/c	0.8510	0.0012	0.0012	0.7895	0.0019	0.0019	0.8513	0.0016	0.0016	0.7859	0.0025	0.0025
$\|y\| < 1.2$	0.8032	0.0007	0.0007	0.7536	0.0021	0.0021	0.8165	0.0007	0.0007	0.7655	0.0024	0.0024
$1.2 < \|y\| < 2.4$	0.8112	0.0009	0.0009	0.7098	0.0028	0.0028	0.8174	0.0008	0.0008	0.7082	0.0032	0.0032
p_T, y integrated	0.8064	0.0006	0.0006				0.8169	0.0005	0.0005			
$0-5\%$				0.6856	0.0047	0.0048				0.6904	0.0053	0.0053
$5-10\%$				0.7224	0.0047	0.0047				0.7302	0.0052	0.0053
$10-20\%$				0.7505	0.0032	0.0032				0.7589	0.0036	0.0036
$20-30\%$				0.7642	0.0032	0.0032				0.7684	0.0036	0.0036
$30-40\%$				0.7657	0.0032	0.0032				0.7796	0.0035	0.0035
$40-50\%$				0.7818	0.0031	0.0031				0.7826	0.0035	0.0035
$50-60\%$				0.7892	0.0030	0.0031				0.7940	0.0034	0.0034
$60-70\%$				0.7909	0.0030	0.0030				0.7899	0.0034	0.0034
$70-100\%$				0.7923	0.0021	0.0021				0.7941	0.0024	0.0024

Table 5.10: Efficiencies of $p+p$ Υ(1S), Pb+Pb Υ(1S), $p+p$ Υ(2S), Pb+Pb Υ(2S) in bins of p_T, $|y|$, integrated p_T and $|y|$, and centrality as appropriate.

The efficiency of the single ratio is defined as the efficiency of the Υ(2S) divided by the efficiency of the Υ(1S) or rather the efficiency of $\mathcal{R}_{21}$. Figure 5.54 shows the efficiency of the single ratio as a function of centrality in Pb+Pb. Figures 5.55 and 5.56 show the efficiency of the single ratio for $p+p$ and Pb+Pb as a function of dimuon p_T and $|y|$, respectively.

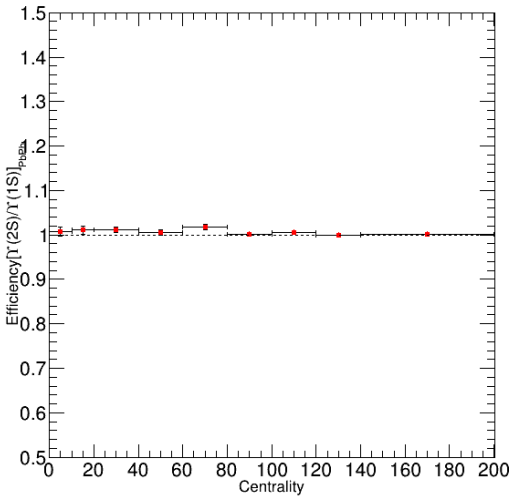

Figure 5.54: Single ratio of efficiencies as a function of centrality in Pb+Pb

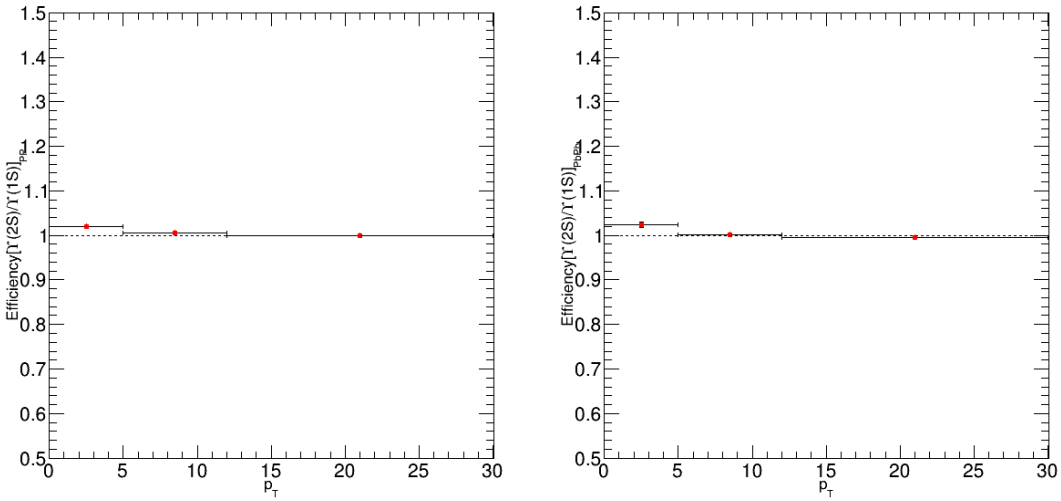

Figure 5.55: Efficiency of $\mathcal{R}_{21}$ single ratio as a function of p_T in $p+p$ (left) and Pb+Pb (right).

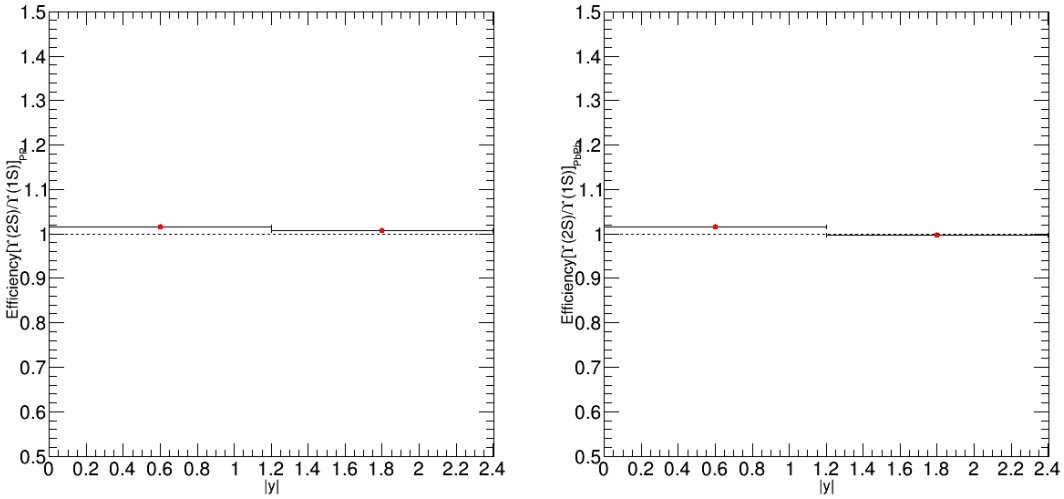

Figure 5.56: Efficiency of $\mathcal{R}_{21}$ single ratio as a function of $|y|$ in $p+p$ (left) and Pb+Pb (right).

Finally, the efficiency double ratio, namely the Pb+Pb efficiency of the single ratio divided by the $p+p$ efficiency of the single ratio, is obtained as a function of each of the quantities p_T, $|y|$ and centrality. The plots for the efficiency double ratios are shown in Figure 5.57. All the efficiency plots have error bars, which are not visible due to their small size. In Figure 5.58, we include plots for the double ratios using a smaller $y-$axis range, so that the error bars are visible.

Table 5.11 shows single ratio of efficiencies for $p+p$ and Pb+Pb and the efficiency double ratio in bins of p_T, $|y|$, Centrality, as well as the integrated bins.

Bin	Single Ratio (pp)			Single Ratio (PbPb)			Double Ratio		
	Value	Error		Value	Error		Value	Error	
		+	-		+	-		+	-
$p_T < 5$ GeV/c	1.0199	0.0014	0.0014	1.0249	0.0063	0.0063	1.0049	0.0063	0.0063
$5 < p_T < 12$ GeV/c	1.0052	0.0015	0.0015	1.0015	0.0051	0.0051	0.9963	0.0053	0.0053
$12 < p_T < 30$ GeV/c	1.0003	0.0023	0.0023	0.9954	0.0040	0.0040	0.9951	0.0046	0.0046
$\|y\| < 1.2$	1.0166	0.0012	0.0012	1.016	0.0043	0.0043	0.9991	0.0044	0.0044
$1.2 < \|y\| < 2.4$	1.0077	0.0015	0.0015	0.9977	0.0060	0.0060	0.9901	0.0061	0.0062
p_T, y integrated	1.0130	0.0009	0.0009						
$0 - 5\%$				1.0070	0.0104	0.0104	0.9941	0.0103	0.0103
$5 - 10\%$				1.0108	0.0098	0.0098	0.9978	0.0097	0.0097
$10 - 20\%$				1.0112	0.0065	0.0065	0.9982	0.0064	0.0065
$20 - 30\%$				1.005	0.0063	0.0063	0.9925	0.0063	0.0063
$30 - 40\%$				1.0181	0.0062	0.0062	1.0050	0.0062	0.0062
$40 - 50\%$				1.0010	0.0060	0.0060	0.9881	0.0060	0.0060
$50 - 60\%$				1.0061	0.0058	0.0058	0.9931	0.0058	0.0058
$60 - 70\%$				0.9988	0.0057	0.0057	0.9859	0.0057	0.0057
$70 - 100\%$				1.0022	0.0041	0.0041	0.9893	0.0041	0.0041
Centrality integrated				1.0089	0.0035	0.0035	0.9960	0.0036	0.0036

Table 5.11: Efficiency single (Υ(2S)to Υ(1S)) and the double ratios in bins of p_T, $|y|$, integrated p_T and $|y|$, centrality and integrated centrality as appropriate.

The three efficiency double ratio plots show values in every bin consistent with 1, with the largest deviation 1.4% away from unity. We conclude that efficiency corrections are not needed. We do not correct our raw yield or ratios by these efficiencies but rather quote a systematic uncertainty due to possible non cancellation of the efficiencies, with the size of the uncertainty taken as the percent deviation from unity as in Table 5.13.

For the Υ(3S), we determine only the centrality dependence of the Pb+Pb efficiency, and define the efficiency single and double ratios analogous to the case of Υ(2S). Figure 5.59, shows the Υ(3S) efficiency and the single ratio of efficiencies applied to $\mathcal{R}_{31}$ in Pb+Pb. The efficiency double ratio for Υ(3S) is shown in Figure 5.60. Table 5.12 contains the values for all the efficiencies regarding the Υ(3S).

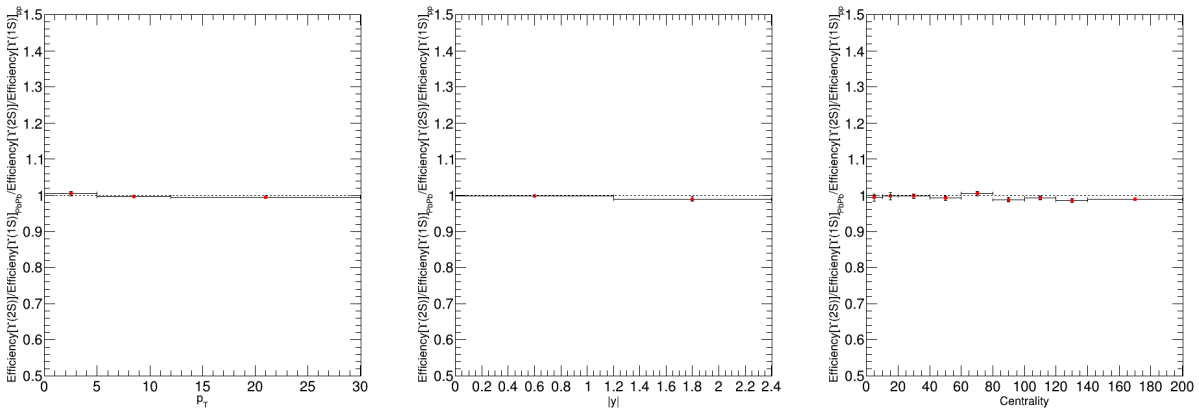

Figure 5.57: Efficiency double ratios, $\mathcal{R}_{21}$ in Pb+Pb vs. $p+p$ as a function of dimuon p_T (left), $|y|$ (middle) and centrality (right).

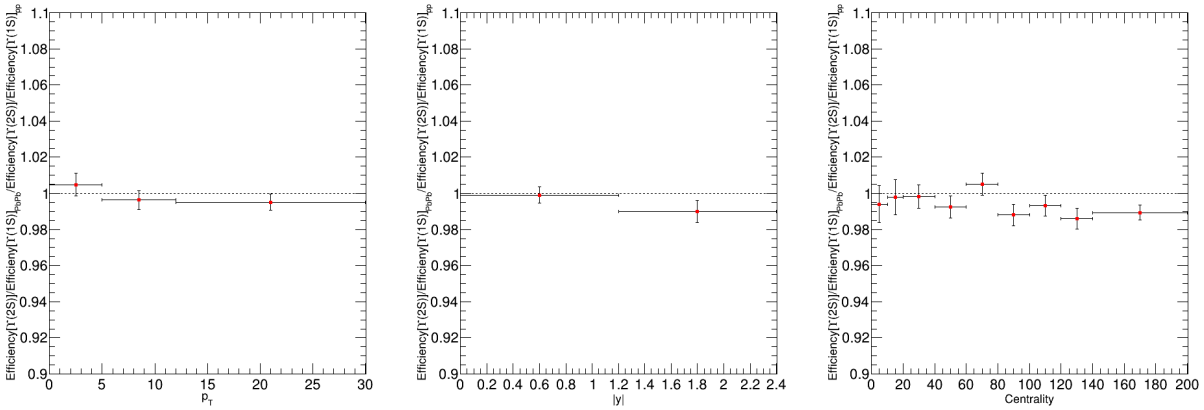

Figure 5.58: Efficiency double ratios, $\mathcal{R}_{21}$ in Pb+Pbvs. $p+p$ as a function of dimuon p_T (left), $|y|$ (middle), and centrality (right). The data shown are the same as in Fig. 5.57, but zoomed in.

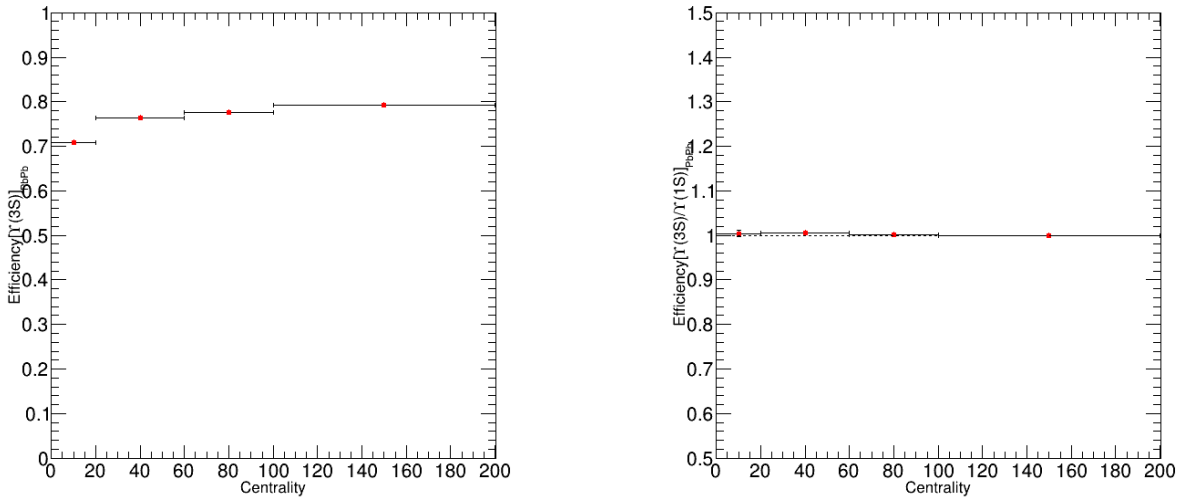

Figure 5.59: Efficiency of Υ(3S) (left) and single ratio of Υ(3S) to Υ(1S) efficiency in Pb+Pb as functions of centrality.

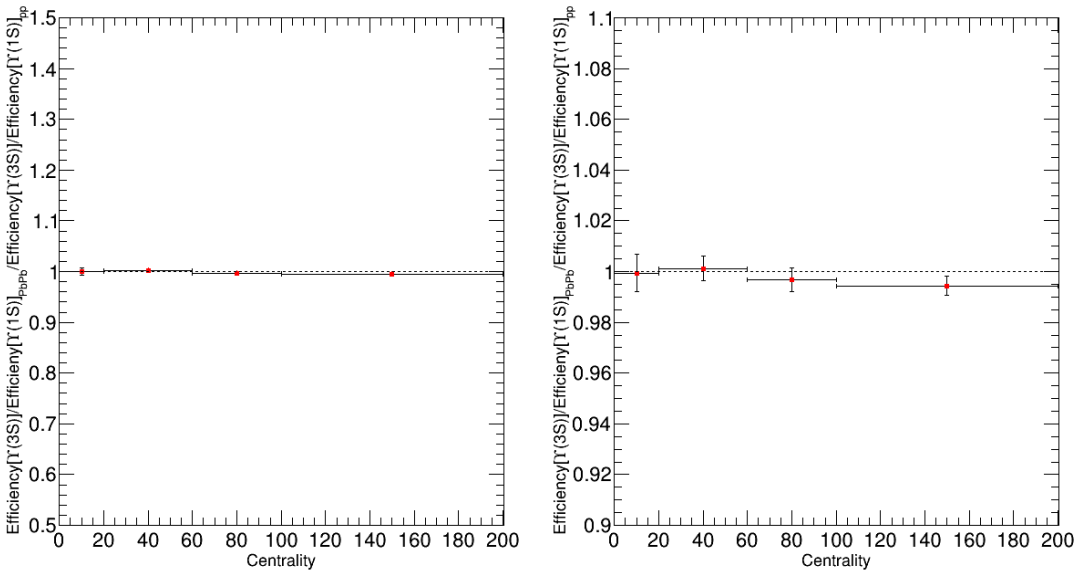

Figure 5.60: Efficiency of double ratio, $\mathcal{R}_{31}$ in $p+p$ vs. Pb+Pb as a function of centrality (left) and the same data is shown zoomed in(right).

Bin	PbPb (3S)			Single Ratio (PbPb)			Double Ratio		
	Efficiency	Error		Value	Error		Value	Error	
		+	-		+	-		+	-
$0-10\%$	0.7080	0.0040	0.0040	1.0040	0.0073	0.0073	0.9995	0.0073	0.0073
$10-30\%$	0.7630	0.0027	0.0028	1.0058	0.0047	0.0047	1.0013	0.0047	0.0047
$30-50\%$	0.7758	0.0027	0.0027	1.0014	0.0045	0.0046	0.9968	0.0046	0.0046
$50-100\%$	0.7872	0.0023	0.0023	0.9988	0.0037	0.0037	0.9951	0.0038	0.0038
Centrality integrated				1.0045	0.0035	0.0035	1.0000	0.0036	0.0036

Table 5.12: Pb+Pb Υ(3S) efficiency, and the Υ(3S) efficiency single and double ratios in bins of centrality and integrated centrality.

5.3 Systematics

5.3.1 Efficiency Uncertainty

The systematic deviation of the acceptance ratio is not corrected for nor is it a systematic uncertainty as noted in Sec. 5.2. The systematic deviations of the efficiency double ratio are shown in Table 5.13. The reported systematic uncertainty is the percent deviation of the efficiency double ratio from 1. For instance, if the efficiency double ratio is 0.95 then the systematic uncertainty is $1-0.95 = 5\%$. Though we present the bin by bin percentage systematic uncertainty by efficiency variance, for the analysis we use 1.4% across all bins, as a conservative estimate, as this is the largest deviation.

Bin	DR21 Efficiency	Systematic Uncertainty (%)
$p_T < 5$ GeV/c	1.0049	0.49
$5 < p_T < 12$ GeV/c	0.9963	0.37
$12 < p_T < 30$ GeV/c	0.9951	0.49
$\|y\| < 1.2$	0.9991	0.09
$1.2 < \|y\| < 2.4$	0.9901	0.99
0-5%	0.9941	0.59
5-10%	0.9978	0.22
10-20%	0.9982	0.18
20-30%	0.9925	0.75
30-40%	1.0050	0.50
40-50%	0.9881	1.19
50-60%	0.9931	0.69
60-70%	0.9859	1.41
70-100%	0.9893	1.07
Centrality integrated	0.9960	0.40

Table 5.13: Systematic deviations of double ratio efficiency given as percentages of the double ratio.

5.3.2 Fitting uncertainties

This section details the studies involved with systematics that arise from choosing a nominal fit model as described in Section 5.1. The systematics are all calculated by comparing the nominal fit results detailed in Section 5.1.4 with an alternative method. The fit uncertainty is computed as the quadratic sum of six sources: releasing signal parameter constraints one by one, changing the signal PDF to a sum of a Crystal Ball plus Gaussian, variation in background by allowing the width parameter to float freely, and using 4th-order polynomial function as an alternative background in a toy pseudo experiment. The variations on the signal $\mathcal{S}$ and background $\mathcal{B}$ are described below and were performed independently for each analysis bin.

5.3.2.1 Uncertainty from signal parameters

The 5 signal PDF parameters $(n, \alpha, \sigma_0, f, x)$ which were fixed by fitting the MC simulation Υ signal (see Section 5.1.1) are released one-by-one in the fit to the data (the other 4 being fixed to their constrained value), leading to 5 fits per bin. Since all signal parameters are obtained independently from the MC for $p+p$ and Pb+Pb in each kinematic range, the total systematic uncertainty is taken to be the quadratic sum of the uncertainties in $p+p$ and Pb+Pb in each bin. The uncertainty in each bin for both collision systems is regarded as the Root Mean Square (RMS) of the single ratio of Υ(2S)/Υ(1S) for the five variations to the nominal fit in a given bin. In Fig. 5.61 and Fig. 5.62, the fit variations of certain bins are reported and the results of the systematic uncertainty due to possible variations in the signal parameters are summarized in Table 5.14 and Table 5.15.

This same procedure was explored for the Υ(3S) and the results are reported in Table 5.16 and Table 5.17.

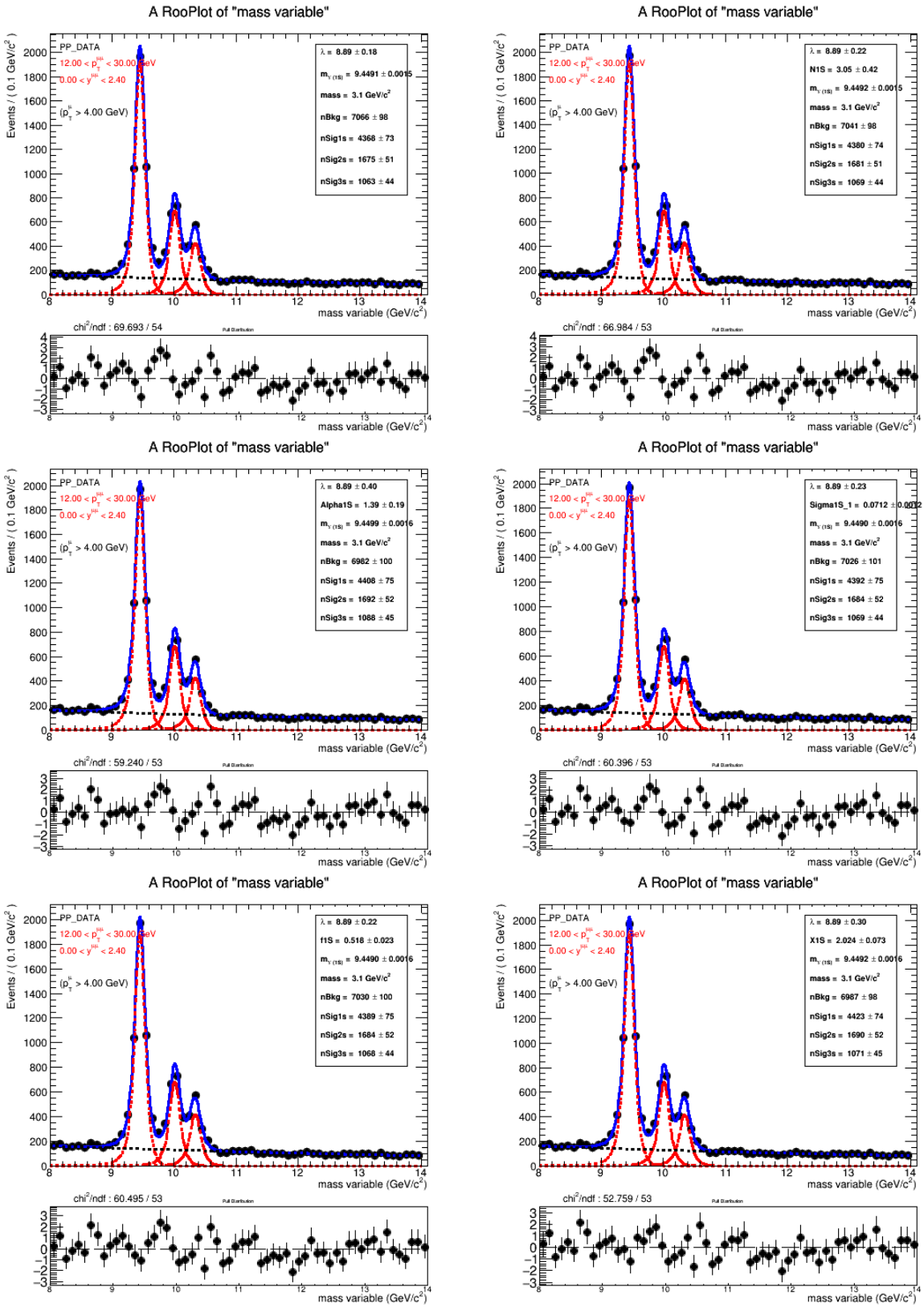

Figure 5.61: Fit variations of the highest p_T bin in $p+p$ data.

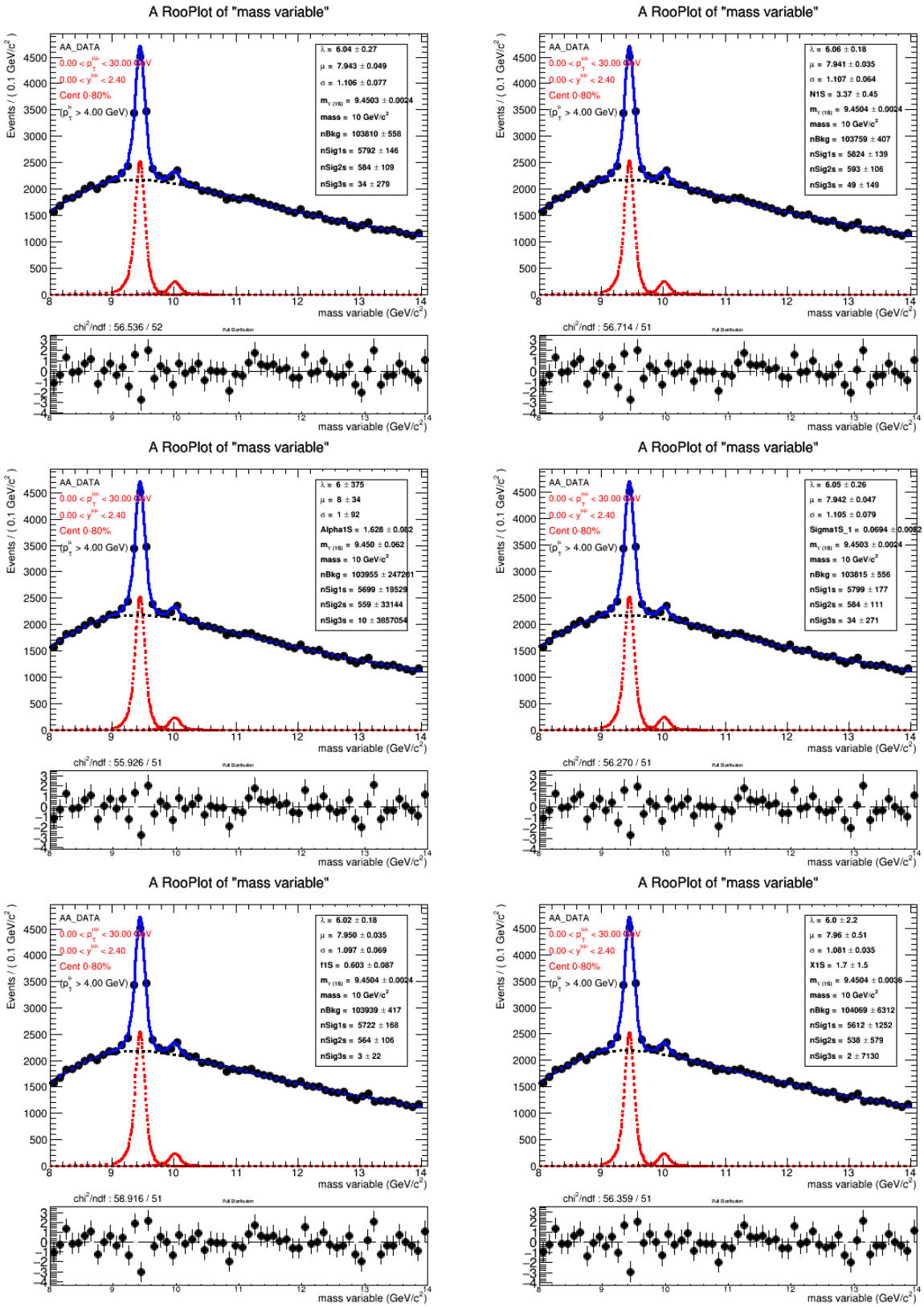

Figure 5.62: Fit variations of the centrality-integrated Pb+Pb data

pp (2S/1S) Bin	n	α	σ	f	x	RMS
integrated	0.375	0.454	0.383	0.477	0.168	0.375
$p_T < 5$ GeV/c	0.400	0.137	0.209	0.158	0.724	0.393
$5 < p_T < 12$ GeV/c	0.299	0.340	0.077	0.187	0.305	0.260
$12 < p_T < 30$ GeV/c	0.226	0.174	0.030	0.062	0.406	0.224
$\|y\| < 1.2$ GeV/c	0.865	0.004	0.639	0.754	0.720	0.670
$1.2 < \|y\| < 2.4$ GeV/c	0.540	0.001	0.030	0.042	0.031	0.243
PbPb (2S/1S) Bin	n	α	σ	f	x	RMS
0 - 100%	1.285	3.312	0.032	1.139	3.273	2.219
0 - 5%	4.629	8.866	5.450	6.708	8.144	6.943
5 - 10%	0.351	3.637	5.860	5.624	1.669	4.052
10 - 20%	1.173	3.078	2.650	6.370	3.822	3.823
20 - 30%	1.008	1.860	0.479	1.103	1.161	1.206
30 - 40%	1.269	1.542	4.218	4.102	3.673	3.228
40 - 50%	2.554	1.893	3.168	3.227	2.239	2.667
50 - 60%	0.320	1.996	0.380	0.215	1.648	1.183
60 - 70%	0.663	2.140	0.114	0.0001	0.037	1.003
70 - 100%	0.682	1.804	4.023	3.765	2.164	2.784
$p_T < 5$ GeV/c	1.198	6.593	1.736	1.334	2.725	3.380
$5 < p_T < 12$ GeV/c	0.525	2.210	1.155	0.514	0.131	1.164
$12 < p_T < 30$ GeV/c	0.450	1.894	0.722	0.407	0.536	0.976
$\|y\| < 1.2$	2.852	0.636	3.009	2.911	0.643	2.314
$1.2 < \|y\| < 2.4$	1.212	2.723	5.608	4.308	0.232	3.434

Table 5.14: Systematic deviations of the single ratio (2S/1S) in units of percentage when varying the signal PDF parameters in each of the analysis bins. The $p + p$ results are the first six rows and the Pb+Pb are the ones below those.

Bin	Total Param. Release Uncertainty
Integrated pp	0.375
MB PbPb 0 - 100%	2.219
0 - 5%	6.943
5 - 10%	4.052
10 - 20%	3.823
20 - 30%	1.206
30 - 40%	3.228
40 - 50%	2.667
50 - 60%	1.183
60 - 70%	1.003
70 - 100%	2.784
$p_T < 5$ GeV/c	3.403
$5 < p_T < 12$ GeV/c	1.193
$12 < p_T < 30$ GeV/c	1.002
$\|y\| < 1.2$	2.409
$1.2 < \|y\| < 2.4$	3.442

Table 5.15: Total systematic deviations of the double ratio (2S/1S) in units of percentage by the variance of the signal PDF parameters

Table 5.16: Systematic deviations of the single ratio (3S/1S) in units of percentage when varying the signal PDF parameters in $p+p$ (top row) and Pb+Pb (bottom five rows).

pp	n	α	σ	f	x	RMS
integrated	0.877	1.930	0.716	0.739	0.235	1.059
PbPb (3S/1S) Bin	n	α	σ	f	x	RMS
0 - 100%	12.565	32.263	0.771	11.101	36.039	22.897
0 - 10%	2.389	4.883	11.858	11.336	9.432	8.805
10 - 30%	1.4×10^4	99.351	2.2×10^3	3.4×10^7	2.5×10^3	1.5×10^7
30 - 50%	2.678	26.586	6.787	8.597	7.235	13.314
50 - 100%	2.218	6.706	9.157	12.157	6.737	8.081

Table 5.17: Total systematic deviations of the double ratio (3S/1S) in units of percentage by the variance of the signal PDF parameters

Bin	Total Signal Uncertainty
Integrated pp	1.059
MB PbPb 0 - 100%	22.897
0 - 10%	8.805
10 - 30%	1.5×10^7
30 - 50%	13.314
50 - 100%	8.081

5.3.2.2 Uncertainty from Signal PDF Change (CB + Gaussian)

The nominal signal PDF defined in Section 5.1 was altered from a double Crystal Ball to a Crystal Ball plus Gaussian. These two options were studied first in MC as described in Section 5.1.1 where it was determined that the double Crystal Ball was the better nominal signal PDF while the Crystal Ball plus Gaussian was also a fair choice. Since the Crystal Ball plus Gaussian was a possible choice we decided to study it for the systematic uncertainty. Below are the results of fitting the data with this alternative signal PDF as well as the percent deviation of the single and double ratios from the nominal fits.

Bin	R21 Uncertainty (%)		DR21 Uncertainty (%)
	pp	PbPb	
p_T, y integrated	0.97	1.84	0.86
$p_T < 5$ GeV/c	1.81	0.51	2.4
$5 < p_T < 12$ GeV/c	1.72	3.68	1.93
$12 < p_T < 30$ GeV/c	1.76	2.37	0.60
$\|y\| < 1.2$	0.64	0.86	0.22
$1.2 < \|y\| < 2.4$	0.34	4.83	4.48
0-5%		4.48	3.48
5-10%		1.28	0.31
10-20%		2.22	1.24
20-30%		1.79	0.81
30-40%	0.97	1.70	0.73
40-50%		1.60	0.60
50-60%		2.05	1.07
60-70%		1.87	0.89
70-100%		2.14	1.6

Table 5.18: Systematic deviations in units of percent for the single and double ratios of Υ(2S) to Υ(1S) due to signal PDF change to Crystal Ball plus Gaussian.

Bin	R31 Uncertainty (%)		DR31 Uncertainty (%)
	pp	PbPb	
p_T, y integrated	1.36	7.86	6.42
0-10%	-	1.20	0.16
10-30%	-	1111	1095
30-50%	-	2.40	1.02
50-80%	-	2.39	2.60

Table 5.19: Systematic deviations in units of percent for the single and double ratios of Υ(3S) to Υ(1S) due to signal PDF change to Crystal Ball plus Gaussian.

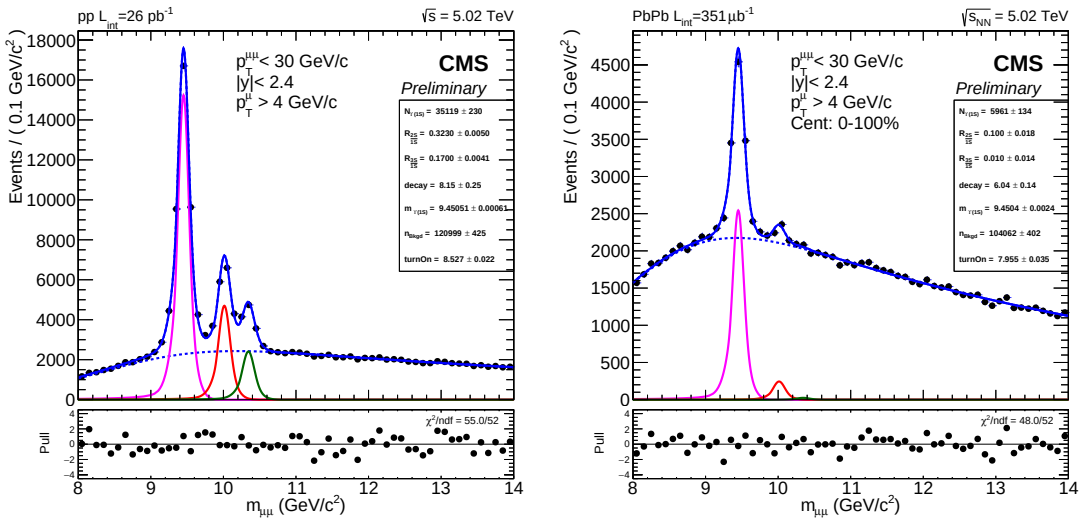

Figure 5.63: Fit to the $p+p$ (left) and Pb+Pb (right) invariant mass distributions using a Crystal Ball plus Gaussian function, where the data are integrated over p_T and y, and for the case of Pb+Pb also over all the centrality bins used in the analysis.

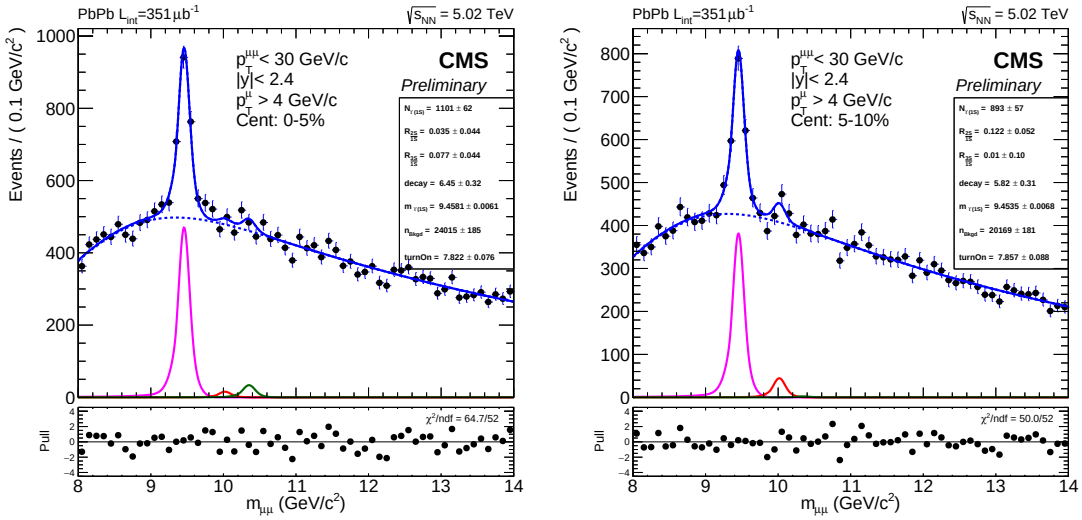

Figure 5.64: Crystal Ball plus Gaussian Fits to Pb+Pb dimuon mass data, for Centrality bins [0-5]% (left) and [5-10]% (right).

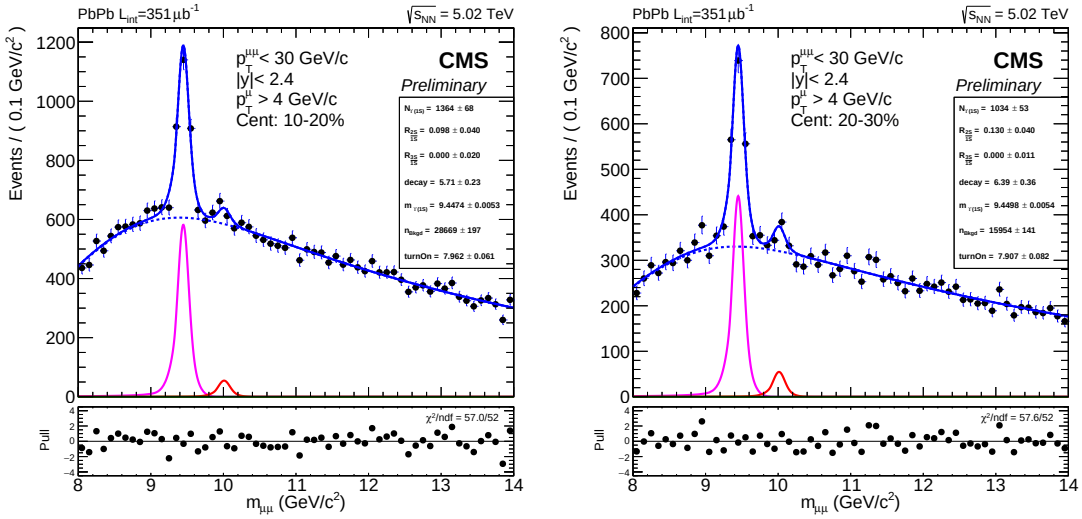

Figure 5.65: Crystal Ball plus Gaussian Fits to Pb+Pb dimuon mass data, for Centrality bins [10-20]% (left) and [20-30]% (right).

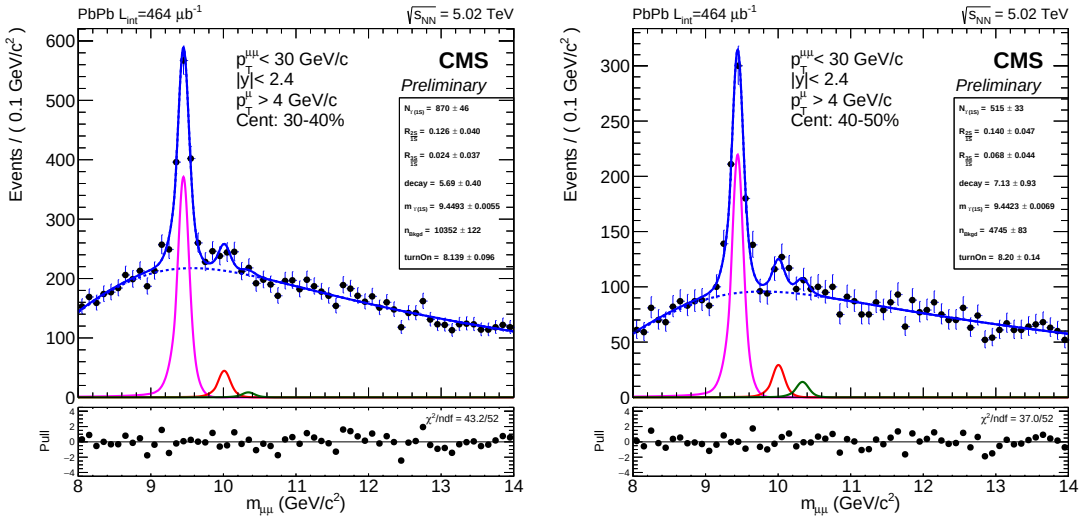

Figure 5.66: Crystal Ball plus Gaussian Fits to Pb+Pb dimuon mass data, for Centrality bins [30-40]% (left) and [40-50]% (right).

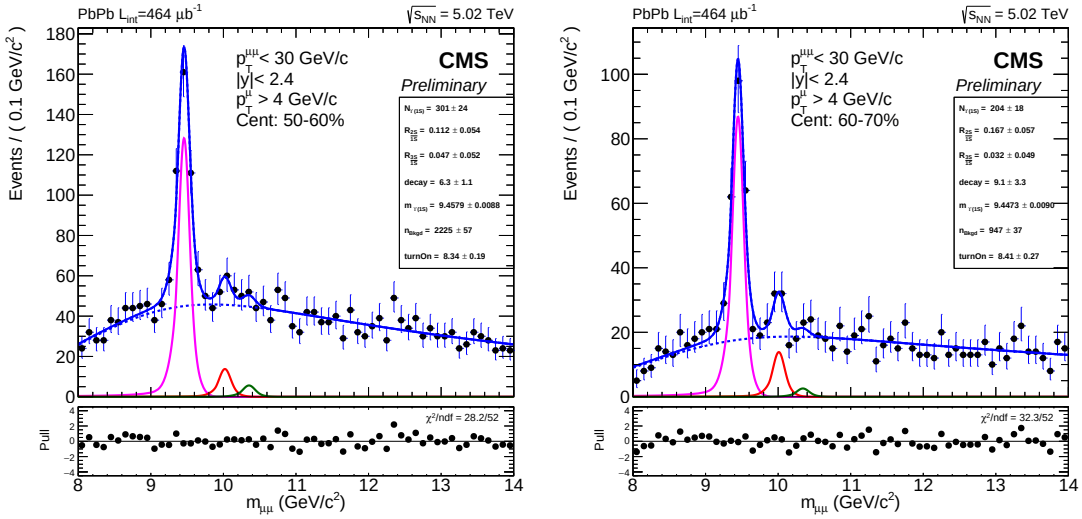

Figure 5.67: Crystal Ball plus Gaussian Fits to Pb+Pb dimuon mass data, for Centrality bins [50-60]% (left) and [60-70]% (right).

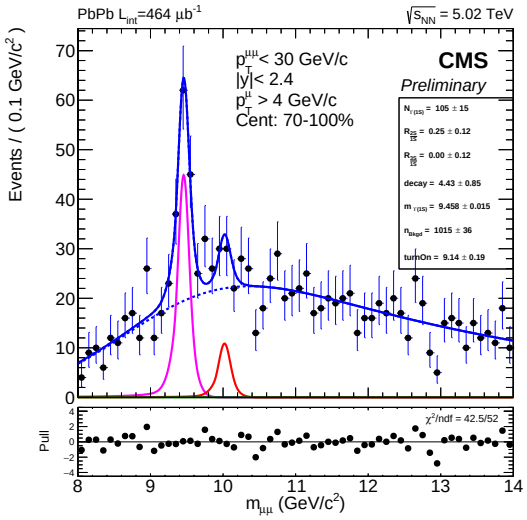

Figure 5.68: Crystal Ball plus Gaussian Fit to Pb+Pb dimuon mass data for the most peripheral bin [70-100]%

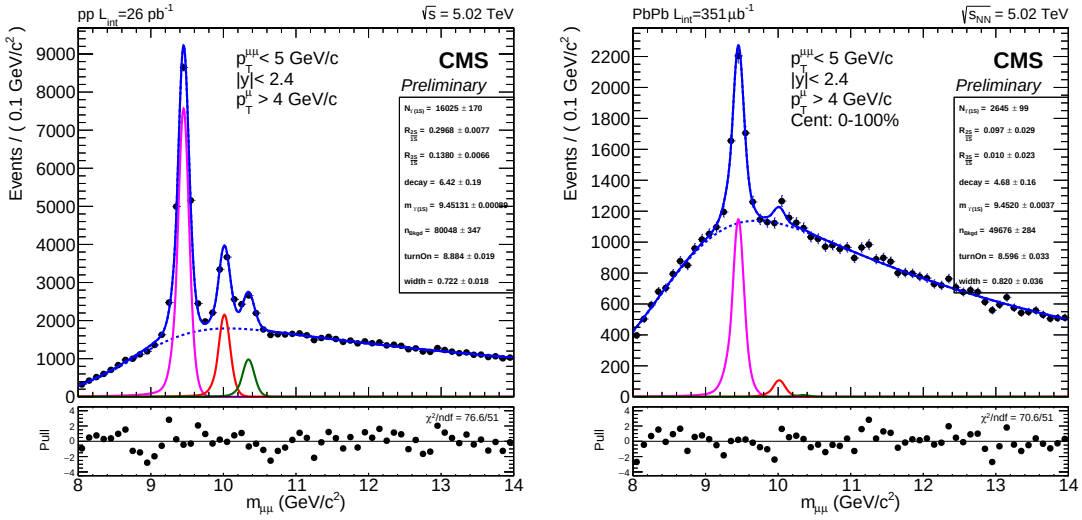

Figure 5.69: Crystal Ball plus Gaussian Fit to $p+p$ (left) and Pb+Pb (right) for p_T [GeV/c] $\in$ [0-5.0].

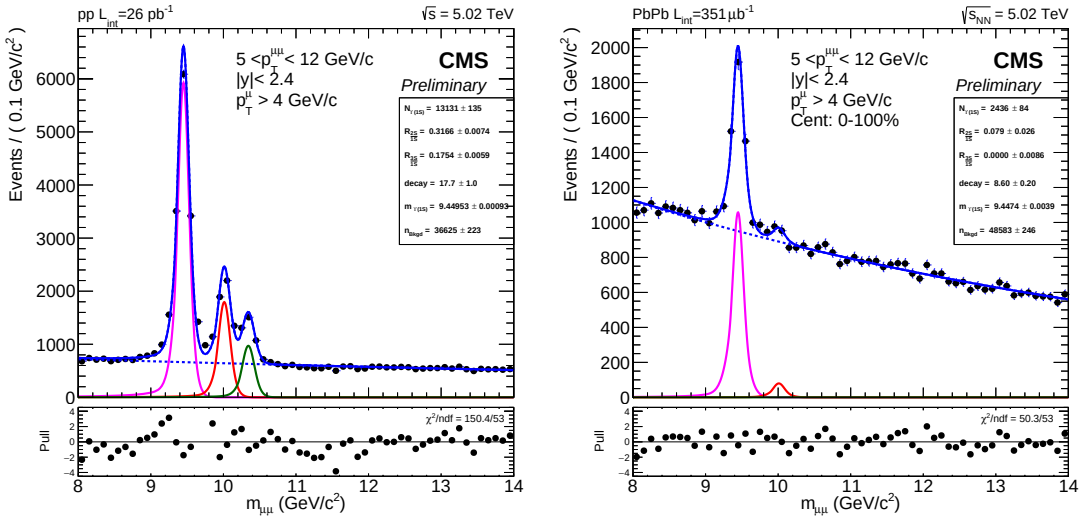

Figure 5.70: Crystal Ball plus Gaussian Fit to $p+p$ (left) and Pb+Pb (right) for p_T [GeV/c] $\in$ [5.0-12.0].

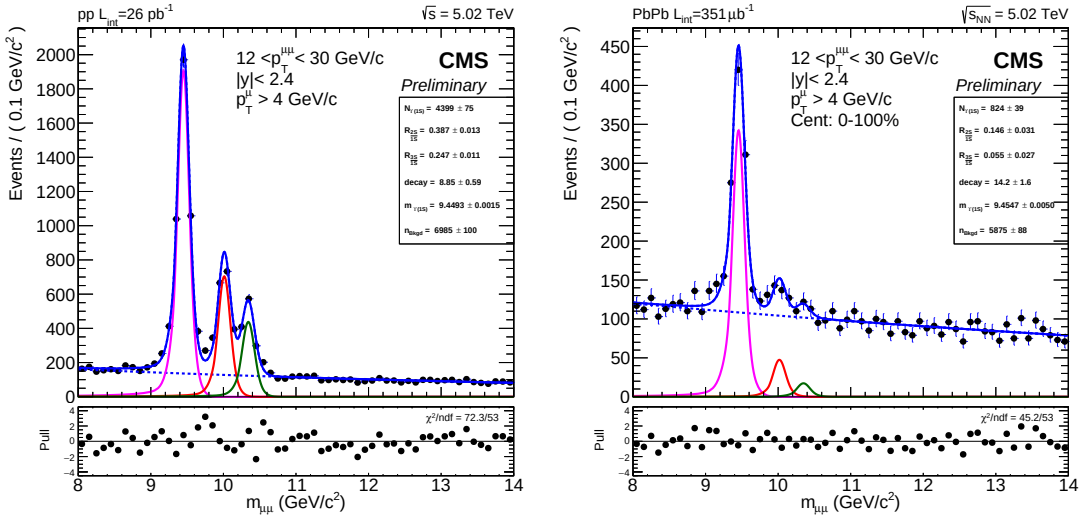

Figure 5.71: Crystal Ball plus Gaussian Fit to $p+p$ (left) and Pb+Pb (right) for p_T [GeV/c] $\in$ [12.0-30.0].

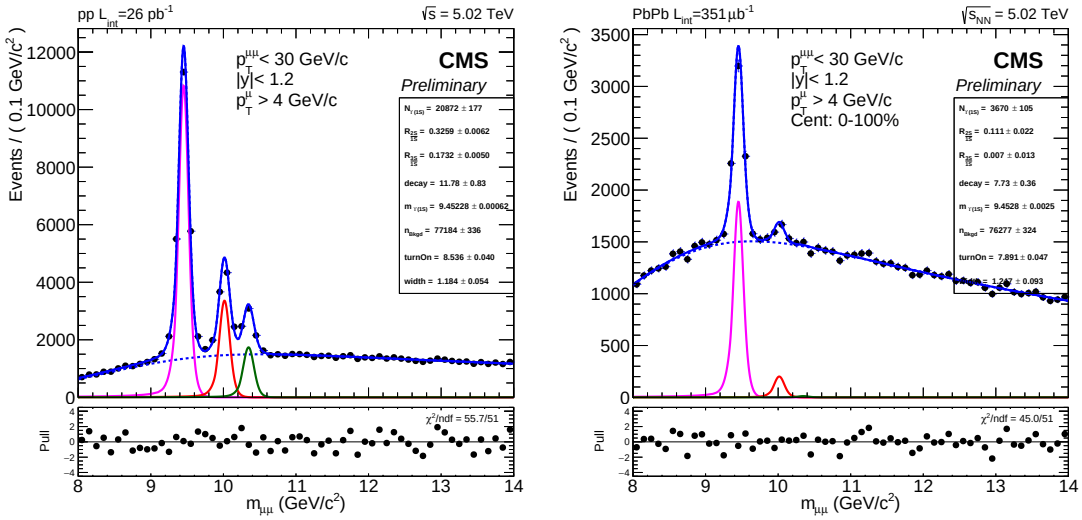

Figure 5.72: Crystal Ball plus Gaussian Fit to $p+p$ (left) and Pb+Pb (right) for $|y^{\mu\mu}| \in$ [0-1.2].

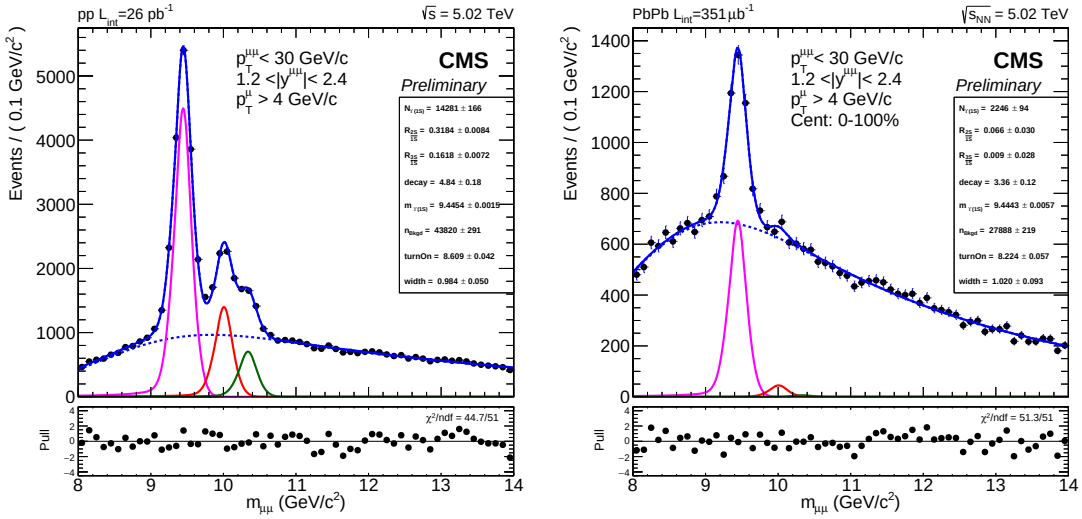

Figure 5.73: Crystal Ball plus Gaussian Fit to $p+p$ (left) and Pb+Pb (right) for $|y^{\mu\mu}| \in$ [1.2-2.4].

5.3.2.3 Uncertainty from Background model PDF

The nominal Background PDF $\mathcal{B}$, defined in Eq. 5.7, was used in every bin for the analysis except for the two highest p_T bins. A systematic uncertainty occurs because, as noted earlier the background shape includes many contributions, and therefore it might not be completely captured by the PDF in Eq. 5.7. This is abundantly clear in the p_T, y, and centrality-integrated bin where the background is made of contributions from regions where the background turn-on shape depends on details of narrow kinematic regions. The uncertainties in each bin are estimated using a toy MC procedure, where we fit the data with both the nominal and an alternative background PDF model, and then evaluate the deviation of the double ratio from the nominal results.

The alternative background PDF used to study this is a 4th-order polynomial function. This PDF model is utilized because it has a similar goodness-of-fit as the $\mathcal{B}$ model but with a lack of physical motivation for its shape. The 4th order polynomial is the minimum number of parameters for a polynomial needed to describe the drastic curvatures in the background shapes in the lowest p_T bin. This study was first done by re-fitting the invariant mass spectra data using the 4th-order polynomial and the results for this are tabulated in Table 5.20 where the deviation from the nominal and alternative are given as a percent deviation for the single ratios in $p+p$ and Pb+Pb as well as the double ratio. The largest deviation seen is in the lowest p_T bin of 38%.

In a second study, to reduce any possible statistical fluctuation that could result in systematic effects, toy MC data sets were generated. The toy MC samples imitate the real data as much as possible by combining the Υ peaks and the background spectra by the ratios obtained in Sec. 5.1.4. The signal PDF is fixed by the the nominal PDF shape obtained from the nominal fit results in each bin detailed in Section 5.1.4. We generate 100K events in each p_T, rapidity, and centrality bin. This pseudo data are then fit using the alternative PDF which consists of the 4th-order polynomial function for the background model and the nominal signal model described in Section 5.1. The deviations of the single and double ratio values in $p+p$ and Pb+Pb are tabulated in Table 5.21. These deviations in the double ratio are taken as systematic uncertainties. Invariant mass

	Dev. in single ratio		Deviation in double ratio
	pp	PbPb	
Integrated	0.81	0.95	0.13
$p_T < 5$ GeV/c	6.70	35.10	26.62
$5 < p_T < 12$ GeV/c	0.10	21.69	21.61
$12 < p_T < 30$ GeV/c	0.39	8.53	8.17
$\|y\| < 1.2$	1.08	3.62	2.51
$1.2 < \|y\| < 2.4$	2.43	12.52	9.84
0-5%	0.81	37.36	37.86
5-10%		1.35	0.53
10-20%		2.09	1.27
20-30%		2.86	2.03
30-40%		5.75	4.90
40-50%		3.91	3.08
50-60%		11.12	10.22
60-70%		9.15	9.88
70-100%		4.43	3.58

Table 5.20: Υ(2S) to Υ(1S) systematic deviations of double ratio variance by alternative fit to data of background PDF as a percent.

	Dev. in single ratio		Deviation in double ratio
	pp	PbPb	
Integrated	2.05	4.65	2.56
$p_T < 5$ GeV/c	9.78	52.02	38.48
$5 < p_T < 12$ GeV/c	0.46	12.52	13.04
$12 < p_T < 30$ GeV/c	0.27	2.33	2.61
$\|y\| < 1.2$	1.45	4.38	2.89
$1.2 < \|y\| < 2.4$	2.38	5.84	3.37
0-5%	2.05	26.53	29.16
5-10%		5.09	6.99
10-20%		5.65	3.54
20-30%		2.86	0.81
30-40%		5.24	3.13
40-50%		5.54	3.43
50-60%		8.28	6.12
60-70%		4.45	2.36
70-100%		14.93	12.63

Table 5.21: Υ(2S) to Υ(1S) Systematic deviations of double ratio obtained by finding the average difference in the relevant ratio when fitting pseudo-data with the nominal background PDF compared to the alternative background PDF, as a percent.

distributions of toy MC data sets and fitting plots can be found in Fig. 5.74 for $p + p$ and in Fig. 5.76 for PbPb.

In Table 5.21 the 20-30% centrality bin has a systematic deviation that is smaller by a factor of around 2 than the neighboring bins 10-20 and 30-40. In order to account for any possible underestimation, a weighted average of all 3 bins is taken as the background systematic for the 20-30 bin. This average produces a systematic uncertainty of 4.04% for the 20-30 bin. This is reflected in the summary table for systematics.

The weighted average is:

$$< x >= \frac{w_{10-20} * x_{10-20} + w_{20-30} * x_{20-30} + w_{30-40} * x_{30-40}}{w_{10-20} + w_{20-30} + w_{30-40}} \tag{5.10}$$

Where x_i is the systematic in that i-th bin and w_i is the weight in the i-th bin. The weight is determined from the background parameters of the background PDF decay (λ) and location of kinematic turn on (μ).

$$w_i = [(\frac{\sigma_\mu}{\mu})^2 + (\frac{\sigma_\lambda}{\lambda})^2]_i^{-1} \tag{5.11}$$

Table 5.22: Background parameters used for weighting the systematic uncertainty bin.

Cent %	$\mu \pm \sigma_\mu$	$\lambda \pm \sigma_\lambda$
10-20	7.96 ± 0.061	5.73 ± 0.226
20-30	7.90 ± 0.016	6.40 ± 0.133
30-40	8.12 ± 0.095	5.72 ± 0.400

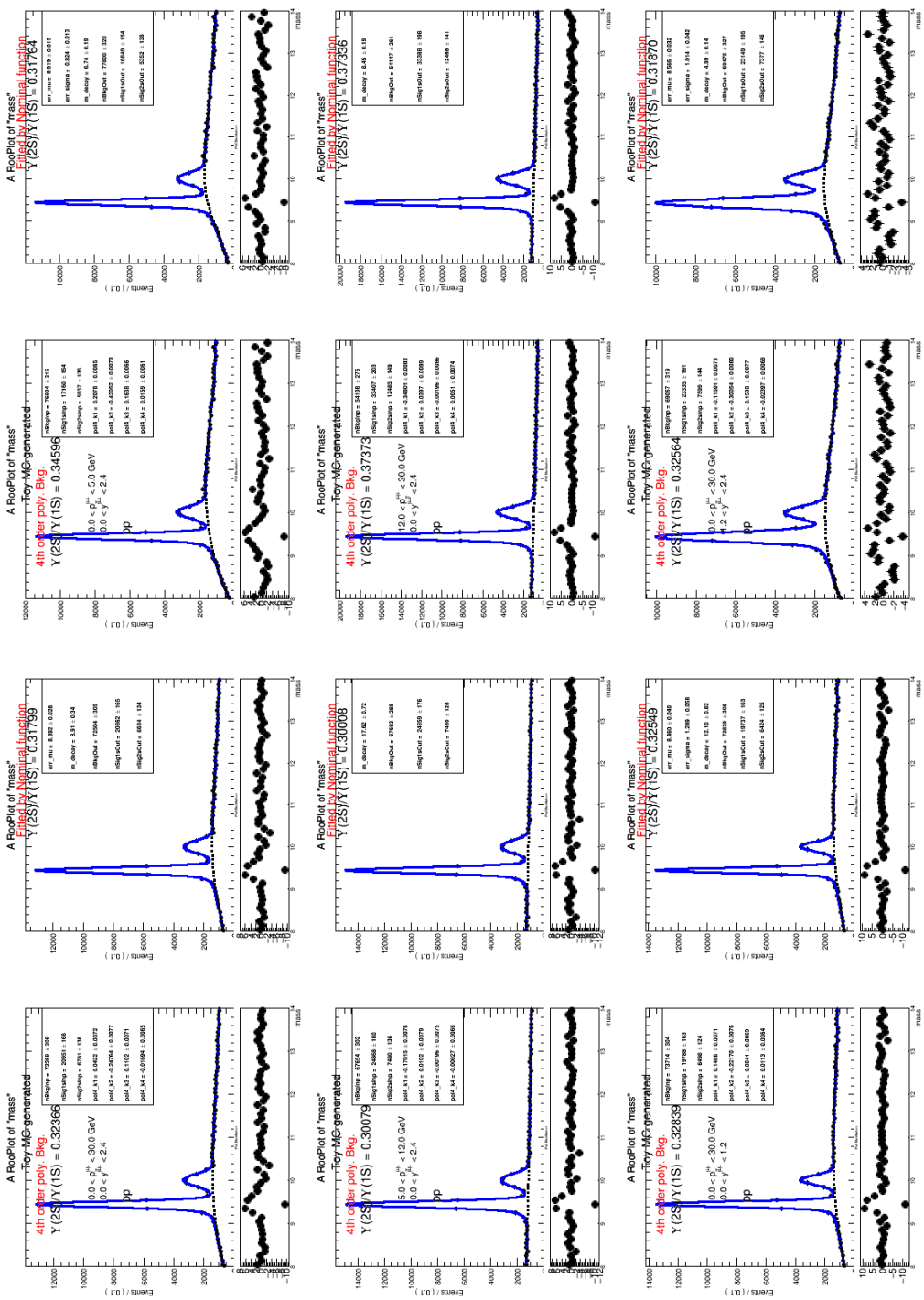

Figure 5.74: Fit variations using Toy MC study in $p+p$ data generated with nominal PDF and subsequently fit by 4th order poly PDF (left) and generated and fit with the nominal PDF (right)

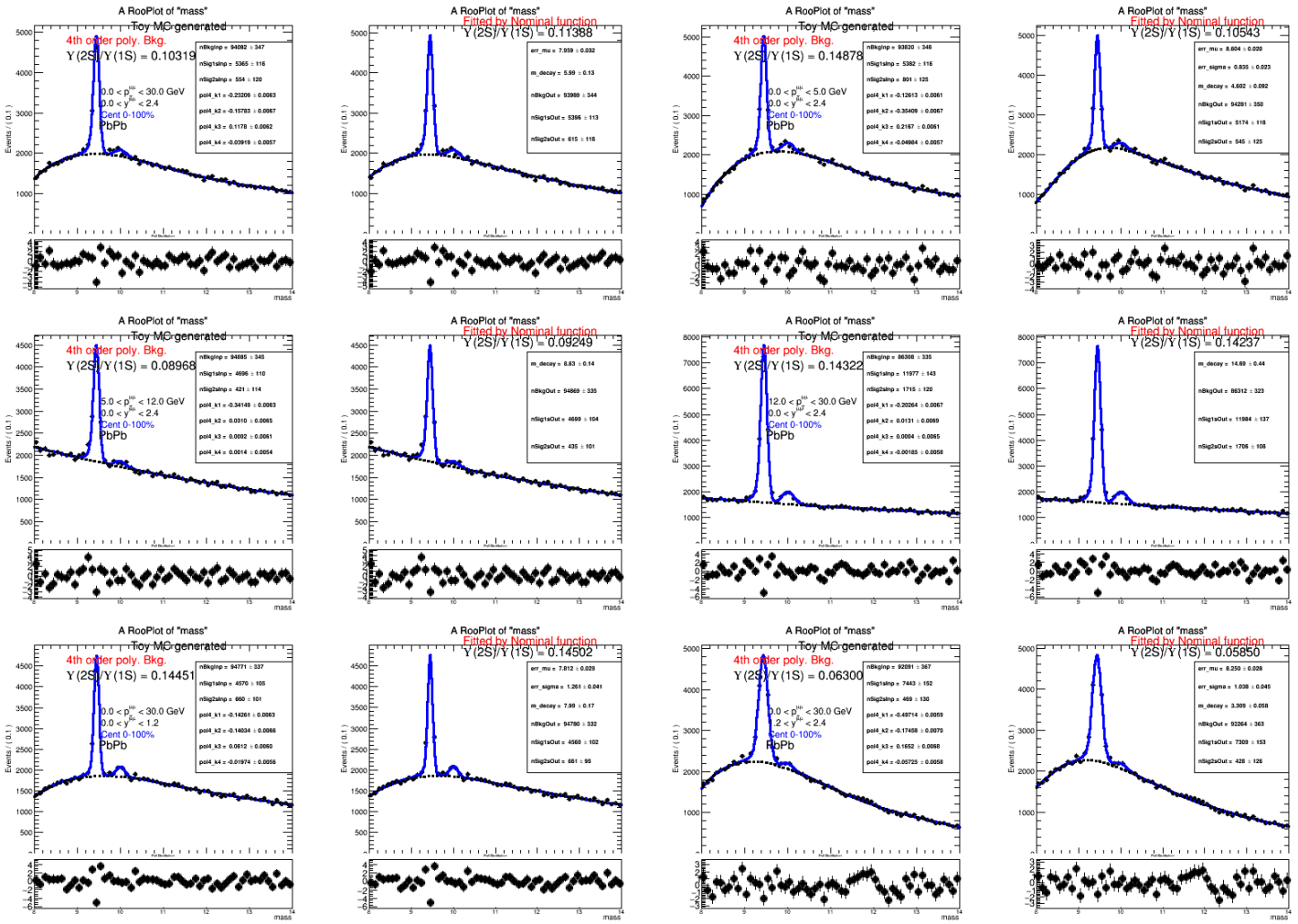

Figure 5.75: Fit variations using Toy MC study in Pb+Pb data generated with nominal PDF and subsequently fit by 4th order poly PDF (left) and generated and fit with the nominal PDF (right)

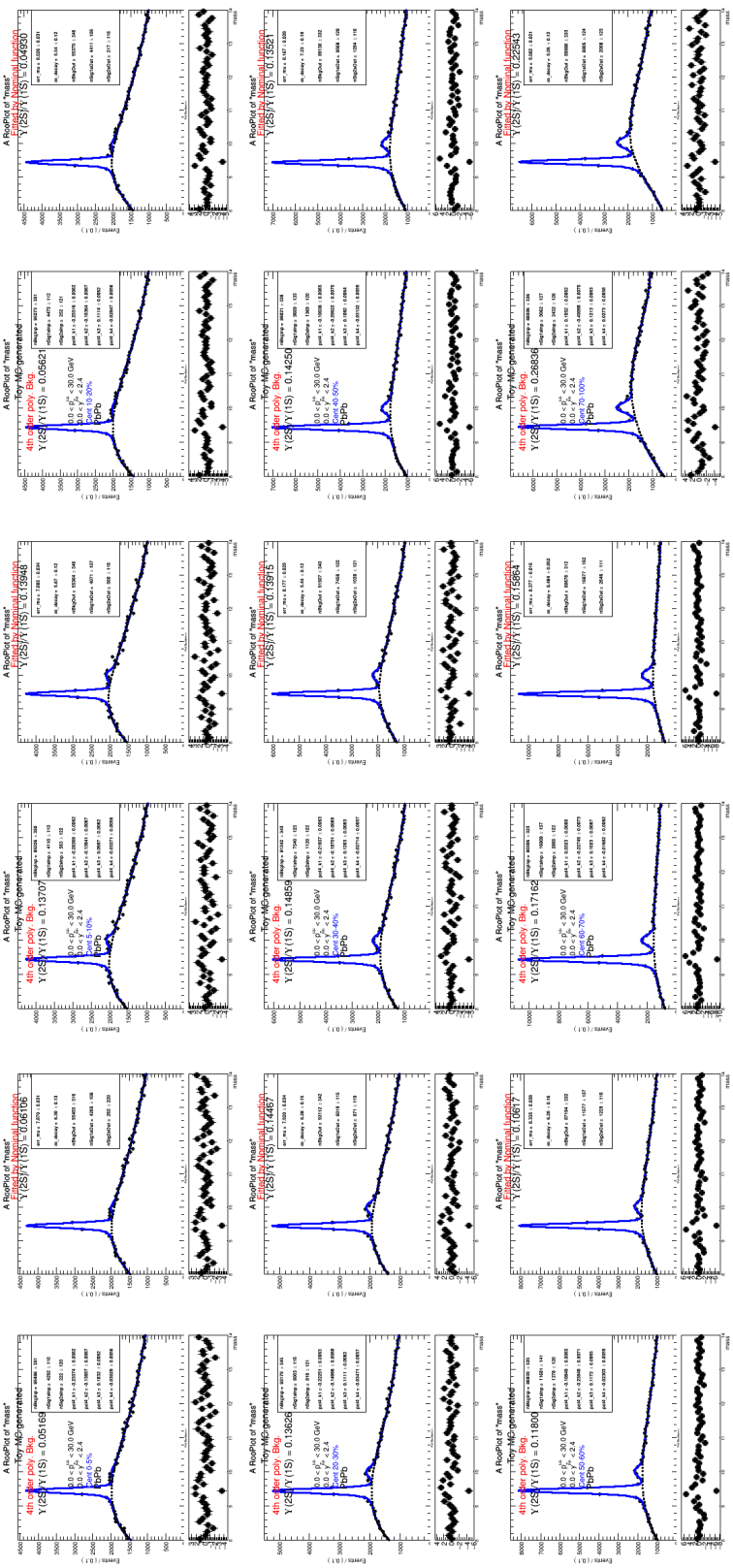

Figure 5.76: Fit variations using Toy MC study in Pb+Pb data generated with nominal PDF and subsequently fit by 4th order poly PDF (left) and generated and fit with the nominal PDF (right)

Table 5.23: Systematic of the double ratio of Υ(3S)/Υ(1S) obtained by fitting the real data with the nominal and alternative background models, then calculating the variation in the single and double ratio between the two cases, in units of percentage.

	Dev. in single ratio		Deviation in double ratio
	pp	PbPb	
Integrated	1.87	-47.98	48.93
0-10%	1.87	-30.51	31.79
10-30%		3.35×10^7	3.29×10^7
30-50%		-6.48	8.20
50-100%		29.41	27.03

The same study was performed for the Υ(3S) and the results are reflected in Table 5.23 for the alternative fits to data and Table 5.24 for the study of deviations in the toy MC. The toy MC studied is the preferred method for both the Υ(2S) and the Υ(3S)due to its robustness to potential bias and statistical fluctuations. This choice is reflected in the systematic summary table.

Table 5.24: Systematic of the double ratio of Υ(3S)/Υ(1S) obtained by fitting the toy MC generated pseudo-data with the nominal and alternative background models, then calculating the variation in the single and double ratio between the two cases, in units of percentage.

	Dev. in single ratio		Deviation in double ratio
	pp	PbPb	
Integrated	2.23	-68.35	69.04
0-10%	2.23	-28.02	29.61
10-30%		739.61	721.03
30-50%		2.44	0.18
50-100%		35.68	32.68

5.3.2.4 Systematic Uncertainty from background PDF parameters

This section details the systematic uncertainty that arises from choosing to hold the Erf width parameter, σ, in the background model, Eq. (5.7), constant during the fitting. The systematic is achieved by fitting with this background width parameter free floating. The deviation in the single ratio and double ratio is given as the systematic for the Υ(2S) and Υ(3S) double ratio. This is only studied in centrality and integrated bins because the fitting procedure only holds the width parameter constant for these bins particular bins as described in Section 5.1.3.

Table 5.25: Systematic (percent deviations) of single and double ratios of 2S to 1S due to allowing the background Erf width parameter to be free.

Bin	$\mathcal{R}_{21}$ Uncertainty (%)		$\mathcal{DR}_{21}$ Uncertainty (%)
	pp	PbPb	
p_T, y integrated	0.012	0.12	0.11
0-5%		0.40	0.42
5-10%		0.47	0.46
10-20%		1.92	1.93
20-30%		0.99	1.00
30-40%	0.012	2.45	2.46
40-50%		1.33	1.34
50-60%		0.85	0.84
60-70%		11.2	11.2
70-100%		8.43	8.42

Table 5.26: Systematic (percent deviations) of single and double ratios of 3S to 1S due to allowing the background Erf width parameter to be free.

Bin	$\mathcal{R}_{31}$ Uncertainty (%)		$\mathcal{DR}_{31}$Uncertainty (%)
	pp	PbPb	
p_T, y integrated	0.016	1.32	1.34
0-10%	-	7.9	7.9
10-30%	-	24.3	24.3
30-50%	-	4.4	4.4
50-100%	-	13.3	13.3

The following tables summarize the total uncertainty that arises from both the non-cancellation in efficiency, as well as the choice of signal and background modeling. Table 5.27 shows the results for the Υ(2S) while Table 5.28 for the Υ(3S). The uncertainties are taken into account in the following results chapter as boxes on the data points and are also reflected in the estimation of the confidence-level intervals.

Table 5.27: Total uncertainty of the double ratio of Υ(2S)/Υ(1S)

	Signal PDF Uncertainty				Background PDF Uncertainty				Efficiency Uncertainty	Final Uncertainty	
	Param. release		CB+Gauss		Alternative PDF with toy MC generation		Erf width Param. float		Dev. from unity		
	pp	PbPb	pp	PbPb	pp	PbPb	pp	PbPb	PbPb/pp	global(pp+eff)	PbPb
Integrated	0.38	2.22	0.97	1.84	2.05	4.65	0.01	0.12	1.40	2.69	5.47
0-5%		6.94		4.48		26.53		0.40			27.79
5-10%		4.05		1.28		5.09		0.47			6.65
10-20%		3.82		2.23		5.65		1.92			7.43
20-30%		1.21		1.79		4.04		0.99			3.72
30-40%	0.38	3.23	0.97	1.71	2.05	5.24	0.01	2.44	1.40	2.69	6.83
40-50%		2.67		1.58		5.54		1.33			6.48
50-60%		1.18		2.05		8.28		0.85			8.66
60-70%		1.00		1.87		4.45		11.17			12.21
70-100%		2.78		2.14		14.93		8.44			17.50
p_T<5GeV/c	3.40		2.36		38.48				1.40	38.73	
5<p_T<12GeV/c	1.19		1.93		13.04				1.40	13.31	
12<p_T<30GeV/c	1.00		0.60		2.61				1.40	3.18	
$\|y\|$<1.2	2.41		0.22		2.89				1.40	4.02	
1.2<$\|y\|$<2.4	3.44		4.48		3.37				1.40	6.73	

Table 5.28: Total uncertainty of the double ratio of Υ(3S)/Υ(1S)

	Signal PDF Uncertainty				Background PDF Uncertainty				Efficiency Uncertainty	Final Uncertainty	
	Param. release		CB+Gauss		Alternative PDF with toy MC generation		Erf width Param. float		Dev. from unity		
	pp	PbPb	pp	PbPb	pp	PbPb	pp	PbPb	PbPb/pp	global(pp+eff)	PbPb
Integrated	1.06	22.90	1.36	7.86	2.23	68.35	0.02	1.32	1.40	3.14	72.52
0-10%	1.06	8.81	1.36	1.20	2.23	28.02	0.02	7.91	1.40	3.14	30.44
10-30%		1.51×10^7		1.11×10^3		739.61		24.28			1.51×10^7
30-50%		3.23		2.39		2.44		4.38			14.43
50-100%		2.67		3.99		35.68		13.32			38.70

Chapter 6

Results

This chapter details the results from the previous sections for the double ratios defined as:

$$\mathcal{DR}_{21} = \left(\frac{\mathcal{R}_{21}|_{\mathrm{PbPb}}}{\mathcal{R}_{21}|_{\mathrm{pp}}}\right), \tag{6.1}$$

$$\mathcal{DR}_{31} = \left(\frac{\mathcal{R}_{31}|_{\mathrm{PbPb}}}{\mathcal{R}_{31}|_{\mathrm{pp}}}\right). \tag{6.2}$$

Figure 6.1 shows the dimuon invariant mass plots obtained in Section 5.1.4 and redrawn for convenience. The left plot is the $p+p$ invariant mass distribution in black points with the total fit shown in solid blue, the background as a dot-dashed blue line, and the individual Υ peaks as dotted gray lines. The right plot is the Pb+Pb data in black points with the same color scheme as just described for $p+p$. Additionally, the right plot contains the $p+p$ signal shape added to the Pb+Pb background and normalized to the Υ(1S) mass peak in Pb+Pb, given as the dashed red line. It is clear from the right hand plot that there is a large relative suppression of both the Υ(2S) and Υ(3S). In other words, this graphically illustrates that the double ratios for the excited Υ states are less than 1. The Υ(3S)is not visible in Pb+Pb data as it is almost fully, one of the main justifications for our estimation of an upper limit.

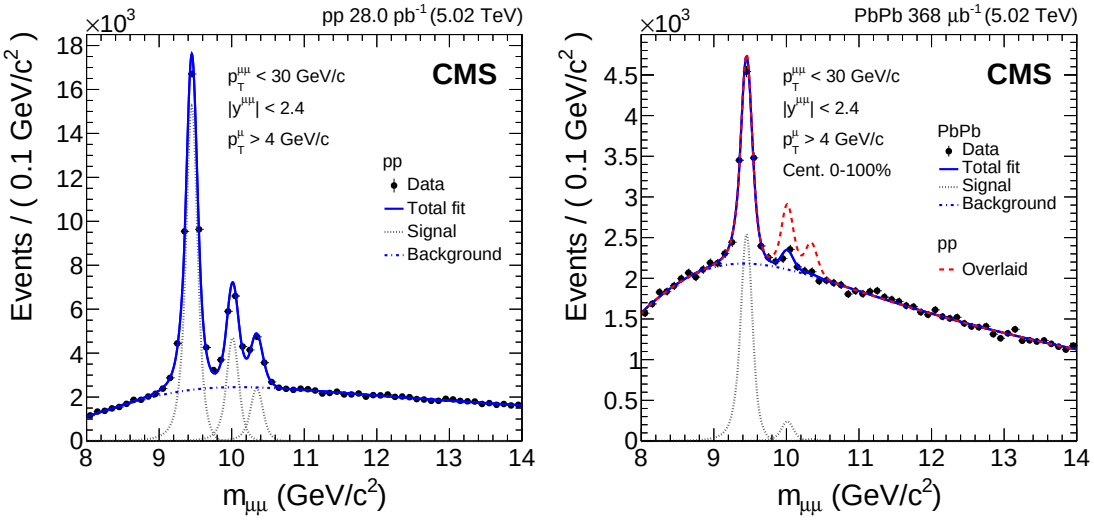

Figure 6.1: Measured dimuon invariant mass distributions for $p+p$ (left) and PbPb (right) data. The total fit (solid blue line) and the background component (dot-dashed blue line) are also shown, as are the individual Υ(1S), Υ(2S), and Υ(3S) signal shapes (dotted gray lines). The dashed red line in the Pb+Pb panel represents the $p+p$ signal shape from the pp panel added to the PbPb background and normalized to the Υ(1S) mass peak in Pb+Pb.

6.1 Υ(2S) Double Ratio

Figure 6.2 shows the $\mathcal{DR}_{21}$ as a function of $N_{\rm part}$. As noted earlier, a larger value of $N_{\rm part}$ corresponds to more central collisions, and smaller values to peripheral ones. A slight downward trend can be seen as one reaches more central collisions. The most peripheral bin is compatible with unity while the most central bin has a yield consistent with zero, hence we calculate an upper limit at the 95% confidence level represented by a blue arrow. The right subpanel in this plot shows the centrality, p_T and y integrated value for the $\mathcal{DR}_{21}$. The blue boxes on the points refer to the systematic error resulting from background and signal shape variation. The blue box at unity is due to the *pp* signal shape, background, and statistical error as well as the systematic due to not correcting the double ratio for efficiency.

Figures 6.3 and 6.4 show the $\mathcal{DR}_{21}$ as a function of dimuon p_T and $|y|$ respectively. Both figures show an overall large relative suppression and roughly flat dependence across their respective kinematic variables within their uncertainties. Both figure have system-

atic errors that reflect background shape variation, signal parameter variations and the efficiency systematic as discussed in Ch. 5 displayed as the blue boxes.

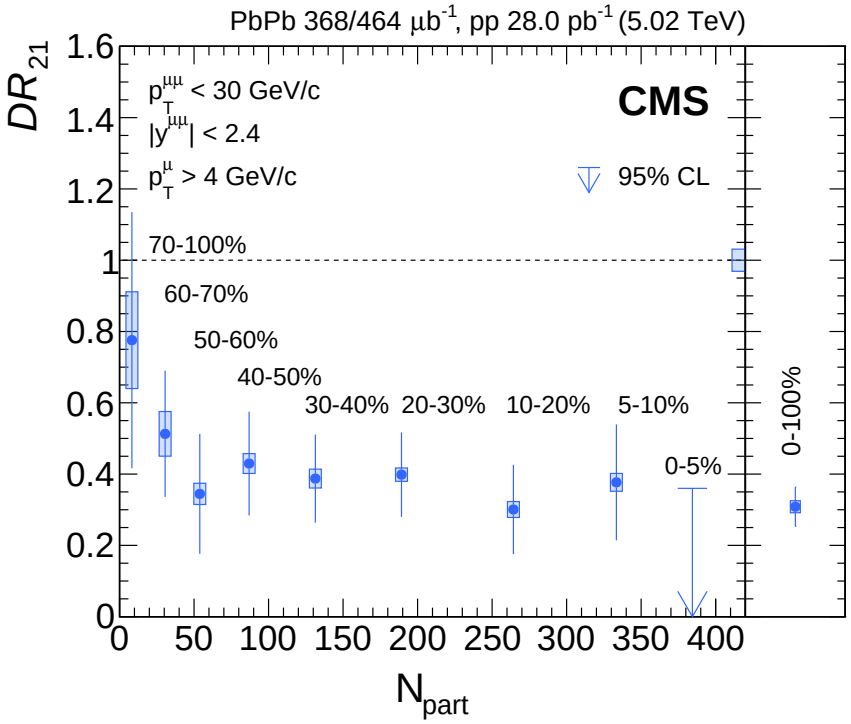

Figure 6.2: Double ratio of the $\Upsilon(2S)$ as a function of centrality. The centrality-integrated value is shown in the right panel. The error bars represent the statistical uncertainty in the Pb+Pb data while the boxes represent the systematic uncertainty due to signal and background variations. The box drawn around the line at unity depicts the systematic and statistical uncertainties from $p+p$ data, as well as the systematic uncertainties due to the combined detection efficiency.

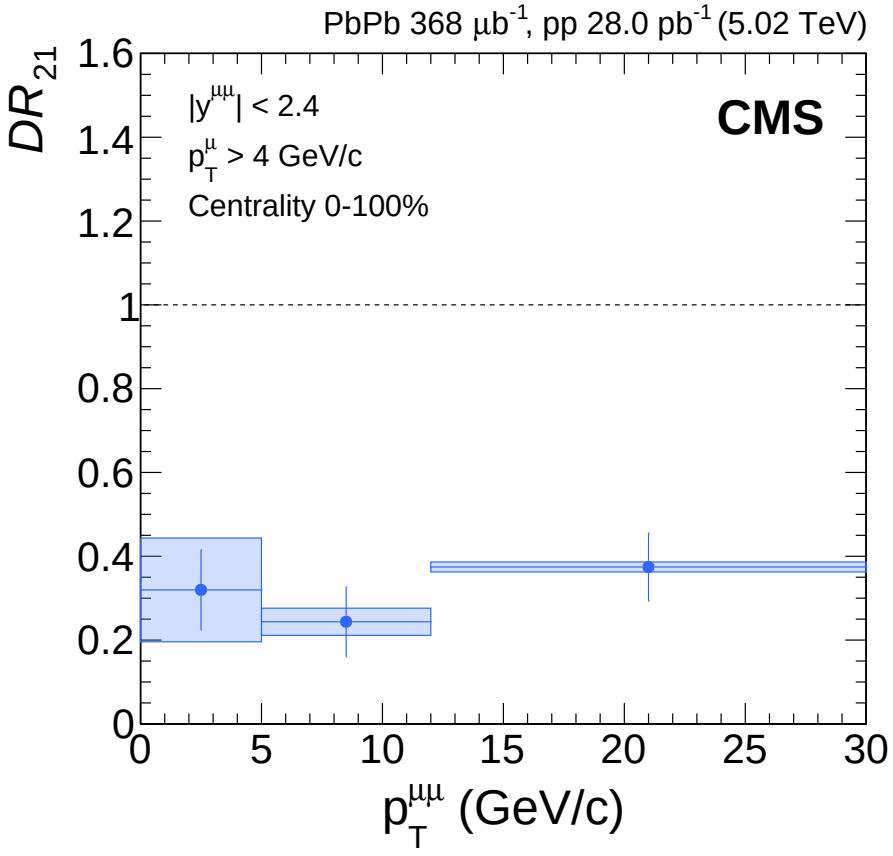

Figure 6.3: Double ratio of the Υ(2S) as a function of $p_T{}^{\mu\mu}$. The error bars depict the statistical uncertainty while the boxes represent the systematic uncertainties in the signal and background models as well as the combined detection efficiency.

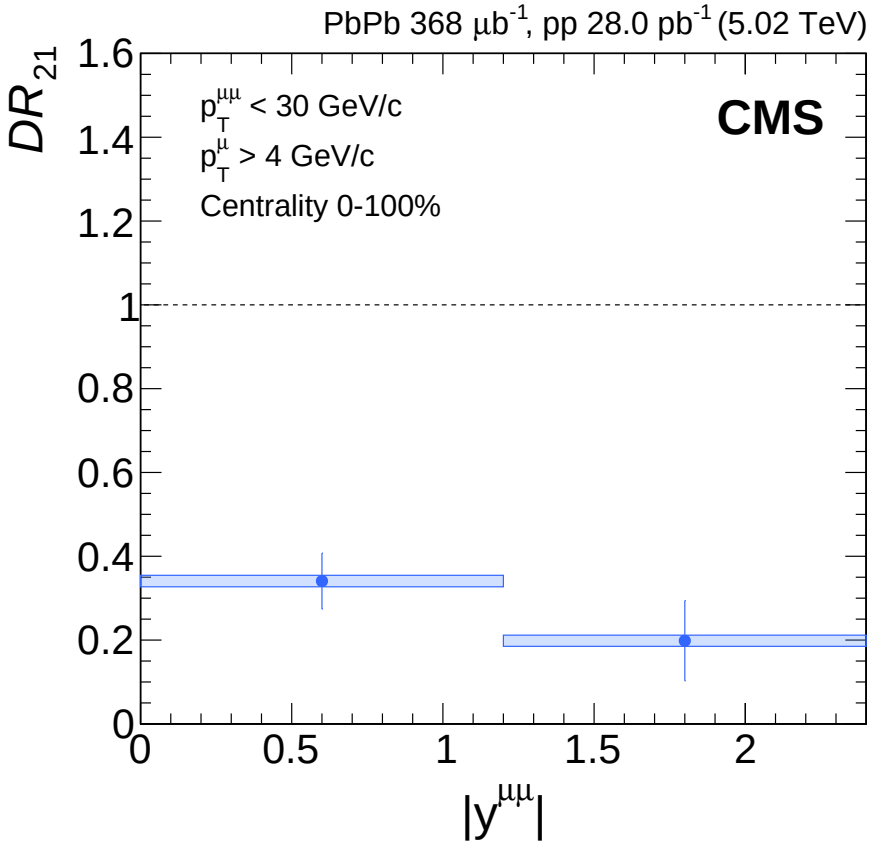

Figure 6.4: Double ratio of the Υ(2S) as a function of $|y^{\mu\mu}|$. The error bars depict the statistical uncertainty while the boxes represent the systematic uncertainties in the signal and background models as well as the combined detection efficiency.

6.1.1 Υ(3S) Upper limit

Figure 6.5 shows the culmination of the results found in Section 5.1.6 and specifically the result for the Asymptotic calculation where the $\mathcal{DR}_{31}$ upper limit was obtained. The arrows refer to the 95% confidence level while the red boxes refer to the 68% confidence level intervals. Across the entire centrality range, there is a large relative suppression. The centrality-integrated bin in the right subpanel also shows a large relative suppression for the 68 and 95% CL intervals.

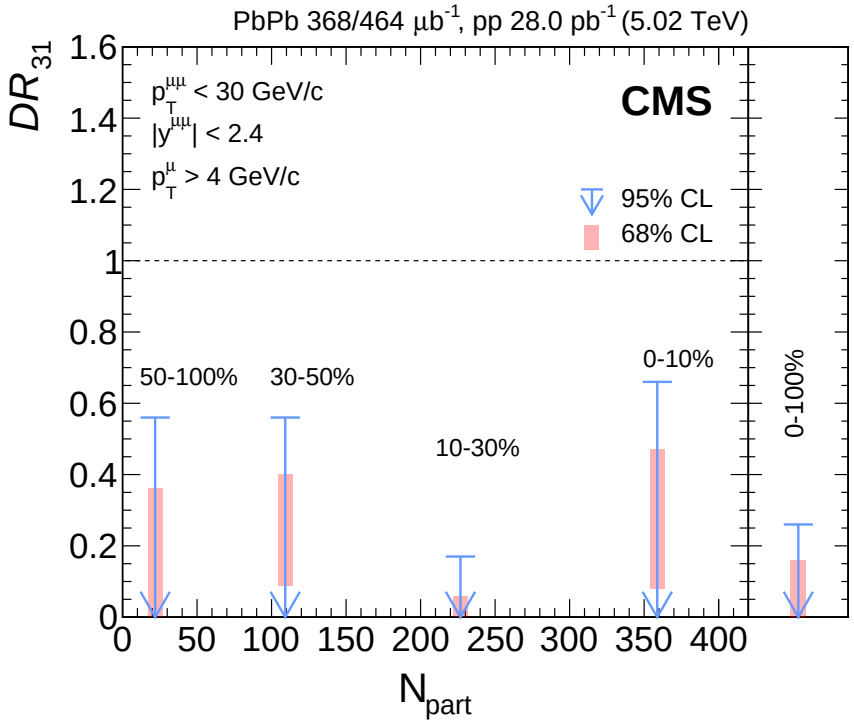

Figure 6.5: Confidence intervals at 95% CL (blue arrows) and 68% CL (red boxes) of the Υ(3S) double ratio as a function of centrality. The centrality-integrated limit is shown in the right subpanel.

6.2 Tabulated Results

Table 6.1: Measured Υ(2S) double ratio as a function of centrality, ${p_T}^{\mu\mu}$, and $|y^{\mu\mu}|$.

Centrality class	$\mathcal{DR}_{21}$
0–5%	< 0.36 at 95% CL, < 0.23 at 68% CL
5– 10%	$0.377 \pm 0.163 \pm 0.025$
10–20%	$0.301 \pm 0.125 \pm 0.022$
20–30%	$0.398 \pm 0.119 \pm 0.019$
30–40%	$0.387 \pm 0.124 \pm 0.026$
40–50%	$0.430 \pm 0.146 \pm 0.028$
50–60%	$0.344 \pm 0.168 \pm 0.030$
60–70%	$0.513 \pm 0.177 \pm 0.063$
70–100%	$0.776 \pm 0.359 \pm 0.136$
0–100%	$0.308 \pm 0.055 \pm 0.017$
Global relative uncertainty	$\pm$ 0.031

${p_T}^{\mu\mu}$ (GeV/c)	
0–5	$0.320 \pm 0.096 \pm 0.121$
5–12	$0.244 \pm 0.083 \pm 0.032$
12–30	$0.374 \pm 0.081 \pm 0.012$

$\lvert y^{\mu\mu}\rvert$	
0–1.2	$0.341 \pm 0.067 \pm 0.014$
1.2–2.4	$0.198 \pm 0.096 \pm 0.013$

Table 6.2: Measured Υ(3S) double ratio as a function of centrality, in terms of confidence intervals at 68% and 95% CL.

	$\mathcal{DR}_{31}$ confidence level intervals	
Centrality class	at 95% CL	at 68% CL
0–10%	< 0.66	$[0.08, 0.47]$
10–30%	< 0.17	< 0.06
30–50%	< 0.56	$[0.09, 0.40]$
50–100%	< 0.56	< 0.36
0–100%	< 0.26	< 0.16

6.3 Comparisons

In this section we compare our results to various theoretical models and previous experimental measurements. Figure 6.6, Figure 6.7 shows the Υ(2S) double ratio as a function of centrality, rapidity with theory curves overlaid. The model represented by the orange lines [15] includes predictions of suppression including color screening effects and taking into account bottomonia feed down. The model illustrated with green lines [5], having an additional regeneration component, agree with the data and each other. Figure 6.7 shows the double ratio as a function of p_T with both of these models overlaid. Figure 6.8 shows the double ratio as a function of $|y|$ with only the model from [15]. The two models are in good agreement with the data and indicate a large initial temperature of the system. Krouppa et al. predict an initial temperature of 600 - 700 MeV while the Rapp et al. model predicts an initial temperature of $\sim$ 590 MeV, both being larger than three times the predicted crossover temperature of the QGP phase.

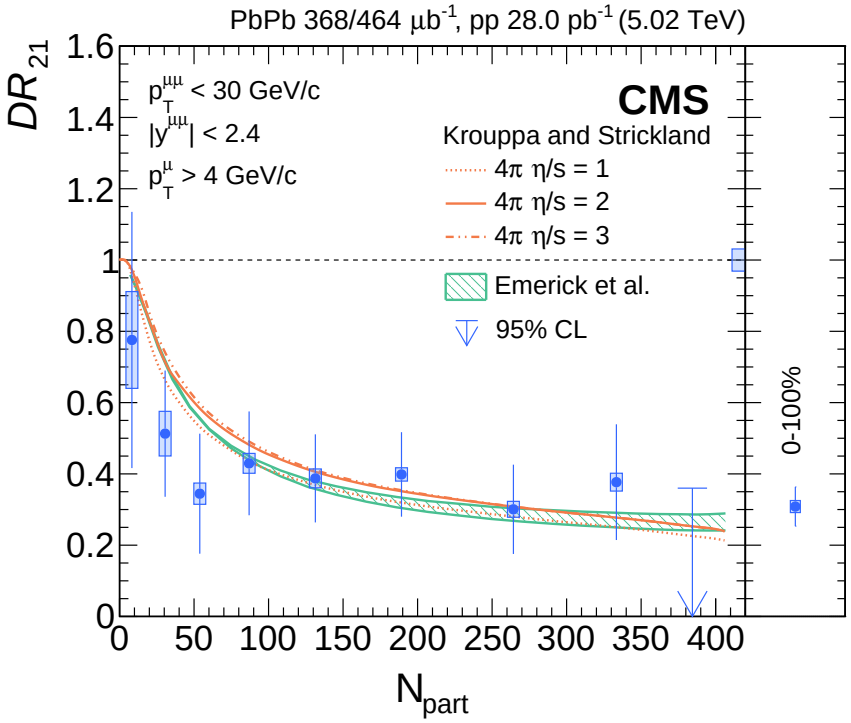

Figure 6.6: Double ratio of the Υ(2S) as a function of centrality overlaid with calculations by Krouppa and Strickland (orange curves [15]) and by Rapp et al. (green hatched band [5]).

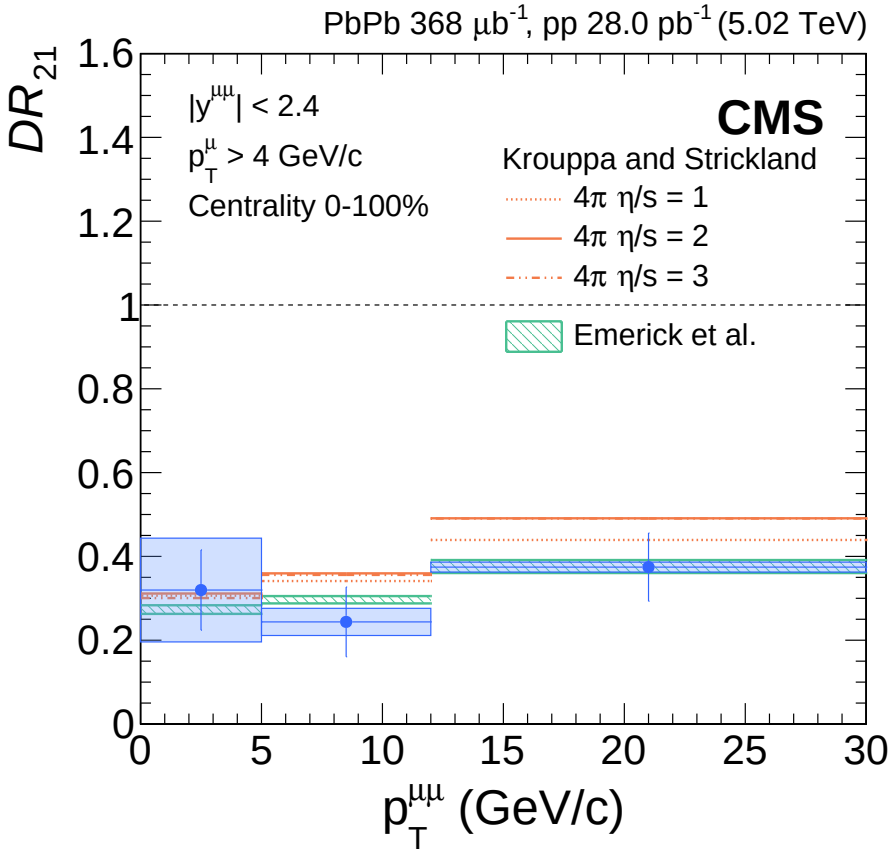

Figure 6.7: Double ratio of the Υ(2S) as a function of $p_T{}^{\mu\mu}$ overlaid with calculations by Krouppa and Strickland (orange curves [15]) and by Rapp et al. (green hatched band [5]).

Figure 6.9 shows the Υ(2S) double ratio as a function of centrality as presented in this work at 5.02 TeV in blue and as found in Ref. [8] from the CMS collaboration using data at the center-of-mass energy of 2.76 TeV in red. Over all centrality and for the integrated value, the two collision energy calculations are in agreement within uncertainties. Given the large global uncertainty for the 2.76 TeV data in red, arising mostly from the much more modest available pp data at the time of the analysis in Ref.. [8] (shown at unity) the current measurement in blue is a much more precise measurement but with a similar level of relative suppression.

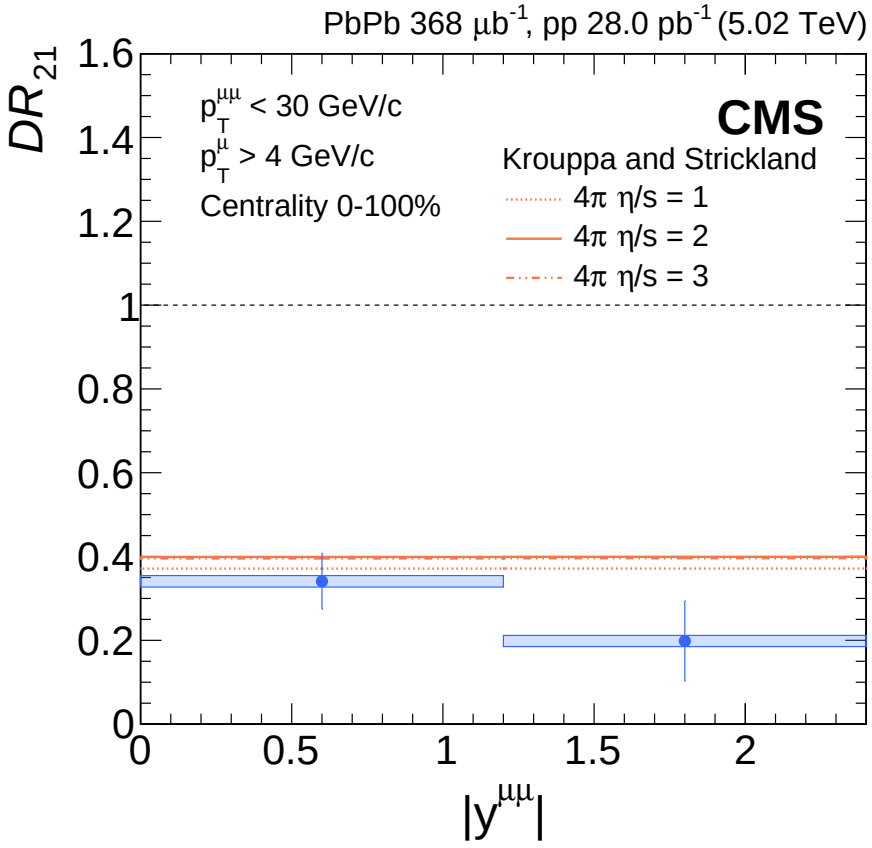

Figure 6.8: Double ratio of the Υ(2S) as a function of $|y^{\mu\mu}|$ overlaid with calculations by Krouppa and Strickland (orange curves [15])

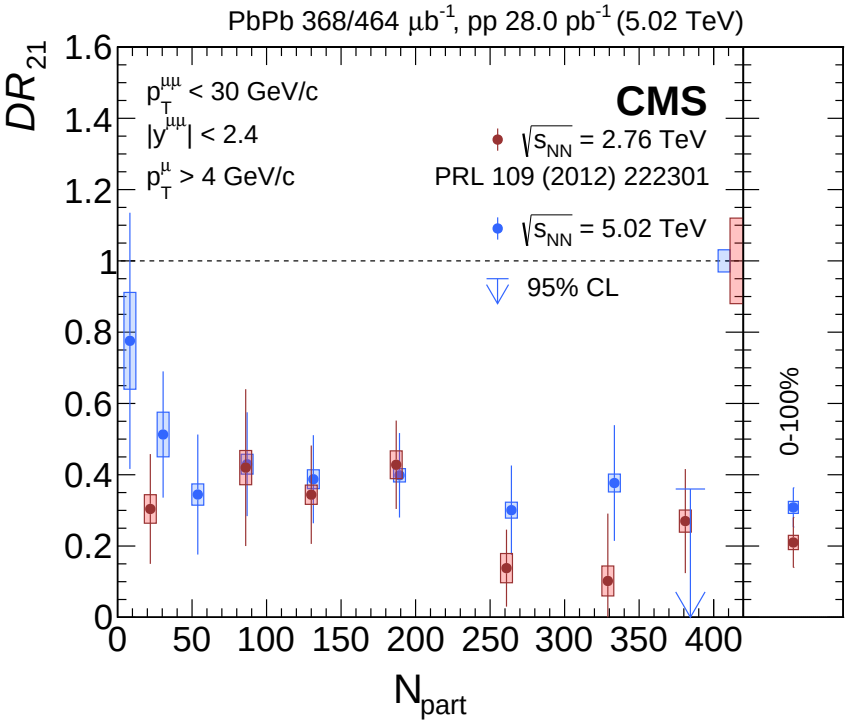

Figure 6.9: Double ratio of the Υ(2S) as a function of centrality at 5.02 TeV collision energy in blue and 2.76 TeV center-of-mass energy in red from Ref. [8]. The global uncertainties are reported in line at unity for both energies and the right panel reflects the centrality integrated values.

Chapter 7

Conclusion

The original goal of the measurement for the Υ(2S) and Υ(3S) double ratios at $\sqrt{s_{\rm NN}} =$ 5.02 TeV has been achieved. The $p+p$ and Pb+Pb data samples used were significantly larger than those used in the corresponding 2.76 TeV measurements. The integrated luminosities increased by a factor of 2.3 for the Pb+Pb sample and by more than a factor of 100 for the $p+p$ sample.

We were able to measure the Υ(2S) double ratio as a function of $N_{\rm part}$ (in 9 bins) and determined that the overall relative modification was large in most of the bins of this analysis except the most peripheral bin (70–100%), where the $\mathcal{DR}_{21}$ value is compatible with unity within the statistical and systematic errors. The remaining 8 bins were compatible with a large relative suppression. The centrality-integrated Υ(2S) double ratio is found to be $\mathcal{DR}_{21} = 0.308 \pm 0.055\,(\text{stat}) \pm 0.019\,(\text{syst})$. This value is below 1 at the $\sim 11\sigma$ level, indicating a very strong relative suppression. In the most central (0–5%) bin the Υ(2S) suppression relative to the Υ(1S) is so large that a 95% confidence level upper limit was calculated and found to be $\mathcal{DR}_{21}(0-5\%) < 0.36$. This large relative suppression of the Υ(2S) did not show significant variations with ${p_T}^{\mu\mu}$ or $|y^{\mu\mu}|$ within the explored phase space of ${p_T}^{\mu\mu} < 30$ GeV/c and $|y^{\mu\mu}| < 2.4$. The predictions from Strickland et al. and Rapp et al. are in good agreement with our data. The previous measurements at 2.76 TeV are comparable within uncertainties to our 5.02 TeV measurement for the $\mathcal{DR}_{21}$ as a function of $N_{\rm part}$.

For the Υ(3S) double ratio, we were able to make this measurement in four centrality

bins, a first in heavy-ion collisions. The centrality-integrated Υ(3S) double ratio was calculated to be < 0.26 for the 95% CL. The 95% CL intervals for the Υ(3S) double ratio exclude unity in all four centrality bins of this analysis, including the most peripheral collisions (50–100%). This was surprising considering the model expectations that the Υ should be less suppressed in peripheral collisions. However, the Υ(3S) has the smallest binding energy and largest radius of all the three states, which makes it the most susceptible to modification by the QGP.

Bibliography

[1] W. M. P. F. Kyle Cranmer. *A fresh look for the standard model*. 2013. URL: http://www.quantumdiaries.org/2013/08/19/a-fresh-look-for-the-standard-model/ (visited on 2017).

[2] C. Patrignani et al. "Review of Particle Physics". In: *Chin. Phys.* C40.10 (2016), p. 100001. DOI: 10.1088/1674-1137/40/10/100001.

[3] R. Vogt. *Ultrarelativistic heavy-ion collisions*. Amsterdam: Elsevier, 2007. ISBN: 9780444521965.

[4] A. Bazavov et al. "Equation of state and QCD transition at finite temperature". In: *Phys. Rev.* D80 (2009), p. 014504. DOI: 10.1103/PhysRevD.80.014504. arXiv: 0903.4379 [hep-lat].

[5] X. Du, R. Rapp, and M. He. "Color Screening and Regeneration of Bottomonia at RHIC and the LHC". In: (2017). arXiv: 1706.08670 [hep-ph].

[6] J. Adams et al. "Evidence from d + Au measurements for final state suppression of high p(T) hadrons in Au+Au collisions at RHIC". In: *Phys. Rev. Lett.* 91 (2003), p. 072304. DOI: 10.1103/PhysRevLett.91.072304. arXiv: nucl-ex/0306024 [nucl-ex].

[7] C. Collaboration. R_{AA} *Zoo Plots*. 2013. URL: https://twiki.cern.ch/twiki/bin/view/CMSPublic/HIRaaCompilation (visited on 2013).

[8] S. Chatrchyan et al. "Observation of sequential Upsilon suppression in PbPb collisions". In: *Phys. Rev. Lett.* 109 (2012), p. 222301. DOI: 10.1103/PhysRevLett.109.222301. arXiv: 1208.2826 [nucl-ex].

[9] T. Matsui and H. Satz. "J/ψ suppression by quark-gluon plasma formation". In: *Phys. Lett. B* 178 (1986), p. 416. DOI: 10.1016/0370-2693(86)91404-8.

[10] F. Brezinski and G. Wolschin. "Gluodissociation and Screening of υ States in PbPb Collisions at $\sqrt{s_{NN}} = 2.76$ TeV". In: *Phys. Lett.* B707 (2012), pp. 534–538. DOI: 10.1016/j.physletb.2012.01.012. arXiv: 1109.0211 [hep-ph].

[11] A. Mocsy and P. Petreczky. "Color screening melts quarkonium". In: *Phys. Rev. Lett.* 99 (2007), p. 211602. DOI: 10.1103/PhysRevLett.99.211602. arXiv: 0706.2183 [hep-ph].

[12] A. Rothkopf, T. Hatsuda, and S. Sasaki. "Complex heavy-quark potential at finite temperature from lattice QCD". In: *Phys. Rev. Lett.* 108 (2012), p. 162001. DOI: 10.1103/PhysRevLett.108.162001. arXiv: 1108.1579 [hep-lat].

[13] Y. Burnier, O. Kaczmarek, and A. Rothkopf. "Quarkonium at finite temperature: Towards realistic phenomenology from first principles". In: *JHEP* 12 (2015), p. 101. DOI: 10.1007/JHEP12(2015)101. arXiv: 1509.07366 [hep-ph].

[14] H. Satz. "Quarkonium Binding and Dissociation: The Spectral Analysis of the QGP". In: *Nucl. Phys.* A783 (2007), pp. 249–260. DOI: 10.1016/j.nuclphysa.2006.11.026. arXiv: hep-ph/0609197 [hep-ph].

[15] B. Krouppa and M. Strickland. "Predictions for bottomonia suppression in 5.023 TeV Pb-Pb collisions". In: *Universe* 2 (2016), p. 16. DOI: 10.3390/universe2030016. arXiv: 1605.03561 [hep-ph].

[16] S. Myers. "The Large Hadron Collider 2008–2013". In: *International Journal of Modern Physics A* 28.25 (2013), p. 1330035. DOI: 10.1142/S0217751X13300354. URL: http://www.worldscientific.com/doi/abs/10.1142/S0217751X13300354.

[17] P. Mouche. "Overall view of the LHC. Vue d'ensemble du LHC". In: (2014). General Photo. URL: https://cds.cern.ch/record/1708847.

[18] "Pulling together: Superconducting electromagnets". In: (2012). URL: http://cds.cern.ch/record/1997395.

[19] X. Vidal and R. Manzano. *Taking a Closer Look at LHC*. URL: http://www.lhc-closer.es/taking_a_closer_look_at_lhc/0.magnetic_multipoles.

[20] "Radiofrequency cavities". In: (2012). URL: http://cds.cern.ch/record/1997424.

[21] R. Dixon. *Phase Stability*. 2015. URL: http://news.fnal.gov/2015/08/phase-stability/.

[22] K. Schindl. "The injector chain for the LHC". In: CERN-OPEN-99-052 (1999), 6 p. URL: https://cds.cern.ch/record/397574.

[23] "The accelerator complex". In: (2012). URL: http://cds.cern.ch/record/1997193.

[24] A. Beuret et al. "The LHC Lead Ion Injector Chain". In: *9th European Particle Accelerator Conference (EPAC 2004) Lucerne, Switzerland, July 5-9, 2004*. 2004. URL: http://accelconf.web.cern.ch/AccelConf/e04/PAPERS/TUPLT011.PDF.

[25] S. Magazine. *The skinny on the LHC's heavy ions*. 2010. URL: http://www.symmetrymagazine.org/breaking/2010/11/05/the-skinny-on-the-lhcs-heavy-ions (visited on 2016).

[26] C. De Melis. "The CERN accelerator complex. Complexe des acclrateurs du CERN". In: (2016). General Photo. URL: https://cds.cern.ch/record/2197559.

[27] T. Sakuma and T. McCauley. "Detector and Event Visualization with SketchUp at the CMS Experiment". In: *J. Phys. Conf. Ser.* 513 (2014), p. 022032. DOI: 10.1088/1742-6596/513/2/022032. arXiv: 1311.4942 [physics.ins-det].

[28] S. Chatrchyan et al. "The CMS experiment at the CERN LHC". In: *JINST* 3 (2008), S08004. DOI: 10.1088/1748-0221/3/08/S08004.

[29] T. Lenzi. "Development and Study of Different Muon Track Reconstruction Algorithms for the Level-1 Trigger for the CMS Muon Upgrade with GEM Detectors". MA thesis. U. Brussels (main), 2013. arXiv: 1306.0858 [physics.ins-det]. URL: https://inspirehep.net/record/1236817/files/arXiv:1306.0858.pdf.

[30] C. Collaboration. "Commissioning of the CMS experiment and the cosmic run at four tesla". In: *Journal of Instrumentation* 5.03 (2010), T03001. URL: http://stacks.iop.org/1748-0221/5/i=03/a=T03001.

[31] C. Marc Favre. "The CMS solenoid descends to 100 Kelvin". CMS Collection. 2006. URL: http://cds.cern.ch/record/930268.

[32] C. Collaboration. *Silicon Pixels*. 2011. URL: https://cms.cern/detector/identifying-tracks/silicon-pixels (visited on 2017).

[33] T. Rohe. "Sensor Concepts for Pixel Detectors in High Energy Physics". In: *Paul Scherrer Institut, 5232 Villigen PSI* (2002).

[34] C. Collaboration. *Silicon Strips*. 2011. URL: https://cms.cern/detector/identifying-tracks/silicon-strips (visited on 2017).

[35] L. Borrello et al. *Sensor Design for the CMS Silicon Strip Tracker*. Tech. rep. CMS-NOTE-2003-020. Geneva: CERN, 2003. URL: http://cds.cern.ch/record/687861.

[36] C. Collaboration. *Energy of Electrons and Photons (ECAL)*. 2011. URL: https://cms.cern/detector/measuring-energy/energy-electrons-and-photons-ecal (visited on 2017).

[37] M Brice, L Vaillet, and L Lazic. "Images of the CMS HCAL Barrel (HB)". CMS Collection. 2008. URL: https://cds.cern.ch/record/1431485.

[38] C. Collaboration. *Energy of Hadrons (HCAL)*. 2011. URL: https://cms.cern/detector/measuring-energy/energy-hadrons-hcal (visited on 2017).

[39] S. R. Davis. "CMS slice image view (transverse/longitudinal/3-D)". In: (2016). URL: http://cds.cern.ch/record/2204863.

[40] G. Abbiendi. "The CMS muon system in Run2: preparation, status and first results". In: *PoS* EPS-HEP2015 (2015), p. 237. arXiv: 1510.05424 [physics.ins-det].

[41] C. Collaboration. *Resistive Plate Chambers*. 2011. URL: https://cms.cern/detector/detecting-muons/resistive-plate-chambers (visited on 2017).

[42] C. Collaboration. *Data Formats and Data Tiers*. 2016. URL: https://twiki.cern.ch/twiki/bin/view/CMSPublic/WorkBookDataFormats (visited on 2016).

[43] C. Loizides, J. Nagle, and P. Steinberg. "Improved version of the PHOBOS Glauber Monte Carlo". In: *SoftwareX* 1-2 (2015), p. 13. DOI: 10.1016/j.softx.2015.05.001. arXiv: 1408.2549 [nucl-ex].

[44] S. Chatrchyan et al. "Dependence on pseudorapidity and on centrality of charged hadron production in PbPb collisions at $\sqrt{s_{\mathrm{NN}}} = 2.76$ TeV". In: *JHEP* 08 (2011), p. 141. DOI: 10.1007/JHEP08(2011)141. arXiv: 1107.4800 [nucl-ex].

[45] T. Sjöstrand, S. Mrenna, and P. Skands. "A Brief Introduction to PYTHIA 8.1". In: *Comput. Phys. Commun.* 178 (2008), pp. 852–867. DOI: 10.1016/j.cpc.2008.01.036. arXiv: 0710.3820 [hep-ph].

[46] I. P. Lokhtin et al. "Heavy ion event generator HYDJET++ (HYDrodynamics plus JETs)". In: *Comput. Phys. Commun.* 180 (2009), pp. 779–799. DOI: 10.1016/j.cpc.2008.11.015. arXiv: 0809.2708 [hep-ph].

[47] the CMS HIN dilepton PInG. *Dimuon performance studies in 2015 5.02TeV pp and PbPb Data*. CMS Note 2016/048. 2016. URL: http://cms.cern.ch/iCMS/user/noteinfo?cmsnoteid=CMS%20AN-2016/048.

[48] V. Khachatryan et al. "Suppression of $\Upsilon(1S)$, $\Upsilon(2S)$ and $\Upsilon(3S)$ production in PbPb collisions at $\sqrt{s_{\mathrm{NN}}} = 2.76$ TeV". In: *Phys. Lett.* B770 (2017), pp. 357–379. DOI: 10.1016/j.physletb.2017.04.031. arXiv: 1611.01510 [nucl-ex].

[49] CMS Collaboration. *$\Upsilon(1S)$, $\Upsilon(2S)$ and $\Upsilon(3S)$ cross section measurements in pp collisions at $\sqrt{s} = 7$ TeV*. CMS Physics Analysis Summary CMS-PAS-BPH-12-006. 2012. URL: http://cdsweb.cern.ch/record/1548008.

[50] M. Oreglia. "A Study of the Reactions $\psi' \to \gamma\gamma\psi$". PhD thesis. Stanford University, 1980, SLAC Report R-236. URL: http://wwwlib.umi.com/dissertations/fullcit?p8108973.

[51] A. L. Read. "Presentation of search results: The CL(s) technique". In: *J. Phys.* G28 (2002). [,11(2002)], pp. 2693–2704. DOI: 10.1088/0954-3899/28/10/313.

[52] G. J. Feldman and R. D. Cousins. "A unified approach to the classical statistical analysis of small signals". In: *Phys. Rev. D* 57 (1998), p. 3873. DOI: 10.1103/PhysRevD.57.3873. arXiv: physics/9711021 [physics.data-an].

[53] G. Cowan et al. "Asymptotic formulae for likelihood-based tests of new physics". In: *Eur. Phys. J.* C71 (2011). [Erratum: Eur. Phys. J.C73,2501(2013)], p. 1554. DOI: 10.1140/epjc/s10052-011-1554-0,10.1140/epjc/s10052-013-2501-z. arXiv: 1007.1727 [physics.data-an].